**BERGISCHE
UNIVERSITÄT
WUPPERTAL**

JÜLICH
Forschungszentrum

Modeling orographic gravity waves from source to termination to improve parameterization schemes in climate models

Dissertation
zur Erlangung des Grades
Doktor der Naturwissenschaften (Dr. rer. nat.)

vorgelegt der
Bergischen Universität Wuppertal
Fakultät 4 – Mathematik und Naturwissenschaften

von
Sebastian Rhode

Wuppertal 2023

Contents

List of Figures

List of Tables

Abstract

Gravity waves (GWs) are one of the most important drivers of middle atmospheric circulations and strongly affect the polar vortex of the winter hemisphere. These waves are of comparatively small horizontal scales and are generated by a multitude of processes, of which wind flow over orography and convection are the most common. The resolution of today's climate models is, however, too coarse for resolving GWs explicitly; therefore, they need to be parameterized within long-term climate projections. These parameterizations are a first approximation of the GW's effect on the atmosphere. A technical shortcoming common to parameterization schemes is their vertical column-wise application without the possibility of horizontal communication between adjacent grid cells due to computation-cost intensity. Hence, parametrization schemes do not account for the horizontal propagation of GWs, even though many studies show the far propagation of gravity waves (and especially mountain waves, MWs) from their sources. This horizontal propagation transports the momentum carried by the orographic GWs away from regions of high orographic variability; thereby spreading the effect of the orography on the atmosphere dynamics. Studies attribute high variability and model biases in the southern hemisphere to this lack of horizontal propagation of mountain waves within climate models.

This thesis investigates approaches for improving the existing parameterization schemes for orographic GWs by statistically approximating the horizontal momentum transport without explicitly resolving the small-scale gravity waves or communicating between model grid columns at every altitude level. To this aim, a mountain wave model is developed that allows for a reliable estimation of mountain wave sources. In the next step, the propagation of the MWs through the atmosphere is modeled and analyzed for differing wind conditions to find a corresponding, statistically stable momentum transport pattern.

First, we investigate possible ways of developing an algorithm that derives mountain wave sources from elevation data. The general idea here is to approximate the orographic elevation data by a small number of two-dimensional mountain ridges with constant cross-sections along their length. These mountain ridges excite approximately monochromatic mountain waves with wave parameters, which are given by mountain wave theory. Two different algorithms are presented: a line detection applied to a reduced skeleton of the elevation data and a genetic algorithm fitting ideal mountain ridges to the elevation. Testing showed that the line-detection algorithm performs much better in reconstructing the original orography with a limited number of mountain ridges. Both algorithms yield the location, width, length, orientation, and height of mountain wave exciting features in the orography at various horizontal scales.

Once the mountain wave sources are estimated, the propagation of the MWs through the atmosphere can modeled using the Gravity wave Regional Or Global RAy Tracer (GRO-GRAT). Combining the source model and the ray tracer results in our mountain wave model (MWM), which is used for estimating MW propagation and momentum transport patterns. For the validation of the MWM against model data and observations, an algorithm for the construction of residual temperatures and gravity wave momentum flux (GWMF) is developed by assuming that each gravity wave can be described as a wave packet of limited spatial extent. The predicted temperature perturbations are compared to a simple Fourier mountain model, the high-resolution Integrated Forecast System (IFS) of the European Centre

for Medium-range Weather Forecast (ECMWF), and Airborne LIdar for studying the Middle Atmosphere (ALIMA) measurements taken during the SouthTRAC campaign in 2019. These comparisons show that the MWM predicts the induced GW perturbations and corresponding field shape well and that the reconstruction algorithm operates as intended. In addition, MWM predictions of global GWMF distributions in the Upper Troposphere/Lower Stratosphere (UTLS) are compared to High-Resolution Dynamics Limb Sounder (HIRDLS) satellite observations. Both data sets are in agreement in terms of MW activity, and further, the mountain wave model is used to explain observed features in the satellite data by investigating the wave parameters in specific regions.

Finally, the validated MWM allows for estimating the MW propagation and GWMF transport pattern by considering every launched MW from source to ray termination. A statistically stable transport pattern describing the horizontal MW propagation is generated by averaging over predictions of a whole year of atmospheric conditions. This GWMF transport pattern is applied to redistribute the GWMF of a columnar simulation, i.e., MWs propagate only in the vertical as in an MW parameterization, horizontally at a single altitude. This one-time redistribution reduces the root-mean-square deviation of the columnar simulation to the fully 3D propagating simulation by up to 60%. Hence, the approximation of the horizontal MW propagation by a transport pattern is a worthwhile approach for an improvement of orographic parameterization schemes at comparatively low performance costs.

In a second consideration, the possibility of approximating the horizontal spread of GWMF via diffusion is investigated. The corresponding diffusion coefficients are estimated from the ray tracing and GWMF data of the MWM. Although the GWMF spreads around the sources in this framework, it is not suitable for a precise approximation of the horizontal propagation of mountain waves. It could, however, at least reduce the sharpness of nudging tendencies around orographic variable regions in climate models cost-efficiently.

Zusammenfassung

Schwerewellen sind einer der wichtigsten Treiber der Zirkulationen in der mittleren Atmosphäre und haben insbesondere einen großen Einfluss auf den polaren Wirbel der Winterhemisphäre. Im Allgemeinen sind sie vergleichsweise kleinskalig und werden von einer Vielzahl Prozessen erzeugt, von denen die typischsten Strömung über Orographie und Konvektion sind. Aufgrund ihrer kleinen horizontalen Skalen ist allerdings die Auflösung heutiger Klimamodelle zu grob um Schwerewellen und ihre Quellen explizit auflösen zu können und daher müssen sie in längerfristigen Klimaprojektionen parametrisiert werden. Diese Parametrisierungen beschreiben den Effekt, den Schwerewellen auf die Atmosphäre haben, allerdings nur als erste Näherung. Eine der technischen Begrenzungen dieser Parametrisierungen besteht darin, dass sie in vertikalen Modellsäulen gerechnet werden, in denen lediglich vertikale Ausbreitung der Schwerewellen modelliert ist. Eine horizontale Wechselwirkung von angrenzenden Modellzellen ist aufgrund der Rechenkosten, nicht möglich, sodass die Modelle effektiv keine horizontale Schwerewellenausbreitung modellieren können. Studien in diesem Bereich haben jedoch gezeigt, dass ein Großteil der Variabilität der atmosphärischen Dynamik in der Südhemisphäre auf diese fehlende horizontale Ausbreitung von Gebirgswellen zurückzuführen ist.

In dieser Dissertation werden daher mögliche Ansätze untersucht um die existierenden Gebirgswellenparametrisierungen durch eine statistische Analyse des Ausbreitungsverhaltens der Schwerewellen zu verbessern, ohne dass diese im Model explizit aufgelöst werden müssen oder eine Wechselwirkung zwischen den Modellsäulen auf allen Höhen notwendig wird. Dafür wurde ein Gebirgswellenmodell entwickelt, welches zum einen eine verlässliche Basis an Gebirgswellenquellen gibt und zum anderen die nachfolgende Ausbreitung modelliert. Anschließend wird die Ausbreitung der vorher bestimmten Wellen in wechselnden atmosphärischen Hintergründen analysiert um ein entsprechendes, statistisch stabiles Impulsflusstransportverhalten abzuleiten.

Zunächst wird ein Algorithmus zur Detektion von Gebirgswellenquellen direkt in den Topographiedaten entwickelt. Die grundsätzliche Idee ist es, das Terrain mit einer kleinen Anzahl idealisierter, quasi-zweidimensionaler Gebirgskämme, deren Querschnitt entlang ihrer Länge eine konstante Gaußfunktion ist, anzunähern. In guter Näherung regen diese Gebirgskämme monochromatische Schwerewellen an, deren Wellenparameter, Amplitude und Wellenlänge, direkt aus der Theorie bestimmt werden können. Zwei unterschiedliche Algorithmen werden hier vorgestellt: zum einen ein Liniendetektionsalgorithmus, der auf ein reduziertes Skelett der Topographie angewendet wird um die Position der Gebirgskämme zu identifizieren; zum anderen ein genetischer Algorithmus, der diese Gebirgskämme per least-squares fit an die Topographie erkennt. In den Tests konnte der Liniendetektionsalgorithmus das Terrain deutlich besser mit einer begrenzten Menge an Gebirgskämmen annähern. Beide Algorithmen liefern die Position, Länge, Breite, Orientierung und Höhe der entsprechenden Strukturen auf verschiedenen horizontalen Skalen.

Nachdem die Gebirgswellenquellen bestimmt sind, wird die Ausbreitung durch die Atmosphäre durch den Gravity wave Regional Or Global RAy Tracer (GROGRAT) berechnet. Die Kombination aus dem Quellenmodell und dem Raytracer bildet das vollständige Gebirgswellenmodell, welches anschließend genutzt wird um das Ausbreitungs- und Impulsflusstransportverhalten zu bestimmen. Unter der Annahme, dass sich einzelne Schwerewellen als endlich ausgedehnte Wellenpakete ausbreiten, kann weiterhin ein Algorithmus aufgestellt werden, der

die durch die Schwerewellen induzierten Residuumstemperaturen und Impulsflussverteilungen aus den Daten des Raytracers bestimmt und somit zur Validierung verwendet werden kann. Die so simulierten Residuumstemperaturen werden hier mit einem einfachen Fourier-Gebirgswellenmodell, dem hochauflösenden Integrated Forecast System (IFS) des European Centre for Medium-range Weather Forecast (ECMWF) sowie Airborne LIdar for studying the Middle Atmosphere (ALIMA) Messungen, die während der SouthTRAC Kampagne 2019 gemessen wurden, verglichen. Diese Vergleiche zeigen, dass das hier vorgestellte Gebirgswellenmodell die Residuumstemperaturen und deren räumliche Verteilung gut vorhersagt. Weiterhin werden globale Impulsflussverteilungen aus dem Gebirgswellenmodell mit Satellitenmessungen des High Resolution Dynamics Limb Sounder (HIRDLS) verglichen. Diese beiden Datensätze zeigen gut vergleichbare Gebirgswellenaktivität in der Validierung. Zusätzlich wird das Gebirgswellenmodells dazu verwendet Strukturen der Satellitenmessung zu erklären indem die spezifischen Wellenparameter in den jeweiligen Regionen untersucht werden.

Das so validierte Gebirgswellenmodell wird schließlich verwendet um das Ausbreitungsverhalten und den Impulsflusstransport der Gebirgswellen statistisch zu analysieren. Dazu wird jede einzelne Welle, und somit ihr Impulsfluss, von der Quelle bis zur Brechung bzw. ihrem Endpunkt verfolgt. Durch die Simulation der Ausbreitung in wechselnden Atmosphärenbedingungen eines Jahres wird somit ein statistisch robustes Transportverhalten abgeleitet. Anschließend wird das so abgeleitete Transportmuster in einer Simulation, in der lediglich vertikale Ausbreitung erlaubt ist, angewendet um die Schwerewellen umzuverteilen und so die horizontale Ausbreitung, und damit den horizontalen Impulstransport, anzunähern. Dazu wird der Impulsfluss jeder Modellzelle einmalig auf einer festen Höhe mittels der bestimmten Transportverteilung horizontal umverteilt. Diese Umverteilung reduziert die root-mean-square Abweichung im Vergleich zur Simulation mit voller Ausbreitung um bis zu 60%. Die angenäherte Beschreibung des horizontalen Impulsflusstransports über ein statistisch erzeugtes Umverteilungsmuster ist daher eine sinnvolle Verbesserung für orographische Schwerewellenparametrisierungen, insbesondere da der Rechenaufwand der Umverteilung vergleichsweise gering ausfällt.

In einer weiteren Betrachtung wird anisotrope Diffusion als weitere Möglichkeit untersucht um die horizontale Ausbreitung der Gebirgswellen zu beschreiben. Dazu werden die entsprechenden Diffusionskoeffizienten direkt aus den Raytracing- und Impulsflussdaten des Gebirgswellenmodells bestimmt. Dieser Ansatz ist zwar dazu geeignet den Impulsfluss um die eigentlichen Quellen herum zu verteilen, jedoch nicht dazu die horizontale Ausbreitung auf weit entfernte Bereiche präzise wiederzugeben. Er könnte jedoch dazu verwendet werden die Schärfe der Nudging-Tendenzen in der Nähe von Gebirgswellenquellen, die viele Klimamodelle zeigen, kosteneffizient und auf einer physikalischer Grundlage aufbauend zu reduzieren.

Chapter 1

Introduction

Waves are part of our daily lives, be they surface waves on the ocean, sound waves in the air, or electromagnetic waves in our vision and telecommunication. So it is no wonder, that there is a zoo of waves in the atmosphere as well (see the schematic in Lighthill (1967)). These waves are means to transport energy within the atmosphere, thereby forcing the background winds. Via this forcing, the atmospheric waves drive circulations within the atmosphere, that are more or less analogous to, e.g., thermohaline circulations in the ocean. The largest-scale circulation in the atmosphere, the Brewer-Dobson circulation (BDC, Butchart (e.g. 2014)), transports freeze-dried air from the tropics through the strato- and mesosphere down to the upper troposphere/lower stratosphere (UTLS) region above the poles. It consists mainly of two transport pathways. The stratospheric branch (divided into shallow and deeper parts) of the circulation transports tropical air directly to the winter pole through the stratosphere. Secondly, the mesospheric, or upper, branch transports tropical air towards the summer stratopause, further up to the mesosphere, and turns back toward the winter pole before downwelling there. By transporting tropospheric air through the middle atmosphere, the BDC directly influences the lifetime and global distribution of greenhouse gases through the atmosphere. The driver of this circulation is the momentum released by dissipating internal waves. In particular, the upper mesospheric branch of the BDC, i.e. the overturning circulation, is mainly driven by gravity waves (GWs) (e.g. McIntyre, 1998; Alexander and Rosenlof, 2003).

1

For GWs, gravity serves as the restoring force initiating and sustaining the oscillation of air parcels. A GW can be excited by any kind of process, that leads to a vertical displacement of an air parcel in a stable atmosphere. An upwards (downwards) displaced air parcel cools down (heats up) adiabatically due to changing pressure. If the background atmosphere is stably stratified, it ends up being cooler (warmer) than the surrounding air and therefore denser and heavier (thinner and lighter). Due to the difference in density, a relative gravity (buoyancy) force will act on the air parcel to return it to equilibrium and thus start an oscillation. Therefore, GWs manifest as local perturbations of temperature and wind in the atmosphere.

GWs carry momentum, hereafter gravity wave momentum flux (GWMF), and energy along their group velocity. The vertical propagation direction in the middle atmosphere is predominantly upwards since most GW sources (e.g., convection, orography, jet instability) are located within the troposphere. Upon dissipation, GWs accelerate/decelerate the background winds in the direction of the wave vector proportionally to the amount of GWMF of the wave being released at that location. The deceleration of the background winds is the driver of the different branches of the BDC. At which altitude a GW breaks and deposits its momentum is linked to the intrinsic phase speed, i.e. phase speed with respect to the surrounding medium. If the wind changes such that the intrinsic phase speed becomes zero, the GW breaks down. This level is called the critical level. Processes like convection can generate a wide spectrum of ground-based phase speeds and directions, which leads to the corresponding GWs breaking at different altitudes. For example, in the summer hemisphere, most westward-oriented GWs encounter a critical level within the stratospheric summer easterlies (in the following also called the summer wind reversal), while the eastward-oriented GWs are able to propagate further until they reach their dissipation level in the mesosphere. Via this process, different altitudes are forced in different directions leading to the residual overturning circulation. More detail on the role of GWs in the BDC can be found in, e.g., Sato and Hirano (2019) and Kang et al. (2020).

The BDC is, however, not the only process in which GWs play an important role. The quasi-biennial oscillation (QBO) is characterized by eastwards-westward alternating zonal

winds in the tropical stratosphere with a period of about 28 months. The wind deceleration due to breaking GWs, the GW drag, is one contributor to the oscillation, as the reversal starts in the upper stratosphere and is consecutively drawn down towards the UTLS (e.g. Lindzen and Holton, 1968; Garfinkel et al., 2022). The interaction of the QBO with tropical wave activity has been the object of prior studies (e.g. Ern et al., 2014; Kim and Chun, 2015). In addition, the QBO influences the strength of the polar vortex via the Holton-Tan effect (e.g. Holton and Tan, 1980; Anstey and Shepherd, 2014). Disruptions of the QBO cycle have been associated with anomalous GW activity (Li et al., 2023) and connected to the BDC (Kang et al., 2022).

Another important atmospheric phenomenon to consider here is sudden stratospheric warming (SSW). These irregular events are characterized by a weakening or even reversing polar vortex followed by a sudden warming of the polar stratosphere by up to 50 Kelvin within a couple of days (Baldwin et al., 2021). SSWs are linked to extremely cold weather in the northern hemisphere (e.g. Vargin and Kiryushov, 2019; Xie et al., 2020) and contribute to the occurrence of severe wildfires in Australia by increasing surface temperatures and reducing rainfall (Lim et al., 2019). Planetary and gravity wave drag is the cause of the vortex slow-down process (e.g. Cullens et al., 2015; Stephan et al., 2020; Cullens and Thurairajah, 2021; Kogure et al., 2021) and GWs play a major role in preconditioning the polar vortex for a displacement event or a split event (Albers and Birner, 2014; Ern et al., 2016; Song et al., 2020). Furthermore, Kidston et al. (2015) showed that during SSWs the polar jet can be shifted southward and thereby directly affect the tropospheric weather systems. This dynamical downward coupling shows the importance of the stratosphere for sub-seasonal and seasonal predictions. More directly, Sigmond and Scinocca (2010) and Sandu et al. (2016) studied the surface effect of GWs in the polar region by comparing model simulations with differing GW activity. They found an increase of surface pressure at the North Pole of up to 9 hPa and a very strong regional surface temperature response of up to 2 degrees in high latitudes.

The spectral range of GWs poses a problem to both, observations and modeling. Since gravity is a comparatively strong force across wide scales, the horizontal wavelength spectrum

of propagating GWs stretches from about 1000 km on the wide end down to the order of 10 km in the short regime. While shorter horizontal wavelengths might exist, they are typically not considered in models and are prone to vertical reflection (c.f. Fritts and Alexander, 2003). Long-term climate projections using general circulation models (GCMs) currently allow horizontal resolutions of about 100 km, which in turn leads to explicitly resolved GWs of about 400 km horizontal wavelength and longer (Skamarock, 2004). A huge part of the gravity wave spectrum is therefore not considered in the model and needs to be parameterized. In general, GCMs employ parameterization schemes for orographically and convectively generated GWs separately. Observations, but also high-resolution model simulations, are crucial for the improvement and tuning of these schemes toward realistic results.

The parameterized sources, orography and convection, are two of the main sources of GWs. If strong air flows towards a mountain ridge, it is deflected upwards and passes over the mountain. The vertical deflection provides the initial displacement of the air parcel and excites an upward propagating GW above the mountain, a mountain wave (MW). Since the mountain is stationary, the excited GW will have stationary phases close to the source location and the warm/cold phase fronts follow the mountain shape. Along the trajectory of the MW, it might turn and propagate not only vertically, but also horizontally, far from the initialization location. The ground-based phase speed, i.e., the phase speed with respect to the ground, will stay close to zero. MWs, therefore, encounter a critical level, where the wind speed is zero. In particular, this is the case in the stratospheric summer easterlies. Convection, on the other hand, generates GWs with a wide phase speed spectrum and excites GWs via multiple mechanisms. The first process is pure thermal forcing, where the initial displacement is given by the convection itself. The second process, the obstacle effect, is similar to orographic GW excitation: a convective cell acts as a (moving) obstacle for the wind approaching it (predominantly in strong shear regions) and deflects the wind vertically. The final mechanism is the mechanical oscillator mechanism, where a local periodic oscillation serves as the momentum source (e.g. Fritts and Alexander, 2003). Since this study focuses on MWs, we focus on the MW source processes and parameterizations in the following.

The short-scale part of the orographic GW spectrum, which is not resolved by climate

models, is approximated by a parameterization scheme within GCMs. Typically, such a parameterization scheme considers only the total GWMF and GW drag stemming from a given model grid cell instead of individual MWs. After initial considerations by Pierrehumbert (1986), multiple approaches to describing the sub-grid-scale orography (SSO) have been developed by the end of the last century. Kim and Arakawa (1995) and Lott and Miller (1997) describe the most common SSO parameterizations that are still in use today. Both these parameterization schemes assume a single dominant mountain of elliptical shape in each grid cell that serves as the source of the MWs. Thereby, the SSO can be described by a few parameters like elevation variance, slope, anisotropy, and dominant orientation. The biggest difference between these schemes lies in the translation of the SSO parameters to GWMF and finally to GW drag. Since the introduction of these schemes, they have received some minor revisions targeting some systematical shortcomings. For one, the original schemes do not consider orographic anisotropy under changing wind directions other than reducing the GWMF, if the wind is not parallel to the dominant direction of the SSO. The original MW scheme of Kim and Arakawa (1995) was extended by Kim and Doyle (2005) to incorporate differing SSO parameters for 8 wind directions and, more recently, Xie et al. (2020, 2021) extended this even further for arbitrary wind directions, which results in a smoother transition in turning winds. The second shortcoming, that has been addressed recently, is the monochromatic representation of the SSO by a single-scale elliptical mountain. In reality, the SSO could excite a wide spectrum of MWs, which might also depend on the wind direction. van Niekerk and Vosper (2021) present a modification to the original Lott and Miller (1997) parameterization that accounts for multiple scales within the SSO and thereby more faithfully represents the underlying orography without the ad-hoc assumption of a single elliptic-shaped mountain.

A shortcoming, that has not yet been addressed in most MW parameterizations is the lack of horizontal propagation of MWs from their source grid cell. The parameterization is commonly applied in a late computational step, where the model is separated into vertical columns and distributed to different compute nodes. At this point, no (computation-cost efficient) communication between neighboring model columns is possible and the parameteri-

zation calculates the GW drag in the respective vertical column by considering only the SSO directly beneath. Studies and observations of GW propagation show, however, that GWs can propagate long horizontal distances from their sources (e.g. Preusse et al., 2002; Sato et al., 2012; Perrett et al., 2021; Kruse et al., 2022), leading to lateral momentum transport. This lack of horizontal momentum transport and the boundedness of the MW drag to mountainous regions leads to a mismatch in the atmospheric forcing and strong and sharp nudging tendencies in these regions. According to Geller et al. (2013), this lack of horizontal propagation is one of the major sources of uncertainties in the southern hemispheric dynamics in GCMs. These uncertainties contribute to common model biases like a too-late breakdown of the polar vortex and a cold-pole bias. Garcia et al. (2017) found that artificially (and hence unphysically) modifying the orographic parameterization could improve the forecast performance, further indicating that this is still an area where the models could be improved.

Therefore, we know that GCMs do not realistically consider the momentum transport of GWs, and MWs in particular. Although this problem has been known for a long time, and there has been much effort to improve the parameterization, horizontal propagation is still a pending problem. Bölöni et al. (2021) implement the horizontal propagation of MWs explicitly by coupling an online ray tracer directly to the GCM. This parameterization is, however, too computation-cost intensive and, thus, no valid option for climate simulations of time periods longer than a few weeks or months. Further investigation of alternative approaches is therefore needed. In particular, a more cost-efficient, approximate parameterization of the horizontal momentum transport could provide the missing link between today's GCMs and fully resolving long-term projections in the future.

For a comprehensive description of the lateral momentum transport of MWs, two steps are needed: the source characteristics and distribution have to be estimated from the topography and the propagation behavior in given atmospheric conditions needs to be modeled. Bacmeister (1993); Bacmeister et al. (1994) investigated topography data sets in search of MW sources, or mountain ridges, for a better representation of clear air turbulence and wave drag directly above the mountains. They, however, did not look further into the excited MW parameters other than the involved GWMF. There have been some follow-up studies

on this mountain wave source database by, e.g., Eckermann and Preusse (1999) and Jiang et al. (2004). However, a quantification of the general horizontal propagation of MWs from their sources was not studied explicitly. A combination of MW source data and propagation modeling via, e.g., ray tracing could be used for the improvement of orographic GW parameterization schemes.

As we see, an accurate characterization of GWs in the middle atmosphere is inevitable for precise sub-seasonal to seasonal predictions and long-term climate projections. For a better understanding and quantification of these processes, modeling alone is not sufficient, and atmospheric measurements on vastly different scales are needed for verification and discovery of interactions. GWs can be observed by a vast amount of platforms and systems including satellite (e.g. Preusse et al., 2000; Jiang and Wu, 2001; Ern et al., 2004), lidar (e.g. Kaifler et al., 2017; Reichert et al., 2021), infrared airglow imager (e.g. Suzuki et al., 2007), meteor radar (e.g. Stober et al., 2013; Placke et al., 2015), and in-situ ballon (Vincent et al., 2007; Corcos et al., 2021) measurements of local temperature and wind profiles.

Especially satellite observations can give a good overview of the global distribution of GWMF, and thus, of the source variability (e.g. Jiang et al., 2006; Ern et al., 2016, 2018; Hindley et al., 2020). The current satellites, however, do not measure the needed quantities or lack the necessary resolution, to resolve individual wave events. Therefore, small-scale observations focusing on specific case studies are still very important for better understanding the processes of GWs and their propagation (e.g. Rapp et al., 2021; Krasauskas et al., 2023; Geldenhuys et al., 2023). The combination of observational data and specific GW modeling, e.g., ray-tracing, can lead to a better understanding of the life cycle of GWs and the horizontal momentum transport (e.g. Preusse et al., 2002; Kalisch et al., 2014; Strube et al., 2021; Geldenhuys et al., 2021). The observations are, thus, an essential part of restraining atmospheric models, thereby reducing uncertainties in the underlying physical processes and climate projections. In particular, they are necessary for the validation and tuning of MW parameterizations within GCMs.

The aim of this thesis is to take further steps in the understanding of MW propagation by combining a reliable MW source-finding algorithm with the well-tested propagation model

GROGRAT (Marks and Eckermann, 1995; Eckermann and Marks, 1997). Furthermore, this thesis explores possible paths for the improvement of parameterization schemes using the modeled propagation behavior. A reliable estimation of the MW source spectrum and localization on a global scale is essential since this gives the lower boundary condition for the propagation model. The necessary parameters include the orientation and displacement, i.e. the mountain height, of mountain ridges as done in previous studies, and additionally, the horizontal scales excited by the orography. In particular, a mountain range could excite a full spectrum of horizontal wavelengths and not just a single monochromatic wavelength. In principle, such a spectrum could be approximated by a superposition of individual two-dimensional mountain ridges with fixed widths, lengths, and heights.

Therefore, the first question considered in this thesis is: **How to optimally approximate the elevation data by a small number of two-dimensional mountain ridges?**

The MW parameters necessary for the propagation modeling via ray tracing can be inferred from the above-established ridge database. Linear theory gives analytical solutions to how the scale, i.e. the width, and the height of a two-dimensional mountain ridge translate to the horizontal wavelength and displacement amplitude, respectively (e.g. Nappo, 2012). Thereby, we get the lower boundary condition for the ray-tracer, GROGRAT (Marks and Eckermann, 1995), directly from the ridge database. After initialization of the MWs, the ray-tracer calculates the path of the wave energy in a given background atmosphere following linear theory. Along the trajectory, all wave parameters are subject to change due to refraction, propagation, and dissipation. In particular, the wave orientation, horizontal and vertical wavelengths, and amplitude will vary along the path of the MW. The validation of such a combined model can be done by comparison of resulting residual fields from observations and high-resolution modeling, if there is a way of reliably reconstructing wave perturbations along the trajectories.

The second question considered in this thesis is: **Can the combined MWM estimate residual temperature perturbations reasonably in comparison to high-resolution model data and observations? Is the MWM able to predict global GWMF distributions?**

The combination of the source model and the propagation modeling by ray-tracing forms the mountain wave model (MWM) which is the predictive tool for horizontal MW propagation. After validation of the MWM in terms of general distribution and field characteristics, it can be applied to studying general propagation behavior and patterns of MWs. By considering multiple years of atmospheric backgrounds, propagation data representative of various conditions are generated. In turn, this is used for statistical analysis of recurring or general propagation patterns.

In this way, the following final questions will be addressed: **How to construct a transport matrix that can approximate the horizontal transport of GWMF due to horizontal propagation? Is it possible to describe the horizontal MW spread using anisotropic diffusion?**

The structure of this thesis is as follows: Chapter 2 gives a brief recapitulation of basic linear GW theory followed by a short overview of the theoretical description of MW excited by two-dimensional mountains. Both are used throughout this work and are the basis for most GW studies. After the theoretical foundation is set, the Mountain Wave Model is described in detail in Chapter 3. A brief discussion of available elevation data sets is followed by the presentation of two different approaches for the identification of idealized two-dimensional ridges in the topography. The chapter closes with the translation of ridge parameters to initial GW launch parameters needed for the ray-tracer and the description of a necessary modification to the amplitude calculation within GROGRAT to account for horizontal perturbation of the GW packets along the trajectory. Chapter 4 presents the method used for reconstructing residual temperature perturbations and GWMF distributions from the MWM-generated ray-tracing data. The residual temperature reconstruction is validated by comparisons against a Fourier transform model, high-resolution ECMWF IFS model data, and airborne lidar measurements. The reconstruction of global GWMF distributions is compared to global satellite observations. MW propagation patterns throughout the year as predicted by the MWM are presented in Chapter 5. This is followed by a study of in which way and how well the full propagation of MWs along their three-dimensional trajectories can be approximated by redistributing, i.e., relocating, horizontally confined MWs at a single altitude. In the end, a brief

glance into the propagation approximation via inferred diffusion coefficients is given. Chapter 6 closes this thesis with a final summary and an outlook of possible follow-up studies.

Chapter 2

Gravity Wave theory

Studies on gravity waves in the atmosphere, or "Luftwogen", reach back as far as the early 19th century (Wegener, 1906). It took, however, until mid-century before today's theoretical descriptions of atmospheric gravity waves, their excitation and propagation, and GW-atmosphere interactions were established. The development of the underlying theory for non-linear interactions, in particular, is still a research topic today. This chapter gives an overview of the essential theory used throughout this thesis. The following considerations include the basics of GW physics, GW propagation, and MW parameterization schemes in GCMs.

The considerations in this chapter are based on the work of Bretherton (1966); Gill (1982); Andrews et al. (1987); Fritts and Alexander (2003) and Nappo (2012).

2.1 Atmospheric stability

Internal waves in a medium need some form of stratification to allow for an oscillation, e.g., salinity in the ocean. The atmosphere is stratified in terms of density with altitude, resulting in gravity (or buoyancy) as the driving force of gravity waves. A simple schematic of the GW oscillation mechanism is shown in Fig. 2.1. If an air parcel is adiabatically displaced in the vertical and adjusts to the local background pressure, p_0, the density of the air parcel, ρ_1, can be related to the background density using the ideal gas law:

$$\rho_0 = \rho_1 \frac{T_1}{T_0} = \rho_1 \frac{\Theta_1}{\Theta_0}. \tag{2.1}$$

Since the pressure is identical, the ratio of temperatures is equal to the ratio of potential temperatures, $\Theta = T \left(\frac{p_s}{p} \right)^{\frac{R}{c_p}}$.

The force (per unit volume) on an air parcel that is displaced in a hydrostatic environment, i.e., $g\rho_0 = -\frac{dp_0}{dz}$ with the density ρ_0 and pressure p_0 of the background atmosphere, is given by the difference in density:

$$F = -g\rho_1 - \frac{dp}{dz} = g(\rho_0 - \rho_1) \tag{2.2}$$

$$= g\rho_1 \frac{T_1 - T_0}{T_0} \tag{2.3}$$

$$\approx g\frac{\rho_1}{T_0} \left(\Gamma - \frac{dT_0}{dz} \right) \xi = -\rho_1 N^2 \xi. \tag{2.4}$$

Therefore, the vertical force on the air parcel is proportional to the temperature difference between the surrounding and the air parcel after adiabatic expansion or compression when adjusting to the local pressure. $\Gamma = -\frac{g}{c_p} \approx -9.8\,\mathrm{K\,km}^{-1}$ is the dry adiabatic lapse rate, ξ is the vertical displacement, and N is the Brunt-Väisälä, or buoyancy, frequency. N^2 can also be written in terms of the potential temperature, and in terms of the density gradient, if the Boussinesq approximation, i.e., assuming an incompressible air parcel other than for the buoyancy, is considered (e.g. Nappo, 2012):

$$N^2 = \frac{g}{T_0} \left(\frac{dT_0}{dz} - \Gamma \right) = \frac{g}{\Theta_0} \frac{d\Theta_0}{dz} \approx -\frac{1}{\rho_0} \frac{d\rho_0}{dz}. \tag{2.5}$$

In analogy to a simple harmonic oscillator, is the frequency of the oscillatory movement if the air parcel is displaced in the vertical only. The corresponding wave equation is simply $\frac{d^2\xi}{dt^2} + N^2\xi = 0$.

The Brunt-Väisälä frequency is closely related to the atmospheric stability and the gen-
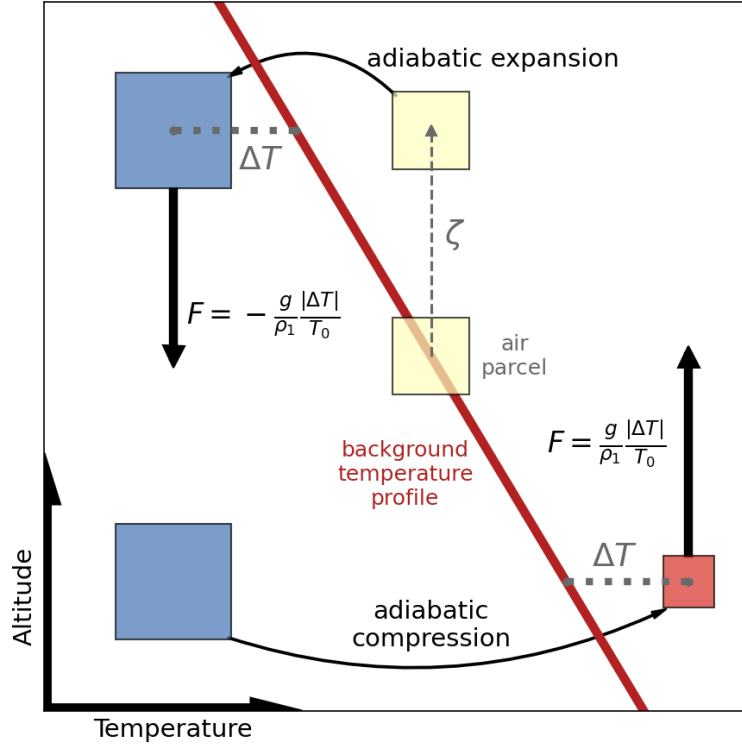
Figure 2.1: Schematic of the gravity wave excitation process upon an initial displacement of the air parcel by ζ. The oscillation is possible as long as the vertical gradient of the background temperature (red line) is higher than $\Gamma = -\frac{g}{c_p} \approx -9.8\,\mathrm{K km^{-1}}$.

eration and propagation of GWs. For $N^2 > 0$, the atmosphere is stable, and the oscillation frequency, N, is real, permitting GW excitation. Stability occurs if the temperature gradient is higher than Γ and the upward displaced air parcel cools down more than the background and ends up colder than the surrounding; therefore, denser. The opposite is the case if $N^2 < 0$: the oscillation frequency will be imaginary, the air parcel movement will shrink or grow exponentially, and no GW is excited. The atmosphere is unstable in this case. A prime example is convection, where a once displaced air parcel inexorably rises.

Typical values for the Brunt-Väisälä frequency are $N \approx 0.01\,\mathrm{s^{-1}}$, or a period of about 10 minutes, in the troposphere and $N \approx 0.02$ s^{-1}, or a period of about 5 minutes, in the stratosphere. In general, the transition at the tropopause is comparatively sharp, leading to partial reflection of GWs.

2.2 Linear theory

In the previous section, a very simplified wave equation arose by restricting the consideration to solely vertical movement of the air parcels. For a more realistic description, horizontal oscillations as well as effects of the Coriolis force need to be considered. To find the corresponding wave equation, the system of equations of motion for momentum, energy, and mass conservation are set up in the hydrostatic, linear approximation, i.e., all quantities are assumed to have the form Fritts and Alexander (2003):

$$q(\boldsymbol{x}, t) = q_0(z, t) + q_1(\boldsymbol{x}, t), \tag{2.6}$$

$$q_1(\boldsymbol{x}, t) = q_A e^{i(\boldsymbol{k} \cdot \boldsymbol{x} - \omega t) + \frac{z}{2H}}. \tag{2.7}$$

Here ω is the ground-based frequency of the GW, $\boldsymbol{k} = (k, l, m)$ the wave vector, and H the density scale height. In this framework, the perturbations, q_1, are purely caused by a singular wave. Any terms higher than the first order in the perturbations $q_1(\boldsymbol{x}, t)$ are dropped from the considerations. Therefore, the linear approximation neglects all possible interactions between different waves and self-interactions, which both could be of importance for high amplitude GWs of different scales (e.g., Heale and Snively, 2015; Bölöni et al., 2021).

Combining the linearized equations of motion results in the general wave equation for the vertical wind perturbation amplitude, w_A. The resulting equation is the Taylor-Goldstein equation of the form $\frac{d^2 w_A}{dz^2} + m^2(z)w_A = 0$, governing the propagation of linear GWs. The vertical wavelength depends on gradients of the background wind; therefore, it yields plane waves only in a constant background atmosphere.

To circumvent the limitation imposed by the full Taylor-Goldstein equation, an approximation is considered. In the case of slowly varying background fields compared to the GW perturbation. In physical terms, this means that the background winds may not change much in the vertical within one vertical wavelength and in time within one period. The resulting approximation is the WKB (Wentzel-Kramers-Brillouin) limit and the standard limit for most GW considerations. In this approximation, the dispersion relation for GWs can be calculated

to:

$$\hat{\omega}^2 = \frac{N^2(k^2 + l^2) + f^2\left(m^2 + \frac{1}{4H^2}\right)}{k^2 + l^2 + m^2 + \frac{1}{4H^2}}. \tag{2.8}$$

This gives the intrinsic frequency $\hat{\omega} = \omega_{\text{gb}} - ku - lv$, which is the frequency of the GW for an observer moving with the background flow. $f = 2\Omega \sin(\theta)$ is the Coriolis frequency at latitude θ with the Earth rotating at frequency Ω. This dispersion relation is a central equation of GW theory.

The different perturbation quantities of a GW are linked by the polarization relations (Fritts and Alexander, 2003, e.g.,). The ones of most importance to this thesis are

$$T_1 = -i\frac{N^2}{g\hat{\omega}}w_1, \tag{2.9}$$

$$w_1 = -i\hat{\omega}\zeta_1, \tag{2.10}$$

where T_1, w_1, and ζ_1 are the perturbations in temperature, vertical wind, and displacement, respectively.

From the polarization relations, phase differences between the quantities become evident. The wind perturbation is follows the temperature perturbation and leads the displacement perturbation by 90°. Furthermore, the horizontal and vertical winds are either in phase or 180° out of phase, and the density perturbation, ρ_1, is always 90° ahead of the vertical wind perturbation.

2.3 Wave propagation

As seen in Sec. 2.2, GWs are oscillations $\propto \exp(imz)$, with the vertical wavelength m that can be calculated by reordering Eq. 2.8. There are two distinct regimes of GWs: either $m^2 > 0$, resulting in m being real and an oscillation of perturbations in the vertical arises, or $m^2 < 0$, leading to imaginary m, which translates to exponentially decaying or growing perturbation with height. Since we require boundedness of our solutions, only the decaying part is a real

solution to consider here. Furthermore, an ever-growing perturbation would violate energy conservation. Therefore, $m^2 < 0$ results in a fixed phase (in the vertical) perturbation with exponentially decaying amplitude away from its source. In this case, the GW is

$$\hat{w} \propto e^{imz} = e^{-qz}, \qquad q > 0, \tag{2.11}$$

where $q = |im|$ is the damping rate of the perturbation. These types of waves are called "evanescent" in contrast to "propagating" GWs. A GW can become evanescent during its lifetime due to changing background conditions, that do not allow for its vertical propagation anymore, or the initial conditions could not allow for a propagating GW in the first place. The former case corresponds to the total reflection of the GW. Note that the phase of evanescent GWs still varies in the horizontal.

Propagating GWs with $m^2 > 0$, on the other hand, carry momentum in the direction of the group velocity. The group velocity is given by derivation of the (ground-based) frequency, i.e., the dispersion relation in Eq. 2.8, by the corresponding spectral component:

$$(c_{gx}, c_{gy}, c_{gz}) = \left(\frac{\partial \omega_{gb}}{\partial k}, \frac{\partial \omega_{gb}}{\partial l}, \frac{\partial \omega_{gb}}{\partial m} \right) \tag{2.12}$$

$$= (u_0, v_0, 0) + \frac{\left(k(N^2 - \hat{\omega}^2), l(N^2 - \hat{\omega}^2), -m(\hat{\omega}^2 - f^2) \right)}{\hat{\omega} \left(k^2 + l^2 + m^2 + \frac{1}{4H^2} \right)}. \tag{2.13}$$

Note that for upward propagation, i.e., $c_{gz} > 0$, $m < 0$, and accordingly the wave vector points downward and vice versa. Further, if the limit of mid- and high-frequency GWs, i.e., $\hat{\omega} \gg f$ and $m \gg \frac{1}{4H^2}$, is considered, the horizontal and vertical intrinsic group velocities simplify to

$$(c_{gh}, c_{gz}) = \frac{Nm}{k_h^2} \frac{(m, -k_h)}{\sqrt{k_h^2 + m^2}}, \tag{2.14}$$

where $k_h = \sqrt{k^2 + l^2}$ is the horizontal wave number. In this case, the group velocity is perpendicular to the wave vector, $(k_h, m) \cdot (c_{gh}, c_{gz}) = 0$, and thus the group velocity is perpendicular to the propagation of phases. In other words, the GW propagates along the lines of constant phase, i.e., along the phase fronts.

The propagation speed of phases is given by the phase velocity, which is calculated by dividing the (ground-based) frequency by the respective wave number:

$$(c_{ph,h}, c_{ph,z}) = \left(\frac{\hat{\omega}}{k_h}, \frac{\hat{\omega}}{m} \right). \tag{2.15}$$

Hence, for an upward propagating GW ($m < 0$), the phase propagates downward. Note that the phase velocity cannot be interpreted as a vector quantity. The horizontal intrinsic phase speed, $c_{ph,h} - u_{\mathrm{par}}$, with $u_{\mathrm{par}} = ku + lv$ is an important quantity for wave propagation. If it reaches zero at any point, the corresponding GW breaks down.

2.3.1   Critical Level

An important atmospheric condition that propagating GWs might encounter along their trajectory is the critical level, which limits vertical propagation. The dispersion relation, Eq. 2.8, solved for m^2 can be written in terms the ground-based phase speed , $c_{gb} = \frac{\hat{\omega}}{k} + u_{\mathrm{par}}$:

$$m^2 = \frac{N^2 - \hat{\omega}^2}{(c_{gb} - u_{\mathrm{par}})^2 - \frac{f^2}{k_h^2}} - \frac{1}{4H^2}. \tag{2.16}$$

In the mid- and high-frequency approximation, i.e., $f \to 0$, this equation has a double pole in $c_{gb} - u_{\mathrm{par}}$. If the background wind changes and $u_0 \to c_{gb}$, $m \to \infty$. On one hand, this leads to the vertical wavelength going to infinitely short scales and thereby breaking the WKB approximation, and on the other hand, as seen in Eq. 2.13, the vertical group velocity goes to zero, the GW stalls in the vertical. In theory, this stalling prevents any GW from crossing a critical level or even reaching it and the GW will dissipate upon approaching the critical level.

The infinitesimal shortening of the vertical wavelengths when GWs approach a critical level is, however, not seen in observations and high-resolution models. In particular, lidar measurements during the SouthTRAC campaign show a complete vanishing of the GW below the critical level without strong wavelength attenuation (Krasauskas et al., 2023).

GWs of various phase speeds exist, which encounter critical levels at different winds and thus, this is a very common dissipation reason throughout the atmosphere. For orographic GWs, which are stationary w.r.t. the ground and therefore have $c_{gb} = 0$, the critical level is located where the wind (projected onto the wave vector) stops. Specifically, this is the case at the wind reversal at about $20\,\mathrm{km}$ in the summer hemisphere, which filters orographic GWs and prevents them from reaching the higher atmosphere.

2.3.2 Ray-tracing equations

The propagation of GWs through the background atmosphere can be described using ray-tracing theory. In this framework, the GWs are considered as monochromatic wave packets following the flow of energy, i.e., the group velocity. The methodology and equations for GWs have been derived by Lighthill (1978) and applied by Marks and Eckermann (1995). The general equations for GW packet propagation are given by the time evolution of location and wave vector:

$$\frac{dx_i}{dt} = \frac{\partial \omega}{\partial k_i}, \qquad\qquad \frac{dk_i}{dt} = -\frac{\partial \omega}{\partial x_i}. \qquad (2.17)$$

Here x_i and k_i are the components of the position and wave vector for $i = 1..3$, respectively.

The first equation gives the group velocity, which was already shown in Eq. 2.13, and describes the path of the wave packet in spatial space. The second equation describes the time development of the corresponding wave vector in spectral space and, thereby, the refraction and turning of the GW. As an example, the explicit relation for the vertical wave number is given by

$$\frac{dm}{dt} = -k\frac{\partial U}{\partial z} - l\frac{\partial V}{\partial z} - \frac{\frac{\partial N^2}{\partial z}(k^2 + l^2) - \frac{\partial \alpha^2}{\partial z}(\hat{\omega}^2 - f^2)}{2\hat{\omega}(k^2 + l^2 + m^2 + \alpha^2)},$$ (2.18)

where $\alpha = (2H)^{-1}$ with the density scale height H.

The stability and scale height are almost constant altitude (with the exception of the tropopause). Therefore, the equation can be approximated by neglecting the latter term such that the shear terms in front dominate. Now, assume an upward propagating wave with phase propagation against the mean flow, i.e., $m < 0$, $kU < 0$, and $lV < 0$. If the wind strengthens with altitude, $\frac{dm}{dt}$ will be positive, leading to an increase in vertical wavelength. A strong wind shear (or vertical gradient of the buoyancy frequency) could lead to $m \to 0$ and theoretically a sign change. Depending on the horizontal wavelength and frequency, the GW will become evanescent or totally reflected (c.f. Eqs. 2.8 and 2.16). In case of weakening winds with altitude, the corresponding change in m will be negative, leading to increasing values of $|m|$ and, therefore, shortening vertical wavelengths. As will be shown later, the shorter the vertical wavelength of a GW, the more prone it is to dissipation due to saturation. If, in any case, $m \to \pm\infty$, the group velocity will approach zero and the GW encounters a critical level. The gradient in buoyancy frequency can be high around the tropopause, where considering solely the wind shear effect is no valid approximation.

2.4   GW momentum flux and dissipation

The main interest in GWs stems from them being a mechanism of atmospheric momentum transport. The momentum carried by a GW depends on the amplitude and the horizontal and vertical wavelengths. The dissipation of GWs mostly happens via saturation and breaking processes. Upon dissipation, the carried momentum of the GW exerts a forcing on the background winds, the GW drag.

2.4.1 GW Energy, Wave Action, and Momentum Flux

The total energy carried by a GW is given by the sum of averaged potential energy due to the displacement around the equilibrium and the kinetic energy due to the up- and downward movement of the air parcel. During the oscillation, the energy shifts between potential and kinetic energy analogously to a simple harmonic oscillator. Using the polarisation relations, the total energy can be expressed by $E = \frac{\rho}{2} \frac{\omega^2}{\omega^2 - f^2} \left(\frac{g}{N}\right)^2 \left(\frac{T_A}{T_0}\right)^2$.

Note that for constant wave parameters, $E = const$ and due to $\rho \propto \exp\left(-\frac{z}{H}\right)$, the temperature amplitude grows exponentially, $T_A \propto \exp\left(\frac{z}{2H}\right)$. During the lifetime of the GW, the intrinsic wave parameters may change, thereby changing the total energy along the GW path. Thus, the GW energy is not a conserved quantity, and the wave action density $A = \frac{E}{\omega}$ is oftentimes considered, which is conserved except for dissipative processes (Bretherton, 1969) following:

$$\frac{dA}{dt} + \nabla \cdot (\boldsymbol{c_{g,gb}} A) = 0. \tag{2.19}$$

In addition, the vertical flux of horizontal momentum of a GW can be calculated from the wave action density A. These quantities are the most common measures of GW activity, as the vertical gradient describes the ac- or deceleration of the background wind due to GW breaking, which is the most important direct effect of GWs in the atmosphere. It is also called the gravity wave momentum flux (GWMF) and is calculated via

$$(F_x, F_y) = c_{g,z} A (k, l) = \rho \left(1 - \frac{f^2}{\hat{\omega}^2}\right) (\overline{u_1 w_1}, \overline{v_1 w_1}) \tag{2.20}$$

$$= \frac{\rho}{2} \frac{(k, l)}{m} \left(\frac{g}{N}\right)^2 \left(\frac{T_A}{T_0}\right)^2 \tag{2.21}$$

for the zonal and meridional momentum flux, respectively. In the last term, the polarisation relations are used again to represent the GWMF in terms of the GW parameters (Ern et al., 2004).

This transport happens mainly in the vertical but, as was shown previously, depending on the wind conditions and wave parameters, can also occur in the horizontal (Kruse et al., 2022). GWs pick up momentum on excitation and possibly along their lifetime through refraction (Geldenhuys et al., 2023). On the other hand, they release the momentum to the atmosphere by dissipation processes like, e.g., saturation or encountering critical levels.

If a GW breaks, the momentum is released locally and cascades to small-scale turbulence (c.f. Baumgarten and Fritts, 2014; Fritts et al., 2014). The net effect of the generated turbulence is an ac- or deceleration of the background winds. The net acceleration is described in terms of the GW drag, which relates to the vertical gradient of GWMF:

$$(D_x, D_y) = -\frac{1}{\rho_0}(\frac{dF_x}{dz}, \frac{dF_y}{dz}), \tag{2.22}$$

where D_x and D_y are the background wind acceleration, or drag, in the zonal and meridional direction, respectively. This direct effect on the wind speed is a cause and contributor to large-scale dynamical processes like the Brewer-Dobson-Circulation and the Quasi-biennial oscillation.

Although this dissipation of energy by ac- or deceleration of the background wind is the most common way of modeling momentum loss of GWs, there is a possibility that secondary (or tertiary) GWs are excited upon breaking. This process is difficult to observe directly in the atmosphere but is strongly motivated by theory (e.g. Voelker et al., 2021). In particular, there are multiple studies on this topic combining theory and high-resolution models with mesospheric radar observations of supposedly non-primary waves (e.g. Vadas et al., 2003, 2018; Vadas and Becker, 2018, 2019).

2.4.2 Saturation

Saturation theory describes the physical limit for GW amplitude growth under realistic background conditions. As shown in the previous section, the temperature amplitude grows exponentially in a constant background atmosphere, $T_{\mathrm{amp}} \propto \exp\left(\frac{z}{2H}\right)$ with the atmospheric

density scale height $H = \frac{R_{\text{spec}} T_0}{g} \approx 7 \, \text{km}$ for the middle atmosphere.

A simple approach for describing GW saturation is based on the stability criterion, $N > 0$, which translates to the condition that the vertical temperature gradient is larger than the atmospheric lapse rate Γ. Otherwise, the atmosphere becomes locally unstable and does not allow the existence of propagating GWs anymore. This type of GW saturation was first proposed by Lindzen (1981) and used to explain momentum deposition in the middle atmosphere (e.g. Matsuno, 1982). This kind of saturation is also called the (vertical) static stability saturation scheme.

An example of a GW saturating in this way is shown in Fig. 2.2. The temperature profile of the GW perturbation and the enveloping GW amplitude are shown in panel a. Panel b shows the vertical temperature gradient. The red triangles in panel a mark the altitudes, where the temperature gradient falls below the atmospheric lapse rate, Γ.

The maximum allowed amplitude within this static stability scheme can be estimated from the stability criterion, $\frac{dT}{dz} = \frac{dT_0}{dz} + \frac{dT_1}{dz} \stackrel{!}{>} \Gamma$, to:

$$\Leftrightarrow \frac{dT_1}{dz} = T_{\text{amp}} m \cos mz \stackrel{!}{>} -T_0 \frac{N^2}{g} \tag{2.23}$$

$$\Rightarrow T_{\text{amp}} \stackrel{!}{<} \frac{N^2 T_0}{g|m|} = \frac{N^2 T_0}{2\pi g} \lambda_z. \tag{2.24}$$

Note that GWs of longer vertical wavelengths λ_z induce a smoother temperature gradient; therefore, allowing for higher amplitudes. If the amplitude of a GW becomes larger than this limit, it generates local convective instability.

The saturation limit can be further refined for dynamical Kelvin-Helmholtz instabilities, which could occur before convective saturation for low-frequency GWs. This consideration accounts for the wind oscillations induced by the GW via the Richardson number, Ri. Local dynamic stability requires
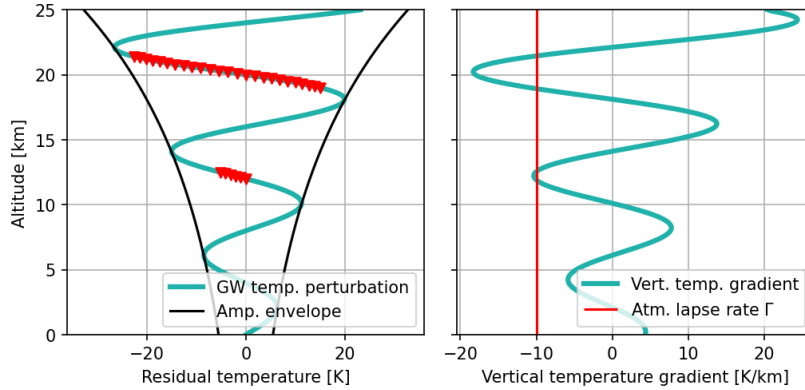
Figure 2.2: Panel a shows the GW amplitude growing exponentially with altitude at a rate of $\exp\left(\frac{z}{2H}\right)$. Black lines show the envelope, and red triangles show where the GW generates local convective instability. Panel b shows the temperature gradient due to the temperature perturbation of the GW (cyan) and the atmospheric lapse rate for dry air (red). The atmosphere is convectively unstable, where the temperature gradient of the perturbed field drops below the lapse rate.

$$\mathrm{Ri} = \frac{N^2}{\left(\frac{\partial u}{\partial z}\right)^2} > \frac{1}{4}, \tag{2.25}$$

where the denominator is the vertical shear of the horizontal background and perturbation wind. The Richardson number, as a measure of the importance of buoyancy compared to the shear stress, has a central role in the theory of turbulence (e.g. Gossard and Hooke, 1975).

Since GWs consist of both perturbations of the background temperature and horizontal wind, they alter the local Richardson number twofold. This consideration, therefore, sets a more conservative boundary on the amplitude of a GW depending on the dynamic stability. For $\mathrm{Ri} < 0$, GWs generate convective instability, as seen before, and for $0 \leq \mathrm{Ri} \leq \frac{1}{4}$ they generate dynamical instabilities. Note that in mid-frequency approximation, $N^2 \gg \omega^2 \gg f^2$, the convective instabilities dominate and the above considerations give no lower boundary for the GW amplitude; therefore, the saturation amplitude is equivalent to the convective limit shown previously. The dynamical saturation was first introduced by Fritts and Rastogi (1985) and is still commonly used within GCMs and GW modeling.

The exact physical process of what happens to a GW upon saturating is still unknown.

The typical notion is that the GW propagates further with a reduced amplitude that does not break stability, the saturation amplitude, which is also seen in observations (e.g. Vargas et al., 2019). This approach is used by, e.g., the ray-tracer GROGRAT (Marks and Eckermann, 1995). From further observations, however, it might also be reasonable that GWs (especially with very high amplitude) break down completely once they hit saturation (Kaifler et al., 2015), while theory allows for amplitudes of up to 50% beyond the saturation limit (Lindzen, 1988). In any case, saturation leads to a reduction in the amplitude and total energy of the GW and, thereby, a forcing of the background winds.

2.5 Orographic Gravity Waves

Orography is one of the most common and best-observed GW sources. Orographic GWs, or mountain waves (MWs), are excited if the ground-level winds are sufficiently strong to pass over the mountains. MWs make up a large part of the global GW distributions and are the dominating GW type in the polar regions, especially during winter. Therefore, they are especially important for considerations of SSWs and polar vortex breakdowns. Due to the seasonally reversing winds in the polar stratosphere, they encounter critical levels and deposit their momentum at different altitudes throughout the year. Due to this behavior, MWs drive different branches of the Brewer-Dobson circulation depending on the season.

2.5.1 Modeling of Orographic Gravity Waves

Mountains serve as a stationary obstacle that redirects the incident wind upwards. If the wind flow is strong enough to cross the mountaintop, the air will undergo vertical upward displacement along the flow, and thus, a GW is excited. Since the mountain is stationary, the ground-based frequency of excited MWs will be zero and the intrinsic frequency is:

$$\hat{\omega} = \omega_{gb} - u_0 k = -ku_0. \tag{2.26}$$

Here k is the horizontal wavenumber and u_0 is the wind speed perpendicular to the

24

mountain ridge. Therefore, the consideration is limited to the two-dimensional case. The corresponding intrinsic phase speed of the MW is identical to the wind speed $c_{ph} = -u_0$ but in the opposite direction. Note that because of $\hat{\omega} \overset{!}{>} 0$, MWs are always directed against the incident flow.

Another point worth mentioning is that MWs encounter a critical level, where $u_0 \to 0$, and are therefore sensitive to wind reversals in the atmosphere, e.g., in the summer-hemispheric stratosphere.

In the following, we will consider an idealized two-dimensional mountain with a Gaussian shape and derive the excited MW spectrum. The topography shape is given by:

$$h(x) = He^{-\frac{x^2}{2a^2}}. \tag{2.27}$$

In a first approximation, the incident wind on the surface can be assumed constant if the orographic elevation is small compared to the horizontal extent. The induced vertical wind perturbation at the surface is then given by

$$w_1 = u_0 \frac{dh}{dx}. \tag{2.28}$$

The MW spectrum at the surface is calculated via Fourier transformation of Eq. 2.28 using this lower boundary condition. With the Gaussian-shaped mountain given in Eq. 2.27, the Fourier transformation becomes:

$$\hat{w}(k, 0) = u_0 \, \mathcal{F}\left[\frac{dh(x)}{dx}\right] = iu_0 k \, \mathcal{F}\left[h(x)\right] \tag{2.29}$$

$$= iu_0 H k\sqrt{2\pi}a e^{-\frac{k^2 a^2}{2}}. \tag{2.30}$$

This equation shows that a Gaussian-shaped mountain excites a full spectrum of MWs and not just a single mode. The resulting wave packet is a superposition of all these spectral
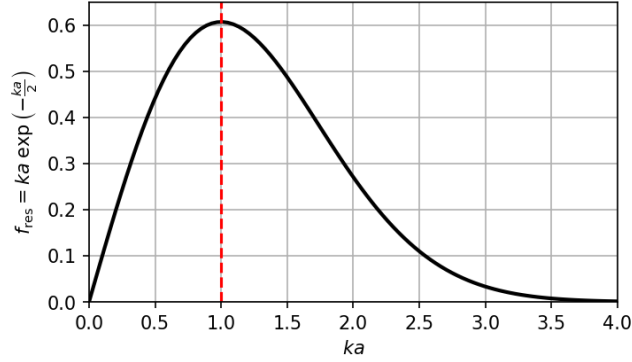
Figure 2.3: Frequency response function of a Gaussian-shaped two-dimensional mountain. The global maximum is located at $ka = 1$, or for $\lambda_{\mathrm{hor}} = 2\pi a$.

modes. The relative weight of each of these modes in the wave packet is given by the response function $f_{\mathrm{res}} = kae^{-\frac{k^2 a^2}{2}}$.

The shape of the response function is shown in Fig. 2.3. It has a rather steep slope towards the global maximum, located at $ka = 1$, and about 56% of the total response is in the interval $0.5 < ka < 1.5$. Nevertheless, the distribution has a long tail, and a simple Gaussian mountain can excite all kinds of horizontal scales. Due to the concentration of amplitudes around $ka = 1$, a predominant horizontal wavelength can be assumed as:

$$\lambda_{\mathrm{hor}} = 2\pi a \tag{2.31}$$

The full spectrum of MW modes can be separated into a propagating and an evanescent part. As seen in Sec. 2.3, this depends on the vertical wave number being either real or imaginary. The vertical wavenumber, as from the mid-frequency limit of the dispersion relation (Eq. 2.8), is given by

$$m^2 = \frac{N^2}{u_0^2} - k^2. \tag{2.32}$$

From this, the critical wave number $k_c = \frac{N}{u_0}$ can be defined as the horizontal wavenumber

26
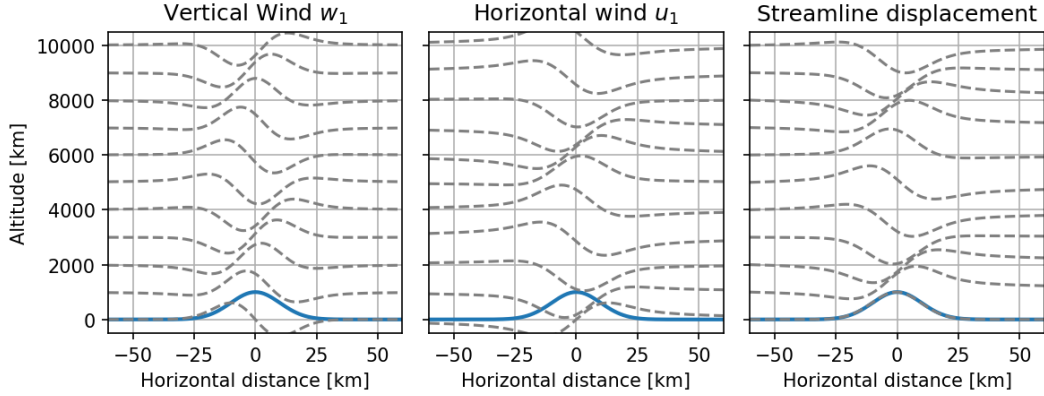
Figure 2.4: Wave perturbations above a Gaussian shaped mountain of height $H = 1\,\text{km}$, width $a = 10\,\text{km}$, in an atmosphere with stability $N = 0.01\,\text{s}^{-1}$, and surface wind speed $u_0 = 10\,\text{ms}^{-1}$. All perturbations are shifted to their corresponding altitude. Panel a shows the vertical wind, and panel b the horizontal wind perturbation. The displacement of streamlines is shown in panel c.

below which m^2 is positive and the corresponding MWs propagating. On the other hand, if $k > k_c$, the corresponding mode is evanescent, and no GW of this scale is excited.

The wave perturbation in spatial space can be calculated as the real part of the inverse Fourier transformation of the spectral amplitudes given by Eq. 2.30. Figure 2.4 shows an example of analytically calculated vertical (panel a) and horizontal (panel b) wind perturbations above a Gaussian-shaped mountain. The boundary parameters set as follows: mountain height $H = 1\,\text{km}$, mountain width $a = 10\,\text{km}$, atmospheric stability $N = 0.01\,\text{s}^{-1}$, and horizontal background wind speed $u_0 = 10\,\text{ms}^{-1}$. The dominant horizontal wavelength for this mountain would be $\approx 63\,\text{km}$. At the surface, the vertical displacement envelopes the mountain corrugation while the phase shifts with increasing altitude leading to a changing pattern. Due to the interference of all contributing wave modes, propagating as well as evanescent modes (see also Fig. 2.3), the perturbations are largely confined to the (horizontal) vicinity of the mountain with a horizontal extent of about one wavelength. Panel c shows the displacement of the streamlines above the mountain. The mountain shape is first replicated by the streamline at about $6\,\text{km}$ altitude. This agrees well with the vertical wavelength of the dominant mode, $k = a^{-1}$, which can be calculated to $\lambda_{\text{z}} = 2\pi \left(\frac{N^2}{u_0^2} - a^{-2} \right)^{-\frac{1}{2}} \approx 6.3\,\text{km}$ using Eq. 2.32.

2.5.2 Theoretical MW amplitudes

The initial displacement amplitude of the excited MW can be calculated from the lower boundary condition following $w_1 = \frac{\partial \zeta_1}{\partial t}$ and the inverse Fourier transformation above. For the Gaussian mountain in Eq. 2.27, the displacement amplitude of the dominant mode is given by

$$\zeta_A = \frac{H}{\sqrt{2\pi}} \approx 0.4H. \tag{2.33}$$

This is, however, only an upper bound for the effective displacement amplitude of the excited MW. If the wind flow is too weak, the wind might not be able to cross the mountain and a MW with a reduced amplitude is excited. To account for this effect, the ratio of kinetic to the potential energy of a displaced air parcel can be considered via the Froude number (squared), $\mathrm{Fr}^2 = \frac{U^2}{N^2 L^2}$, where U is the wind velocity, N is the atmospheric stability, and L is the displacement of the air parcel, which can be interpreted as the height of an obstacle in the path of wind flow. The wind can only flow over an obstacle and thereby excite MWs if the kinetic energy is larger than the potential energy at the point of highest displacement, which is at the peak of the obstacle. Rephrased, this requires a Froude number larger than one or rearranged for the obstacle height, L,

$$L < \frac{|U_{\mathrm{par}}|}{N}. \tag{2.34}$$

Therefore, L is the maximum obstacle height that the wind is able to cross with a given wind speed and stability. The specific amplitude of all MW sources identified by the MWM is thus strongly dependent on the surface level wind perpendicular to the two-dimensional ridge. The wind parallel to the mountain ridge is irrelevant in the conversion to potential energy since it is not deflected vertically in the idealized, two-dimensional considerations. The conversion of kinetic to potential energy is, however, not lossless. Barry (2008, pp. 72-82) discussed the

loss due to surface friction and estimated the conversion factor to be roughly 0.64. Therefore, the effective MW amplitude for a given wind speed is further reduced. Accounting for both effects, the effective displacement amplitude excited by a two-dimensional ridge in a given wind and stability can be approximated as

$$\zeta_{\text{eff}} = \min\left(\zeta_A, 0.64\,\frac{L}{\sqrt{2\pi}}\right) \tag{2.35}$$

$$\approx \min\left(\zeta_A, 0.26\,\frac{|U_{\text{par}}|}{N}\right). \tag{2.36}$$

The effective initial displacement amplitude of excited MW grows linearly with the surface-level wind speed perpendicular to the ridge until it is strong enough to cross the full height of the mountain ridge. From that point on, the initial amplitude will not grow with strengthening wind.

2.5.3 MW Parametrization

Topography can excite GWs of a wide spectrum of horizontal scales, as seen in Sec. 2.5.1. The considered range of horizontal wavelengths of propagating MWs is usually between tens and about a thousand km. While MWs of longer scales can be represented and directly simulated in current GCMs, shorter-scale MWs are too short to be resolved within the model resolution in long-term climate simulations. Typical horizontal resolutions for such a long-term climate projection are of the order of about 250 km, as in the ECHAM/MESSy Atmospheric Chemistry (EMAC) (Eichinger et al., 2023). Within this coarse resolution, at best GWs of 1000 km horizontal scale can be resolved (Skamarock, 2004). This limitation excludes all but the longest horizontal MWs, and thus, all other scales have to be parameterized within the model. The development of these parametrization schemes is a complex field of research on its own. Therefore, only a brief overview of the basics and the most prominent approaches is given here.

Today's parametrization schemes for MWs are based on the early work by Pierrehumbert (1986), Miller et al. (1989), and Baines and Palmer (1990). From this, two dominant schemes

emerged that are still widely used today: the Lott and Miller scheme (Lott and Miller, 1997) is used by, e.g., the European Centre for Medium-Range Weather Forecasts (ECMWF) operational forecasting systems and by the German Aerospace Center (DLR) EMAC chemistry-climate model. And secondly, the Kim and Arakawa scheme Kim and Arakawa (1995); Kim (1996) that is used by, e.g., the American National Centers for Environmental Prediction (NCEP).

Although the various approaches differ in the specifics of the parametrization scheme, they all aim at approximating the drag exerted by MWs launched from the sub-grid scale orography (SSO). In both of the above-mentioned schemes, the SSO is described by a few parameters (standard deviation, anisotropy, orographic slope, and orientation in the case of the Lott and Miller scheme) from which the surface stress under changing wind conditions can be calculated. The approximations of the topography are usually very generalizing and tuned to numerical simulations or even analytical solutions where they exist. For the Lott and Miller scheme, the SSO is assumed to consist of a single elliptical mountain, for which numerical simulations can be used to identify the surface stress patterns. Lott and Miller (1997) found the surface level drag to be best described by

$$(\tau_1, \tau_2) = \rho U N \mu \sigma G \left(B \cos^2 \Psi + C \sin^2 \Psi, (B - C) \sin \Psi \cos \Psi \right) \tag{2.37}$$

with $B = 1 - 0.18\gamma - 0.04\gamma^2$, $C = 0.48\gamma + 0.3\gamma^2$ from numerical simulations (Phillips, 1984) and a tuning parameter G. μ is the standard deviation, σ the slope, and γ the anisotropy of the elliptic mountain as derived from the SSO, and Ψ gives the angle between the wind directions and the main mountain orientation. τ_1 gives the drag perpendicular to the mountain ridge, i.e., in the direction of the primary axis of the mountain, and accordingly, τ_2 gives the drag perpendicular to τ_1.

Newer approaches of MW parameterizations derive the needed parameters directly from the bulk of the SSO without the need for an assumption on the intrinsic mountain shape (e.g. Kim and Doyle, 2005). In addition, the scheme described by Kim and Doyle (2005) allows for

the estimation of the SSO parameters in eight discrete directions of the incident wind, thereby possibly changing the scales under turning wind direction, whereas the parameters were fixed previously and the gravity wave drag (GWD) was solely strengthening or weakening with turning wind. In most recent studies, this parameterization scheme has been generalized to allow for arbitrary wind directions (Xie et al., 2020, 2021).

As we have seen in Sec. 2.5, even a simple Gaussian-shaped mountain excites a wide range of horizontal scales, which, in principle, lead to dissimilar GWD profiles due to different propagation and breaking behavior. Describing the SSO in each grid cell with only one single wavelength is, therefore, only a crude approximation. Recently, there has been some effort to incorporate multiple scales within the SSO into the parametrization schemes. van Niekerk and Vosper (2021) use a Fourier transformation of the SSO to estimate the whole spectrum of possibly excited wave modes. These new approaches and improvements are, however, only slowly being accepted and incorporated by the climate modeling community and most of the MW schemes in use still assume the excitation of a single wavelength in each grid cell.

Besides their flaws, orographic parametrization schemes are still an invaluable part of current GCMs and, although the resolution of these models is ever-increasing, they will remain important for long-term and ensemble simulations in the future (Sandu et al., 2016, 2019; Xue et al., 2021).

Chapter 3

Mountain Wave Model

A comprehensive algorithm for the modeling of MW propagation can be constructed by combining a MW source model with a propagation model using ray tracing. The general propagation behavior strongly depends on the initial wave parameters of the MWs and, thus, the algorithm to detect the MW sources in the elevation data is critical to the studies in this thesis. The presented work is based on the published work in Rhode et al. (2023) with some additional detail and the description of an alternative approach for ridge identification.

First, an overview of the topography datasets that have been considered for this work, and preprocessing steps applied to these is given. Following this is a description of the ridge detection algorithm using a Hough transformation that was developed and used throughout this study. An alternative approach using a genetic algorithm that did not turn out as capable is also briefly described. Finally, there is an overview of the MW parameters of the detected mountain ridges, including a description of the parameter derivation and distribution in the final ridge database. The chapter closes with considerations of the MW amplitudes: first, the initial amplitude strongly depends on the surface level flow and could be reduced in case of low wind speeds. Second, the amplitude calculation within GROGRAT has been revisited and modified to account for changes in the horizontal extent of the GW packets.

3.1 Topography data and preprocessing

The elevation data plays a major role in the detection of MW sources and therefore multiple data sets have been considered. Furthermore, directly working with the unprocessed elevation is not suitable for detecting idealized two-dimensional mountains due to the complexity of the orographic features. Therefore, the elevation is preprocessed before the ridge-finding algorithms are applied.

3.1.1 Topography data sets

There are multiple publicly available elevation data sets that could in principle be used for the MW ridge finding. In this thesis, we focus on the propagating spectrum of GWs of about 10 km and longer horizontal wavelengths. Therefore, any data set with a resolution of about 1' is suitable and data quality, i.e., the data should be free of gaps and anomalies, is of higher importance than a finer resolution.

The first considered dataset for the MW source detection is the data provided by the TanDEM-X mission (e.g. Hajnsek et al., 2020), which provides elevation data with horizontal resolutions of up to 12 m for special use. For generic scientific use, the data is freely available at a 90 m resolution. Although this data set is of very high horizontal resolution, it is not ideal for the use case of MW source detection. In coastal regions, which are typically strong candidates for MW generation due to the sudden rise in elevation, the data show strongly undulating artifacts. In addition, the coverage of the data set has quite a few gaps that need to be processed before usage (e.g. González et al., 2020). Therefore, this data set is not further considered for generating a global ridge database without intensive preprocessing. In any case, the high horizontal resolution provided by TanDEM-X is far beyond what is needed for the MW sources targeted in this study.

The National Oceanic and Atmospheric Administration (NOAA) provides the Global Land One-km Base Elevation (GLOBE) elevation data (Hastings and Dunbar, 1999; GLOBE Task Team, 1999). This data set results from a project combining elevation data from 11 sources to generate a topography field of 30" horizontal resolution, or about 1 km at the equator. Due

to the high amount of preprocessing that has already been performed during the generation of the data, it is ready to use for the ridge-finding algorithm and exhibits no gaps and anomalies.

The last elevation dataset considered here is the ETOPO1 data set which is also provided by the NOAA and publicly available for general use. The elevation is given on a 1' horizontal resolution, or about 2 km at the equator, with global coverage (Amante and Eakins, 2009). Just as the GLOBE data, this dataset has also been generated by the combination of data from multiple sources. Thus, it is free from any gaps and artifacts. The elevation data is provided as a bedrock-only version, which gives the earth-surface elevation below any ice sheets and glaciers, and as an ice-sheet version, which includes the ice thickness in the elevation. In addition, this data includes bathymetry data, which, however, is of no use to the ridge finding. The resolution of 1' in both directions is more than enough for the shortest-scale MWs considered in this study. The ETOPO data has recently been updated to 30" and 15" horizontal resolution (NOAA National Centers for Environmental Information, 2022).

The ETOPO1 data set is well suited for the application of a ridge-finding algorithm due to its lack of gaps and artifacts near the coastlines and the high resolution. It is also more recent than the GLOBE data and in further support and updated regularly. Therefore this dataset has been used exclusively in the following. To approximate the ocean surface, the negative elevations have been set to zero before further processing.

3.1.2 Topography slicing and scale separation

The topography data is given on a rectangular 1'×1' grid, which is not equidistant in terms of kilometers for adjacent longitude rows, especially at higher latitudes, and therefore not suited for further processing based on equidistance in both directions. The first processing step, before the scale separation is applied, is thus slicing the elevation data into slim bands of latitude and interpolation to an equidistantly spaced, locally Cartesian grid. For this study, the latitude bands are 10° wide, and adjacent bands overlap by 4° in order to capture also structures at the edges of the latitude bands. The resulting horizontal resolution of the interpolated grid corresponds to the meridional resolution of 1' latitude, or about 2 km, in both, longitude and latitude. This gives an approximated elevation slice that has been unwrapped from the

spherical coordinates and alleviates the stretching in lon-lat when considering distances.

To estimate multiple scales of MW sources within the elevation data, a scale separation is applied before it is searched for approximately monochromatic MW sources within these scale bands. This scale separation is applied on the previously generated equidistantly spaced grid using a bandpass filter. Two approaches have been considered: a Gaussian bandpass filter in spatial space and a Butterworth filter in spectral space. Both are implemented via

$$H_{\mathrm{bp}}(x,y) = H_{\mathrm{lp},1}(x,y) - H_{\mathrm{lp},2}(x,y), \tag{3.1}$$

where $H_{\mathrm{lp},1}$ and $H_{\mathrm{lp},2}$ are the lowpass filtered topography fields with the lower and upper scale of the bandpass interval as cutoff, respectively. In the case of the spatial Gaussian lowpass filter, the topography is convoluted with a Gaussian kernel of the given scale. For the spectral filter, the modes of the Fourier transform representing scales smaller than the target scale are set to zero with the transition following a 6th-order Butterworth curve.

An example of the resulting filtered data is given in Fig. 3.1, where a bandpass interval of 190–480 km is chosen. Negative values occur due to the definition of the bandpass in Eq. 3.1 and correspond to valleys in the considered scale interval. Both filters agree well in terms of amplitudes, scales, and localization of the filtered topography. The Butterworth filter shows some edge artifacts that can be alleviated by omitting the data edges, which is possible due to the overlapping bands of latitude generated in the previous step. In the remainder of this study, the Butterworth filtering has been used due to it being more consistent with other approaches of scale separation within atmospheric data (e.g. Strube et al., 2020).

This preprocessing results in scale-separated slices of topography data, which are much more suitable for the application of the ridge-finding algorithms described in the following section. The considered scale intervals for the ridge finding are chosen as multiplicative symmetric around a central scale λ_c, i.e., the scale intervals are given as $[\frac{\lambda_c}{a}, a\lambda_c]$. Varying a leads to a trade-off in spectral confinement of the ridges, on the one hand, and elevation height after bandpass filtering, on the other hand. By overlapping the scale intervals, the
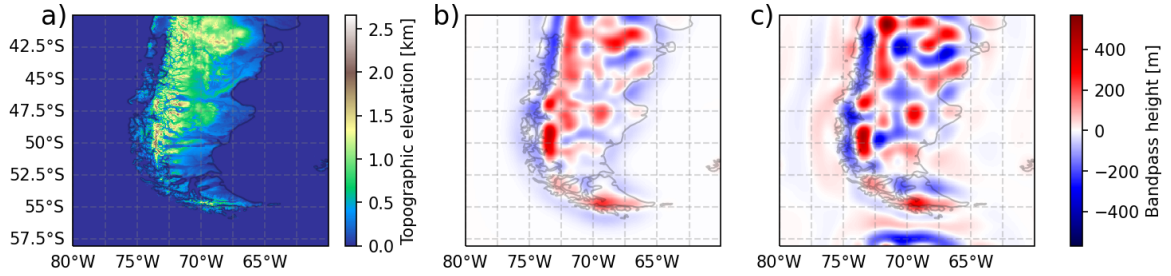
Figure 3.1: Effect of the bandpass filter on the elevation data in the Southern Andes region. Panel a shows the full topography data, and panels b and c show the result of the spatial Gaussian and spectral Butterworth bandpass filter results, respectively. The bandpass scale interval, in this case, is 190–480 km.

Interval No.	Central Scale λ_c [km]	lower boundary [km]	upper boundary [km]
1	80	50	130
2	140	90	225
3	200	125	320
4	300	190	480
5	400	250	640
6	500	310	800
7	600	410	1040
8	850	500	1280
9	1000	625	1600

Table 3.1: Scale intervals for the ridge finding covering the full MW spectrum of interest, i.e., about 40 km to around 1000 km. These intervals are used in all ridge-finding experiments throughout this thesis.

identified ridge heights are more realistic, while the detected scale stays close to the central scale. Testing showed that $a = 1.6$ yields good results. The values λ_c given in Tab. 3.1 result in a good approximation of the underlying topography and coverage of the full spectrum of orographic MWs, i.e., tens to about a thousand km horizontal wavelengths. The dense distribution of central scales ensures that all horizontal wavelengths can be sampled reliably. Potential double sampling of a mountain within multiple scale intervals is taken care of after the ridge finding.

3.2   Ridge identification

In general, a so-called ridge-finding algorithm aims to approximate the underlying topography with a relatively low number of idealized two-dimensional ridges. Two-dimensional refers to the mountain ridges being of constant height and shape along the full ridge length. Within this framework, mountain ridges are straight without any bends or curvature along their length, which is a crude approximation of realistic mountain ranges. In principle, these idealized ridges can have any profile; however, there are three often recurring shapes in two-dimensional mountain modeling: Witch-of-Agnesi (e.g. Gallus and Klemp, 2000; Jiang and Smith, 2003), Gaussian (e.g. Lott et al., 2020, 2021), and sinusoidal (e.g. Nappo, 2012) mountain ridges. All of them have been tested within this thesis.

The concept of a ridge-finding algorithm for the estimation and localization of MW sources was first introduced by Bacmeister (1993); Bacmeister et al. (1994). They presented a rather brute-force method reducing the topography to a skeleton and testing every single point for a mountain ridge. Unlike their approach, the methods presented in this thesis try to minimize the false positives, i.e., finding candidates with no underlying mountain ridge in the topography, by preprocessing the data in a way that makes ridge-like structures more readily detectable.

In the following sections, two different approaches for ridge-finding in the previously generated bandpass-filtered topography are presented. The first approach is based on the generation of a skeleton of the elevation data to the main ridge lines, which is then further analyzed using a line detection algorithm from computer vision. The second approach uses a genetic algorithm that imitates the survival of the fittest ridge collections through generations of ridge populations to approximate the given elevation with idealized mountains.

3.2.1   Line detection ridge finding

The first method for ridge identification builds on the idea that the ridgelines of mountain ranges, i.e., the trace along mountain crests, can be represented as a set of lines. Candidates for ideal two-dimensional mountain ridges will then emerge as sufficiently long, straight

segments within the skeleton.

For the application of this line detection algorithm, a skeleton representing only the ridge-lines of the elevation data has to be generated first. Afterward, straight line segments within this skeleton can be detected using a line-detection algorithm, which gives us the location and orientation of mountain ridge candidates. In this study, the Hough transform is used for the detection of straight features. At the identified locations of the straight-line features, a mountain ridge is assumed and a least squares fit optimization is performed. This tests whether the feature represents indeed a suitable mountain ridge and estimates the parameters of the structure, i.e., ridge height and width.

Ridge line skeleton

The main ridgeline of a mountain is the line connecting the points of highest elevation in the cross-mountain direction. Or, in a different formulation, the ridgeline is the collection of points, where the gradient changes sign in the direction of the gradient. The latter definition includes also valleys, which correspond to negative elevation in the bandpass-filtered topography and are therefore easily identified. Since the elevation data is a discrete two-dimensional field, the gradients can't be evaluated consistently and precisely in arbitrary directions. Therefore an approximation using four different skeletons is made. These represent the gradient changing sign in the zonal, meridional, and diagonal, i.e., south-west to north-east and south-east to north-west, directions, respectively. Each of the so-generated skeletons gives ridgelines that need to be tested for straight-line features for the respective direction.

Technically the skeleton is generated by traversing the initial field along the given direction and flagging a point if it has a higher value than the previous and next point. The collection of flagged points gives a binary skeleton where non-zero entries correspond to the ridgelines of the corresponding scale interval.

For instance, the skeleton of the bandpass filter of the Southern Andes presented in Fig. 3.1 is shown in Fig. 3.2. The ridgelines cover the main Andes mountain range well. Besides the main Andes ridge, there are a lot of ridgelines with east-west orientation to the east of the
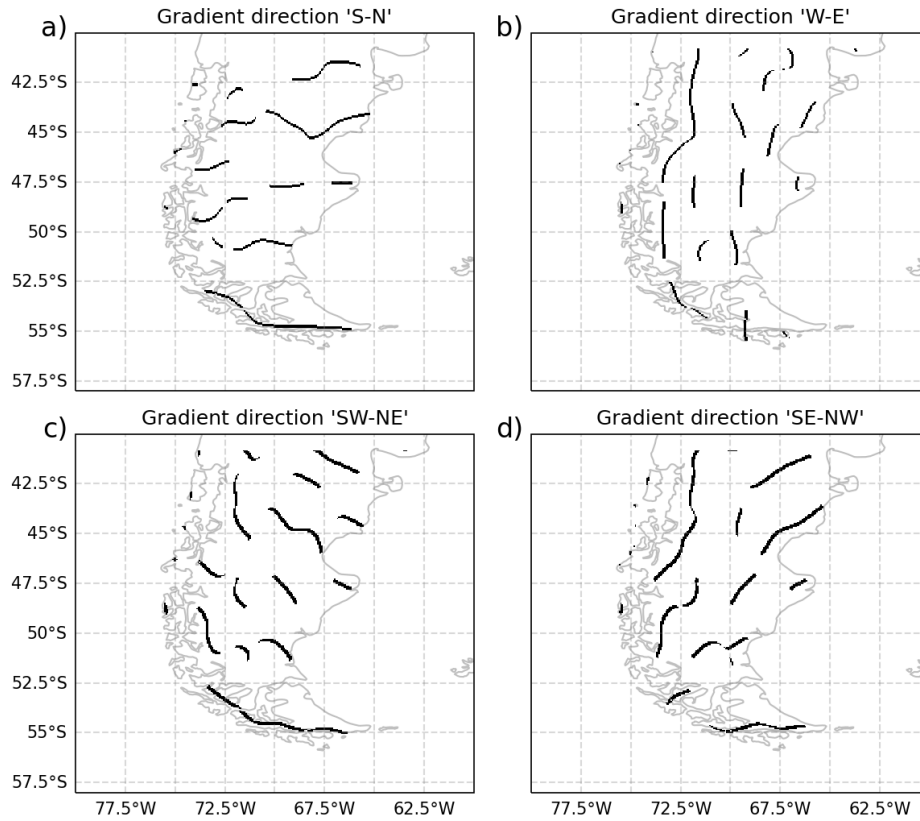
Figure 3.2: Ridgeline skeletons for the bandpass filtered topography of the Southern Andes region shown in Fig. 3.1 c. Panels a-d show the four different directions in which the local maximum detection has been performed, i.e., south-north, west-east, southwest-northeast, and southeast-northwest, respectively.

main mountain range. These correspond to lower-elevation mountain ranges at that location within the topography data. Note that all detected mountain ridge candidates are tested against the elevation data, and therefore spurious ridgelines do not lead to spurious mountain ridges in the final dataset.

Hough transformation

The next step involves detecting straight-line segments in the ridgeline skeletons generated in the previous step. A straightforward approach is to use a line detection algorithm from computer vision, the Hough transformation. This algorithm has been in use since the early work of Duda and Hart (1972) and received minor improvements and adaptations for the detection of more complex features in the meantime (e.g. Kang et al., 1991).
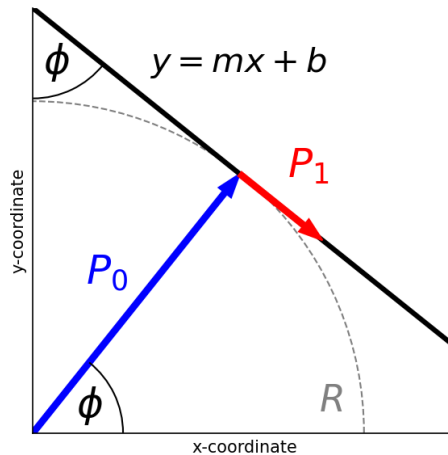
Figure 3.3: The line $y = mx + b$ can also be represented by the parameters (R, ϕ), where $R = |P_0|$. All points of the line are parameterized by $P_0 + sP_1$, with $s \in \mathbb{R}$ and a (unit) vector P_1 perpendicular to P_0.

The fundamental basis for the Hough transformation is the representation of any line by a pair of parameters in two dimensions. The most common representation of a line is given by the parameters (m, b), where m is the slope of the line and b is the intercept. All points of the line can then be represented simply via $y = mx + b$, for $x \in \mathbb{R}$. The Hough transformation uses the pair of parameters (R, ϕ), where R is the distance of the line to the origin and ϕ is the angle of the line with respect to the vertical axis. Similar to (m, b), for $m, b \in \mathbb{R}$, (R, ϕ) span the space of all possible straight lines for $R \in \mathbb{R}$ and $\phi \in [0, \pi)$. This space is also called the Hough space.

Figure 3.3 shows a schematic of these parameters for a given line. P_0 is the point on the considered line closest to the origin and further represented by R and ϕ in polar coordinates. It is important to note that the line can be parameterized by the two perpendicular vectors P_0 and vector P_1 via $P_0 + sP_1$, where $s \in \mathbb{R}$ and $|P_0| = R$. With this relation, it is easy to show that for a given point on the line, (x, y), the distance of the line to the origin can be calculated by $R = x \cos \phi + y \sin \phi$ if the angle ϕ between the x-coordinate and the perpendicular basis vector P_0 is known. By inserting $\phi \in [0, \pi)$ into this equation, the parameter pairs (R, ϕ) for all lines passing through the point (x, y) can be calculated.

Now, the general algorithm of the Hough transformation is similar to a voting procedure. Every non-zero element in the input data field casts a "vote" to every line that passes through

this point, i.e., every dark pixel of an image gives more confidence to all possible lines that it could be part of. For this, a zero-valued discrete matrix representing the Hough space is initialized that is used for counting the votes. Oftentimes, this matrix is referred to as the (Hough space) accumulator. For every non-zero entry in the data field, $R_i = R(x, y, \phi_i)$ is calculated according to the relation above for each discrete value ϕ_i of the Hough space. The corresponding entries in the accumulator of all these tuples (R_i, ϕ_i) are then incremented by one. After iterating over all points, the accumulator matrix will exhibit local maxima in R and ϕ that correspond to the detected line features in the input data field.

An example of this Hough space accumulator and the detected lines are given in Fig. 3.4. Panel a shows the input data field, or skeleton, in which the line features will be detected. Panel b shows the Hough space accumulator after the Hough transformation has been applied. The color shading gives the vote count for every pair of (R, ϕ). There are five maxima, that correspond to the lines in the skeleton in panel a. However, the maximum for line 5 is quite unpronounced because the corresponding line in panel a does not exhibit as many points in the skeleton as the other lines, and therefore it did not get as many individual votes. Nevertheless, since the parameters of this line are distinct enough from the other lines, this short line segment leads to a local maximum and is therefore detected by the Hough transformation.

A slightly improved version of this algorithm allows the extraction of line segments, including their start and end points, instead of just the parameters of infinite-length lines. This is done by an additional step of the algorithm: once any line in the Hough space accumulator receives more votes than a given threshold, a search for other connected points belonging to the same line segment is carried out. Starting with the last-processed point, the data field is traversed in both directions of the assumed line with every non-zero element along the way considered a part of the line segment until a gap of l_gap zero-valued points is encountered. Then the search ends and the corresponding last non-zero entry is set as the endpoint of the line segment. If the so-found line segment is longer than a specified minimal line length l_min, it is stored as a feature of the input image. Since this line segment has been processed completely, the votes of all points belonging to it are removed from the Hough space accumulator
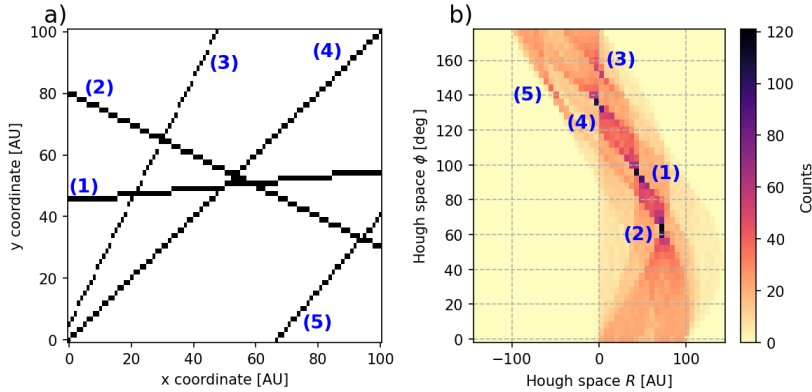
Figure 3.4: Example of the Hough transformation and the Hough space accumulator generated along the process. Panel a shows an example data field (or image) in which the main line features are detected. Panel b shows the Hough space accumulator after the Hough transformation has been applied. The five local maxima correspond to the five different line structures in the input image and are labeled accordingly in both panels.

afterward to prevent confusion between different segments along a common line.

The collection of detected lines strongly depends on the maximum line gap, l_{gap}, and the minimal line length, l_{min}. Since the ridge finding will be applied to various scales, the lengths of detected features also vary: larger-scale mountain ridges are usually wider and thus correspond to longer line segments in the skeletons as well.

The dependency of the Hough transformation on both parameters is illustrated in Fig. 3.5. The skeleton is the same as in Fig. 3.2a, i.e., for a central horizontal scale of 300 km. Panels g–i show that a too-high minimum line length reduces the number of detected line features and leads to undetected features in the skeleton. On the other hand, a too-short value possibly leads to detected lines with a much shorter length than the width, thereby fitting isotropic features instead of ideal mountain ridges (see panels a–c). In addition to the trad-off in the line length, panels c and f show an anomalous line connecting multiple features (at around 40°S, 72°W), which is detected due to the high maximum line gap. In this case, the gap between different parts of the detected line feature might be longer than the actual feature itself. In the testing performed within this thesis, the best line fitting was achieved for a minimum line length of $l_{min} = \frac{\lambda_c}{3}$ and $l_{gap} = 0.4\lambda_c$, which is shown in panel e. These values are used exclusively throughout this thesis.
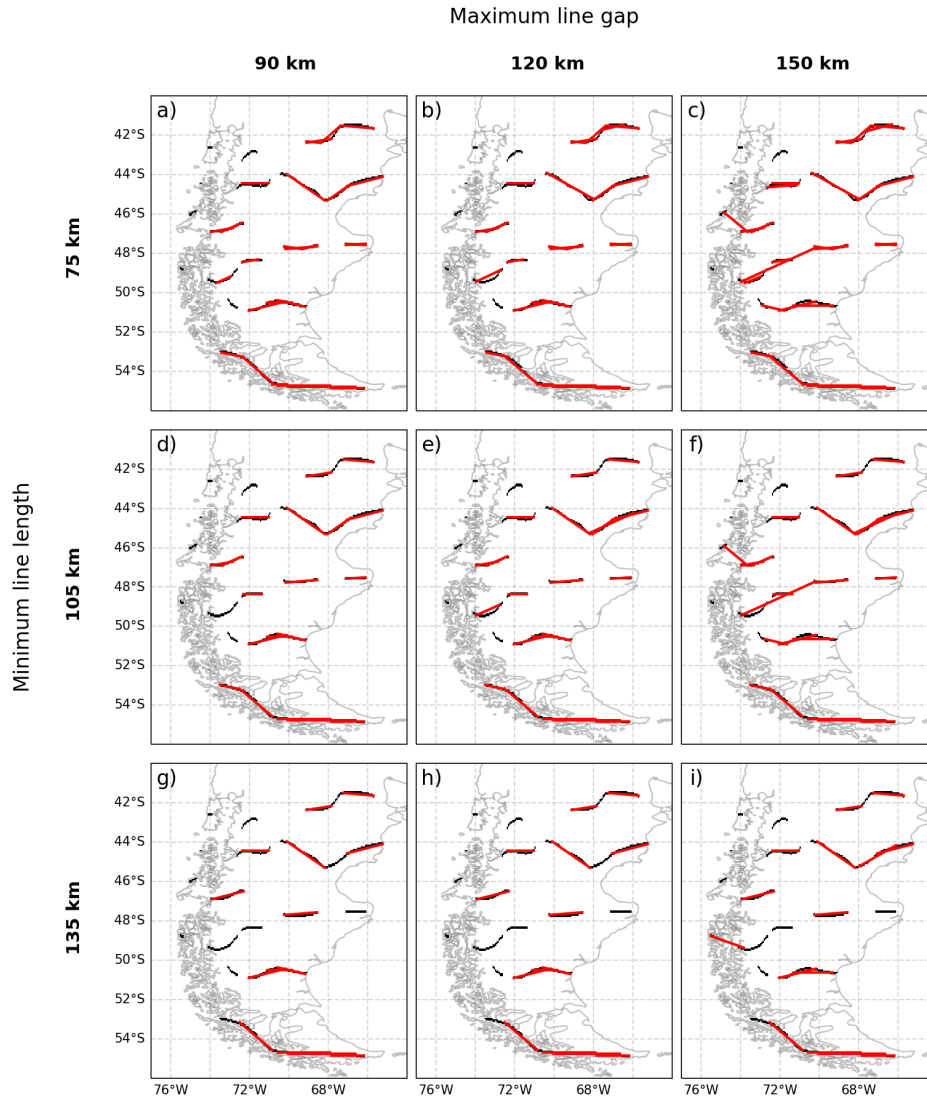
Maximum line gap

Figure 3.5: Dependency of the line detection of the Hough transformation on the parameters of minimum line length $l_{\min}$ (differs by row) and the maximum line gap l_{gap} (differs by column). The underlying skeleton is the same as shown in Fig. 3.2a, i.e., generated for a central scale $\lambda_c = 300$ km. The detected line features are shown in red on top of the skeleton.

Idealized mountain ridge fit

The line detection performed in the previous section results in a collection of line segments found in the elevation data. These line segments are candidates for idealized mountain ridges. A least squares fit tests whether the topography at the line segment location can be approximated by a two-dimensional mountain ridge. For this, the bandpass filtered topography generated in Sec. 3.1.2 is cropped and rotated such that it only includes the line segment

43

length-wise and has a width equal to the central scale used in the scale separation across the line segment. In this way, the mountain ridge in question lies centered in the cutout with a horizontal orientation.

In this cutout, the least squares difference between the elevation and an idealized mountain ridge is minimized and, in this way, the optimal parameters of the mountain ridge, i.e., height and width, approximating the topography are determined. If the approximation of the topography by the best-fitting ridge is not sufficient, i.e., if the remaining residual is too large, or the scale of the best-fitting ridge is far off the considered scale interval (which could happen, e.g., for a plateau-like elevation), the ridge candidate is dropped as a false positive. The accepted ridges are supposed to be MW sources and are stored in a ridge collection. In our testing, the number of rejected ridges, i.e., false-positive ridge candidates, is below 2%.

In general, the idealized mountain ridges could take any profile. For this thesis the following three cross sections have been tested: the sinusoidal, the Gaussian-shaped, and the Witch-of-Agnesi-shaped mountain. In combination with the spectral Butterwort filter used for the scale separation, the sinusoidal ridges performed the best in terms of representing the underlying topography. The performance is related to the scale separation by Fourier transform, which gives the bandpass filtered elevation a systematic tendency toward sinusoidal structures.

A single structure in the topography could be sampled by multiple line segments and thereby double-counted. In addition, double-counting might occur due to the overlapping scale intervals. In either case, the resulting MW activity of this region would be overestimated. To prevent this, a merging algorithm is applied before the ridge collection is accepted. In principle, this assures that out of multiple idealized ridges with approximately the same location, scale, and orientation, only the ridge best fitting to the original elevation is kept.

An example of the performance of the approximation by the so-generated ridge collection is given in Fig. 3.6. The input to the ridge-finding algorithm, i.e., the bandpass filtered topography, is shown in panel a, and the same data without the negative values is shown in panel b. The latter one is the benchmark of the ridge-finding algorithm as this should be approximated by idealized mountain ridges. Panel c shows the reconstruction from the
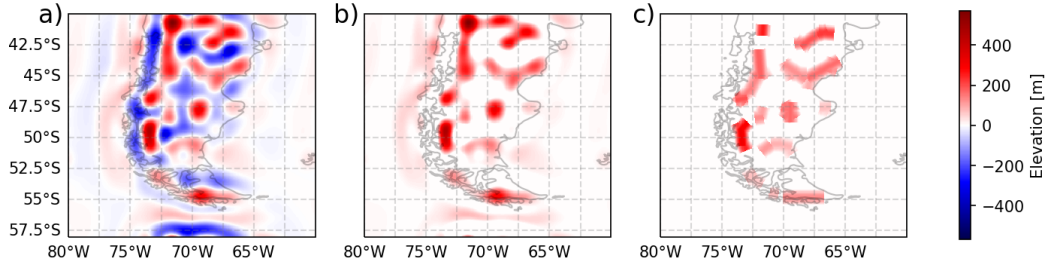
Figure 3.6: Example of the ridge identification performance of the detection algorithm based on the Hough transformation. Panel a shows the bandpass-filtered topography that should be approximated by a number of idealized straight mountain ridges and panel b shows the same topography without negative values, i.e. the mountains that are approximated. Panel c shows the reconstruction from the ridge collection extracted from the elevation data. The reconstruction approximates the elevation of panel a very well in terms of height and scales.

detected ridge collection for the single considered scale interval. The elevation is well represented by this rather small number of mountain ridges. Most of the general structures of the original field are present in the reconstruction, and the height and scales of the mountains are in agreement between both panels.

3.2.2 Genetic ridge detection

The second approach for a ridge identification algorithm explored in the frame of this thesis uses a genetic algorithm. This method resembles the "survival-of-the-fittest" from evolutionary theory by passing down well-fitting ridges through generations of ridge collections combined with random fluctuations of the parameters ("genomes").

The general idea is rather straightforward. First, a number of random ridge collections, which in the following will be referred to as "specimens", is initialized as the first generation. This is the starting point of the approximation of the underlying topography and, in general, will perform poorly in the approximation due to its random nature. A metric describing the fitness is needed in order to compare individual specimens within a generation. Since, in this case, the aim is to approximate the bandpass-filtered topography as well as possible, the fitness metric is calculated as the sum of squared differences between the ridge collection and the (bandpass-filtered) elevation data, i.e., similar to the standard root-mean-square deviation. The resulting value of this metric, the fitness, is also prescribing the hierarchy within the

generation: the lower the residuum, and thus, the higher the fitness, the better the genomes of the specimen. In this case, the genomes consist of 10 different ridges which are defined by six parameters each. The ridge parameters are longitude, latitude, height, orientation, width, and length.

The higher ranking, or fitter, specimens should have more influence on the parameters of the next generation, thereby propagating good fitting ridge collections and ridges through generations. Therefore the specimens of the new generation, which are also referred to as "children", are constructed as follows: two specimens of the previous generation are selected randomly as the "parents" with the probability of each individual specimen being a parent increasing with the fitness. Here, the lowest fitting quartile has zero chance of being a parent, and the other specimens have a probability of being selected linearly increasing with their fitness ranking. The decrease in heredity probability ensures that the best-fitting ridges are kept in the sum of all specimens, or "population", while unfit ones become extinct. The individual ridges of each child are picked at random from both parents, thereby creating a new ridge collection.

Until now, the intrinsic parameters of the ridges of each specimen are untouched. To allow for new and altered ridges, and thereby for new specimens, that might prove more fit than their parents, a random mutation of the parameters of each specimen is performed. This is implemented by randomly altering the parameters of the location, width, length, height, and/or orientation of the ridges with a random fluctuation. This step resembles the random mutation of genomes in evolutionary theory and is crucial for the emergence of better-fitting ridges within the specimens. Here, the mutation of the variables is given by a zero-centered, Gaussian-distributed probability density.

To ensure that each generation is at least as good as the previous one and to keep good specimens in the population, the specimens with the highest fitness of a generation are carried over to the next generation. A reasonable value is to carry over 10% of specimens, which allows for enough variation potential through generations in the rest of the population and simultaneously ensures the preservation of the best parameters.

An example of the 12 best-fitting specimens after 100 generations for the Southern Andes
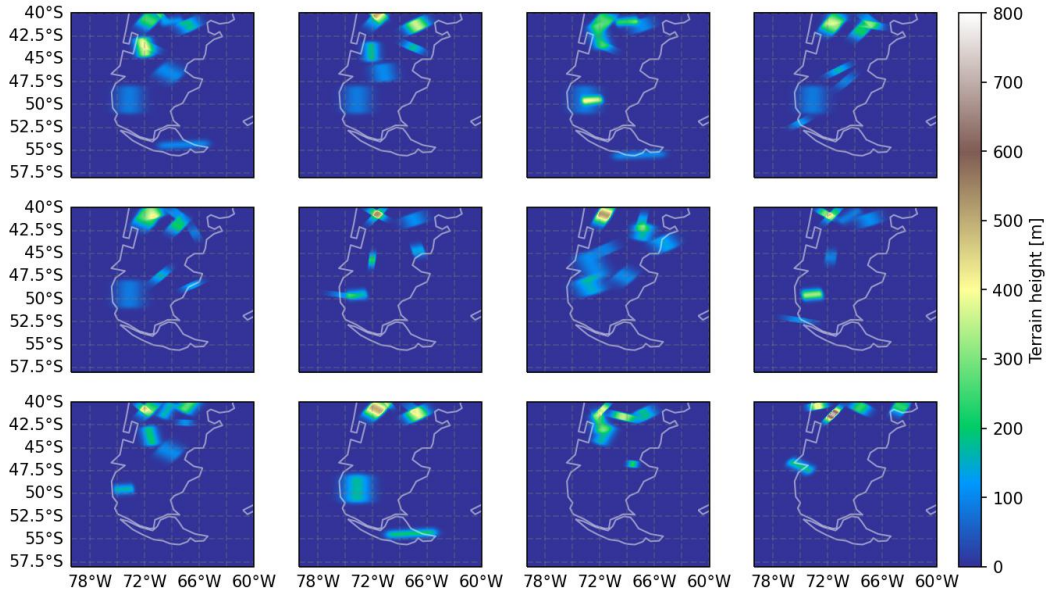
Figure 3.7: The genetic algorithm applied to the same Southern Andes region as considered in Sec. 3.2.1. Shown are the 12 best-fitting specimens (decreasing fitness from left to right, top to bottom) after 100 generations. Each generation consists of 100 specimens, and each specimen of 10 individual ridges.

region, which has also been considered in Sec. 3.2.1, is shown in Fig. 3.7. In this test, each generation consisted of 100 specimens, and each specimen of 10 individual ridges. Although the method seems very promising, the results in terms of topography approximation are lacking. Especially in comparison to the previously shown deterministic algorithm, the underlying topography is not well approximated. There are multiple reasons contributing to this. For one, the randomness in this approach is quite high. There can be different specimens with almost the same fitness, whose ridges and orientations completely differ from one another. In addition, the search space of possible values is enormously huge, even for the small example considered here. Each specimen consists of 10 individual ridges, which are each determined by 6 parameters. Therefore the dimensionality of the search space spans already 60 dimensions.

There is a certain appeal to this approach due to its elegancy and, with deeper investigations, the performance for a small region such as the Southern Andes might be improved. For the problem at hand, i.e., a global-scale ridge detection, the straightforward and more deterministic approach shown in Sec. 3.2.1 is better suited. Therefore the genetic ridge finding approach has not been used in further studies within this thesis.

Symbol	Description	Estimation from
φ	Longitude	Hough transformation
θ	Latitude	Hough transformation
α	Ridge orientation	Hough transformation
l	Ridge length	Hough transformation
h	Ridge height	Least squares fit
a	Ridge width	Least squares fit
λ_{hor}	Horizontal wavelength	$2\pi a$
ζ	Displacement amplitude	$\frac{1}{\sqrt{2\pi}}h$
ζ_{eff}	effective disp. amplitude	$\min\left(\zeta, 0.26\frac{|U_{\mathrm{par}}|}{N}\right)$

Table 3.2: Overview of all parameters provided by the ridge-finding algorithm and the step at which step they are estimated or the corresponding relation. External parameters depending on the atmospheric conditions are the low-level wind speed parallel to the (horizontal) wave vector, $|U_{\mathrm{par}}|$, and the atmospheric stability, N.

3.3 MW parameter estimation

Both ridge detection algorithms presented in Sec. 3.2 result in a collection of idealized mountain ridges. Each individual mountain ridge is assumed to be the source of a monochromatic MW, thereby launching a GW ray in the ray tracer. The initial GROGRAT launch parameters still need to be estimated from the ridge parameters. Specifically, these are the launch location (longitude and latitude), the orientation of the wave vector, the corresponding horizontal wave number, and the displacement amplitude. An overview of all parameters and at which point they are derived is given in Tab. 3.2.

The dominant wavelength and the corresponding initial displacement amplitude have been derived in Sec. 2.5.1 and Sec. 2.5.2, respectively.

With this, all parameters needed for the projection of the paths of the MWs through the atmosphere using the ray-tracer GROGRAT are estimated. The results of these calculations are investigated and analyzed in the following chapters of this thesis. For more information on the ray-tracer as a tool, refer to Marks and Eckermann (1995).

3.4 GROGRAT amplitude correction

The amplitude of the GWs along their path is predicted within GROGRAT by assuming the conservation of vertical flux of the wave action $F = c_{g,z}A$, where $c_{g,z}$ is the vertical component of the group velocity and $A = \frac{E}{\omega}$ is the wave action density (Marks and Eckermann, 1995). Eq. 4 of Marks and Eckermann (1995) gives the development of F along the ray path:

$$\frac{dF}{dt} = \frac{\partial F}{\partial t} + \boldsymbol{c_g} \cdot \nabla F = -\frac{2}{\tau} - Fc_{g,z}\nabla \cdot \boldsymbol{j}, \qquad (3.2)$$

where τ is the damping timescale accounting for radiative and turbulent dissipation and $\boldsymbol{j}$ is a scaled vector along the group velocity:

$$\boldsymbol{c_g} = c_{g,z}\boldsymbol{j} \qquad (3.3)$$

$$\Rightarrow \boldsymbol{j} = (\frac{c_{g,x}}{c_{g,z}}, \frac{c_{g,y}}{c_{g,z}}, 1) \qquad (3.4)$$

The last term in Eq. 3.2 accounts for changes in F accompanying changes in the horizontal extent of the wave packet. In a transient background field, as considered throughout this thesis, the group velocity vector of the GW can change, which leads to a deformation of the wave packet. However, the standard version of GROGRAT approximates the calculation of the vertical wave action flux by dropping this last term. In previous studies, this approximation yielded sensible results in terms of the propagation pathways (e.g. Preusse et al., 2002, 2009; Strube et al., 2021). The aim of this thesis is, however, a description of the amplitude as accurately as possible in order to reconstruct residual temperature fields and GWMF distributions. The reconstruction is very sensitive to the amplitude along the GW path and the horizontal extent of the GW packet. In addition, horizontal momentum transport is one of the main interests. Since horizontally far-propagating GWs encounter strongly varying background fields along the path, they are prone to deformations of the wave packet via refraction. Therefore, an approximation of the last term in Eq. 3.2 is proposed instead of

dropping it.

For a numerical exact calculation of the amplitude along the ray path from the vertical flux of wave action density, an involved ray-tube technique is needed (c.f. Lighthill, 1978; Marks and Eckermann, 1995). Another approach to exact amplitudes within the ray-tracing framework is to extend the amplitude calculation to the spectral space as done by Muraschko et al. (2015). However, both of these approaches are beyond the scope of this thesis. Here, a simple approximation of $\nabla \cdot \boldsymbol{j}$ is calculated analytically from the parameters at the ray path location. In this way, a ray-tube technique is approximated locally at the ray location, and the accuracy of the amplitude prediction for strongly oblique propagating GWs is improved.

Using the identity in Eq. 3.4, the term $\nabla \cdot \boldsymbol{j}$ can be calculated to:

$$\nabla \cdot \boldsymbol{j} = \frac{1}{c_{g,z}} \left(\partial_x c_{g,x} + \partial_y c_{g,y} \right) - \frac{1}{c_{g,z}^2} \left(c_{g,x} \partial_x c_{g,z} + c_{g,y} \partial_y c_{g,z} \right). \tag{3.5}$$

The partial derivatives of the individual components of the group velocity can be expressed in terms of the spatial derivatives of the background quantities, N and $\alpha = \frac{1}{2H}$, and of the intrinsic frequency, $\hat{\omega}$. Note that the latter terms correspond to the refraction terms of the ray-tracing equations, i.e., $\frac{dk_i}{dt} = -\frac{\partial \hat{\omega}}{\partial x_i}$. All of these terms are already calculated within GROGRAT and therefore need no further handling (Marks and Eckermann, 1995). The expressions of the individual terms in Eq. 3.5 are given in full length in App. A.3. The amplitude correction has been implemented in a modified version of GROGRAT that allows choosing either the standard amplitude calculation or the corrected one by option.

Testing has shown that the net effect of this correction varies strongly from one GW to another. On average, the changes in amplitude distribution of a large GW ensemble are more or less negligible. However, if the horizontal distribution is considered instead of the ensemble average, many far-propagating GWs show much-enhanced amplitudes. The resulting distributions show better agreement with the satellite observations used for validation than without amplitude correction. The following considerations in this thesis will, thus, be based on ray-tracing calculations that include the amplitude correction term.

Chapter summary

This chapter describes the mountain wave source model developed for detecting MW sources within the topography. The description closely follows Rhode et al. (2023), where the model has been initially published. The ETOPO1 elevation dataset is used for the detection of two-dimensional mountain ridges. This elevation data needs to be interpolated to an equidistantly spaced grid, and the scales in the elevation field are separated by using a spectral Butterworth filter. These steps assure the reliable detection of mountain ridges of different scales within a given domain. Two different approaches for ridge-finding are presented in this chapter: an algorithm using a line-detection method on a reduced elevation skeleton and a more brute-force genetic algorithm. The line-detection algorithm performs much better in detecting mountain ridges than the genetic algorithm, and hence, this ridge-finding method is used in the mountain wave model (MWM). Afterward, the estimated parameters of the mountain ridges are translated to GW parameters so that they can be used as the initial condition for the ray-tracer GROGRAT. The ridge identification and localization algorithm is unprecedented in this detail in the current literature.

In the amplitude prediction of GROGRAT, a term in the time development of the vertical flux of wave action density is dropped (Marks and Eckermann, 1995), leading to inaccuracies in the amplitudes of far-propagating GWs. Therefore, an approximation of the neglected term is presented, which accounts for the change in amplitude due to horizontal deformations of the GW packet that have been previously neglected. This chapter provides the theoretical basis for the MWM, which is used for studies of horizontal propagation and momentum transport of MWs in the subsequent chapters.

Chapter 4

Residual temperatures and GWMF

Before the mountain wave source model (MWM) presented in Ch. 3 can be used for further studies, it needs a validation against high-resolution atmospheric model and observation data. In the MWM, the MWs are perpetually launched at the locations prescribed by the ridge database and the corresponding initial parameters. Afterward, the propagation through the atmosphere is calculated by a ray tracer. The ray-tracing data can't be compared to other models and measurements directly, and thus, is further processed to either temperature or GWMF before the validation.

First, this chapter gives an overview of the background atmosphere used for ray tracing. Afterward, the validation via residual temperature field and global GWMF distribution reconstructions is shown. For both cases, a description of the reconstruction algorithm is given before the validation via independent data sets. In the case of temperature residual, validation against model data from a simple Fourier transform mountain wave model and a high-resolution ECMWF Integrated Forecast System (IFS) simulation is carried out. For a test against observational data, a comparison against lidar data of one flight of the South-TRAC campaign (Krasauskas et al., 2023; Rapp et al., 2021) is given. Here, the MWM can be used to identify separate wave packets and allocate them to specific source regions within the southern Andes. The global GWMF distributions are validated against HIRDLS satellite observations for January and July 2006. Beforehand, an observational filter is applied to the MWM data in order to make a reliable comparison (Trinh et al., 2015). This chapter follows

Rhode et al. (2023), where the reconstruction methodology has been first introduced and applied.

4.1   Atmospheric backgrounds

The atmospheric conditions can be described as a superposition of a zonal mean, global and large-scale waves, e.g., Kelvin and Rossby waves, and small-scale waves, e.g., gravity waves. Using a scale separation, the small-scale content of the background variables can be isolated from the large-scale background. In the middle atmosphere, the small-scale fluctuations are mostly caused by GWs, and hence, the scale separation can be used as a separation of physical processes.

The MWM needs such a scale-separated background atmosphere for two different reasons: first, the initial amplitudes of the individual MWs are strongly dependent on the low-level wind direction and speed (see Sec. 3.3) and thereby are calculated for every launch time; and second, the ray tracer requires a time-dependent background atmosphere for the calculation of the MW paths. In both cases, this background atmosphere should not contain any small-scale perturbations. A scale-separated background atmosphere restrains MWs from propagating through and interacting with the background perturbations of themselves and other GWs, which would inherently break the assumptions of linear theory used for the ray tracer.

The background atmosphere, i.e., zonal and meridional wind and temperature, used for global simulations, is exclusively constructed from ECMWF ERA5 reanalysis data (Hersbach et al., 2020; , C3S). This data set is given on a horizontal resolution of $0.3° \times 0.3°$, or about $33 \, \mathrm{km} \times 33 \, \mathrm{km}$ at the equator. The final background should contain global- and synoptic-scale structures but no small-scale perturbations like, e.g., GWs, that might be resolved in the ERA5 data (see Gupta et al., 2021). The atmospheric fields, therefore, are scale-separated following Strube et al. (2020). A zonal Fourier transform lowpass filter with a cutoff wavenumber of 18 is performed, which corresponds to wavelengths of about $2200 \, \mathrm{km}$ at the equator. Afterward, the data is filtered in the meridional direction using a 3rd-order Savitzky–Golay filter with a width of 31 data points, corresponding to about $9°$, or $1000 \, \mathrm{km}$,

window width. No vertical filter is applied to the data.

The scale-separated background is reduced to a coarser horizontal resolution of 2° latitude and 2.5° longitude, or about 220 km and 280 km at the equator. In this way, the computational requirements are reduced significantly without reducing the information content of the large-scale background. In the vertical, the model levels are interpolated to an equidistant spacing of 0.5 km. For the global-scale simulations, these atmospheric backgrounds are generated every 6 hours. GROGRAT internally uses a 4D 3rd-order spline interpolation in time and location to ensure a smooth transition between data points and time slices.

For the special case study of the SouthTRAC flight ST12, i.e., between 20.09.2019 00:00 UTC and 21.09.2019 23:00 UTC, hourly backgrounds have been prepared. The higher resolution in time allows for a more precise consideration of GW refraction and propagation, which is beneficial for the comparison of GW phase fronts to model data and observations as testing showed.

4.2 Residual temperature estimation

Since direct wind measurements within the atmosphere are sparse, there have been efforts to derive GW activity from their induced perturbations in the temperature field (e.g., Ern et al., 2004). The GW-induced perturbations can be revealed by scale separation as described in 4.1, which is valid for both model and observation datasets. The resulting small-scale features can be (partly) interpreted as GWs. A method allowing for the reconstruction of residual temperatures induced by the MWs from the MWM predictions is therefore the most direct approach for a low-level comparison to these data sets. This section describes the algorithm that has been set up for this thesis. Afterward, a basic validation of the algorithm to a simple Fourier mountain model is performed before considering the much more complex lidar and ECMWF IFS data sets for ST12 during the SouthTRAC campaign. However, note that predicting temperature residuals of GWs is very intricate due to their dependence on MW amplitude, scales, orientation, and phase, which is different from, e.g., the single values comparisons of GWMF.

4.2.1   Methodology

The reconstruction of residual temperature is possible if we assume that each MW launched by the MWM can be represented by a single wave packet propagating through the atmosphere (see Sec. 2.3.2). Within this assumption, the ray path calculated by the ray tracer gives the center of the wave packet and the GW parameters, i.e., wavelength, amplitude, and phase, at any given time. The perturbation induced by the wave packet is of finite extent, and therefore the amplitude is assumed to decrease with increasing distance from the ray path. In this way, the perturbations are localized around the ray path.

Following the theoretical MW solution in Sec. 2.5.1, it is reasonable to assume that the extent of a wave packet excited by a single mountain ridge is comparable to the horizontal wavelength and the length of the corresponding source ridge, l. Here, the perturbation is assumed to be constant along the whole length of the source ridge and only modified by a 6th-order Butterworth function, $\left(1 + (x/S)^{12}\right)^{-1/2}$, with $S = l/2$ as scale, for a smoother transition at the edges of the wave packet. A Gaussian-shaped envelope with a width set to half a wavelength is assumed along the wave vector, thereby localizing the perturbation to an interval of $\pm\lambda_{\mathrm{hor}}$ around the center of the ray path, with the perturbation dropping below 2% of the initial amplitude beyond.

The total phase of the wave is calculated from the distance to the central wave packet location and the wave vector as:

$$\phi_{\mathrm{tot}} = \phi + k_{\mathrm{hor}} d_{\mathrm{parallel}} + m d_z + \frac{c_m}{2} d_z^2, \tag{4.1}$$

where ϕ is the phase at the ray path, which is calculated by integrating the phase along the ray path (in time and space) and given by GROGRAT, $k_{\mathrm{hor}} = \sqrt{k^2 + l^2}$ the horizontal, and m the vertical wavenumber. d_{parallel} is the horizontal distance to the ray path parallel to the wave vector, and d_z is the vertical distance to the center of the wave packet. The last term accounts for small changes in the vertical wavenumber in the vertical. The vertical wavenumber is highly dependent on the wind conditions and could change rapidly with altitude, e.g., when the GW is approaching a critical level (e.g. Nappo, 2012). Therefore it is approximated

as $m(z) \approx m + c_m d_z + \mathcal{O}\left(d_z^2\right)$ with c_m calculated as the finite difference derivative of m from the ray path. This approximation gives a realistic phase throughout the spatial domain representing the phase fronts and oscillations of the GW packet.

The temperature amplitude T_{amp} calculated by the ray tracer is assumed to be the peak amplitude of the wave packet at the ray path. The total perturbation of a single MW packet is, hence, given by:

$$T = -T_{\mathrm{amp}} \cos(\phi_{\mathrm{tot}}) \frac{1}{\sqrt{1 + \left(\frac{2d_{\mathrm{perp}}}{l}\right)^{12}}} \exp\left(-\left(\frac{2d_{\mathrm{parallel}}}{\lambda_{\mathrm{hor}}}\right)^2 - \left(\frac{2d_z}{\lambda_z}\right)^2\right). \qquad (4.2)$$

Here, d_{perp} is the horizontal distance to the ray path perpendicular to the wave vector. λ_{hor} and λ_z are the horizontal and vertical wavelengths, respectively, interpolated in time along the ray path. Note that the sign is chosen such that the initial temperature perturbation above the source, where $\phi_{\mathrm{tot}} = 0$, is a negative corresponding to the positive displacement of the air parcel caused by the mountain.

A superposition of all individual contributions for all considered MWs gives the total residual temperature field, which is in accordance with linear theory.

A proof of concept for the temperature reconstruction is shown in Fig. 4.1, where temperature perturbations estimated by the above-described method and from a Fourier transform model are given side by side. The Fourier transform model calculates the wave field above a surface corrugation analytically analogously to the considerations in Sec. 2.5. Panels a and c show the resulting temperature perturbation from a Gaussian mountain with a dominant scale of 100 km and 300 km, respectively. The Fourier model accounts for the full spectrum of GWs and the resulting interference between the modes, which leads to a natural localization of the wave packet above the mountain. Panels b and d show the reconstruction of residual temperature from a single monochromatic wave packet of the respective dominant wavelength. The background atmosphere is the same in all simulations with a constant wind speed of $11\,\mathrm{ms}^{-1}$ and temperature of $292.78\,\mathrm{K}$ at the surface decreasing with altitude at a typical tropospheric temperature gradient of about $-6.5\,\mathrm{Kkm}^{-1}$. Although this atmosphere is quite unrealistic, it serves as a test of the reconstruction performance. Note that, due to the
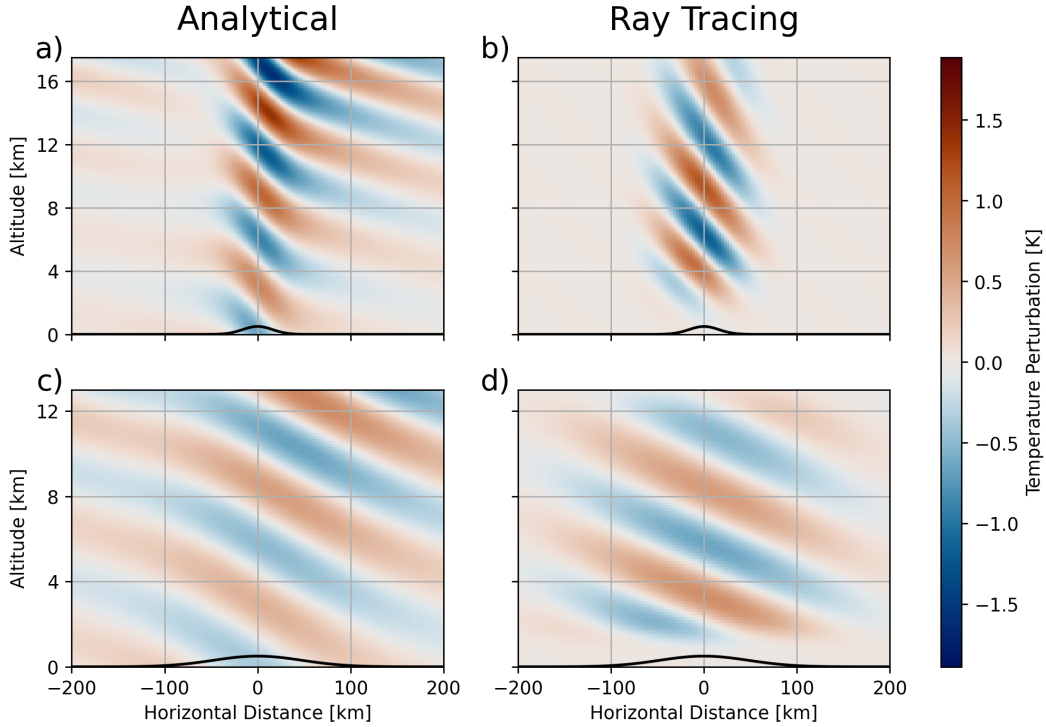
Figure 4.1: Temperature perturbation above a Gaussian mountain ridge from an analytical Fourier transform model (panels a and c) and reconstructed from ray traces of a single monochromatic wave packet (panels b and d) for different (dominant) scales of 100 km (top) and 300 km (bottom). The mountain shape is shown in black and has a height of 500 m in all simulations. Note that the Fourier transform model considers the whole spectrum of GWs excited by the Gaussian mountain instead of a single monochromatic wave.

temperature profile, the stability N decreased with altitude, which leads to a reflection of the GWs in the ray tracing simulation.

Both temperature fields agree well in terms of horizontal scales and phase, especially when considering that the ray tracer considers only a single GW mode. The amplitudes of the ray tracing simulations tend to be somewhat higher than those of the Fourier model, which, however, is not caused by the reconstruction but the initialization. The horizontal and vertical scales are virtually identical in the central column above the mountain. In the peripheral region of the Fourier transform model, intense interference of the various spectral modes excited by the Gaussian mountain leads to the localization of the GW packet mainly to an interval of about 1–1.5 wavelengths in the horizontal. This localization agrees with the findings from theory in Sec. 2.5.1 and gives confidence in the assumption made for the

reconstruction.

Note that the reconstructions from ray tracing data are generated from multiple wave packets (with the same initial parameters) launched at different times. This overlapping reconstruction is necessary since assuming an extent of about 1.5 wavelengths in the vertical does not allow reconstruction within the whole domain from a single wave packet. Since the GW packets have finite vertical group velocities and are launched at different times, they center around different altitude levels at the time of reconstruction. The (constructive) interference of the wave packets forms the seen, uninterrupted wave pattern. All of these individual wave packets fit seamlessly together.

4.2.2 SouthTRAC case studies

In more realistic case studies, the reconstructed temperature can be used as a diagnostic tool for the MWM performance. For this, the reconstructed temperature perturbations are compared to two data sets: high-resolution ECMWF IFS model data and lidar observations. For the comparison with lidar data, flight 12 of the SouthTRAC campaign (Rapp et al., 2021) is considered, which started at around 20.09.2019 23:00 UTC and ended at about 21.09.2019 05:00 UTC. During the campaign, a minor SSW event occurred such that the case studies a special situation, where the vortex is anomalously displaced (Lim et al., 2021). For more details on this flight, refer to Krasauskas et al. (2023). The large-scale ray tracing background is constructed from the ERA5 reanalysis data (see Sec. 4.1).

Comparison to ECMWF IFS

First, the residual temperatures predicted by the MWM are compared against the high-resolution ECMWF IFS data. The IFS model data is given on a horizontal resolution of $0.1°$, or about $10\,\mathrm{km}$ grid spacing, and therefore includes short-scale GWs starting at about 80 km horizontal wavelength (Skamarock, 2004). The residual temperature is separated from the background as described in Sec. 4.1 and the small-scale perturbations are considered. The MWM run is performed using hourly atmospheric background data generated from ERA5 (Hersbach et al., 2018) with MWs initialized and launched every hour to simulate the per-

petual forcing over the Andes.

Figure 4.2 shows the temperature residuals simulated by the IFS and reconstructed from the MWM for altitudes of 8, 20, and 32 km. In the troposphere, i.e., on the lowest shown level of 8 km, the scale separation is expected to perform worse in terms of isolating GW perturbations from other processes (Strube et al., 2020). Besides others, this is due to the Charney-Drazin condition that allows for higher wavenumber Rossby waves in the troposphere compared to the stratosphere, where the wind speed is typically higher. This lack of GW isolation is likely the reason for the strong temperature residuals above the Pacific Ocean, where little GW activity is expected at this altitude. In general, at this altitude, the orographic GWs are expected to be close to the topography; thus, perturbations above the ocean are likely of other origins that are not modeled by the MWM. Directly comparing the IFS to the MWM (Fig. 4.2a, b), the general shape of the wave field above the mountains agrees. Both data sets show a warm phase following along the coast of Chile with a less pronounced cold phase to the west. GWs of larger horizontal scales are seen in the sheltered Lee region. In the MWM, these MWs originate from the main Andes ridge and long-scale mountains of smaller height in eastern Patagonia. This low-elevation topography is usually not considered when investigating MWs in the southern Andes. A feature that the MWM overestimated is the northward extent of the warm phase following the coast. The IFS data does not show this beyond about 45°S, while the MWM expects this to reach north to about 35°S. Here, the temperature residuals are much more pronounced than in the IFS. Although the wave-field shape is comparable along the coast, the MWM doesn't match the high-resolution model further west, where the IFS shows much longer-scale temperature perturbations. Both data sets show very short-scale GWs in the wind-sheltered region to the east of the main Andes ridge. However, the predicted orientation is hard to compare between the models due to long-scale perturbations obscuring the temperature fields.

Well above the tropopause, at 20 km altitude, lateral propagation of MWs from their sources should be visible, and therefore spreading to regions above the ocean is expected. Indeed this can be seen in both data sets in Fig. 4.2c and d, where temperature perturbations distribute to the whole domain and, in particular, above the Atlantic Ocean. Following
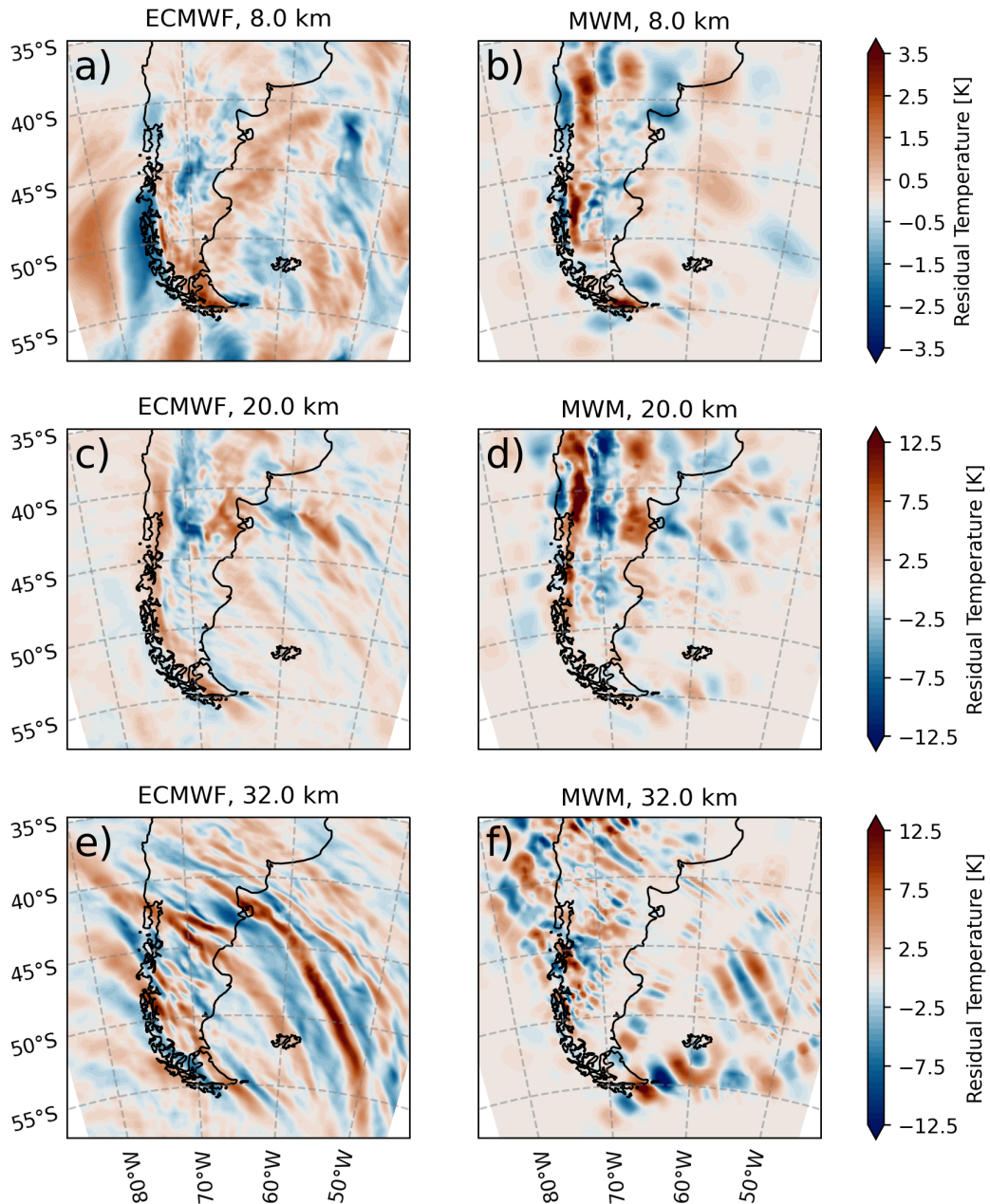
Figure 4.2: Temperature residuals over the southern Andes region as modeled by the high-resolution IFS (0.1° horizontal grid spacing, left column) and as reconstructed from individual ray traces from the MWM (right column). The horizontal temperature cuts are given at 8, 20, and 32 km altitudes for the upper, middle, and lower rows, respectively. Note the change of color scale with altitude.

GW theory, long-scale GWs propagate faster laterally than short-scale GWs. Therefore, the wave field above the oceans is dominated by large-scale features, while small-scale MWs are

located mostly above the land close to their source. Again, the general shape of the wave field is predicted well by the MWM in terms of location, scales, and orientation: the warm phases follow the western coastline from north to south, and above the Atlantic Ocean, the wavefront orientation is closer to northwest-to-southeast. The MWM, however, seems to predict too strong amplitudes compared to the IFS simulation. This overestimation might be – to some extent – physical, as the IFS is known to underestimate GW drag even at the high resolution considered here (e.g. Preusse et al., 2014; Gisinger et al., 2022; Wei et al., 2022). Another noteworthy feature is the wave packet trailing from the southeastern tip of Tierra del Fuego towards the Drake Passage. Both data sets show a similar extent of propagation, which indicates that the propagation modeling within the MWM is realistic. Although this is commonly assumed to be one of the main GW sources of the Drake Passage, at this altitude, the impact on the residual temperature is not seen as dominant here.

At 32 km altitude (Figure 4.2e, f), the wave-field characteristic changes completely. The phase fronts no longer follow the underlying orography and coastline but have turned due to a change in wind direction. The IFS shows a predominantly northwest-to-southeast orientation of the general wave field with a curving wavefront above the Atlantic Ocean. The IFS predicts high-amplitude long-scale GW perturbations above the Pacific Ocean as well (c.f. Krasauskas et al., 2023). The MWM correctly captures the general change in wave-field characteristics between 20 km and 32 km: the locations and orientation of the phase fronts agree well with the IFS simulations. However, it is evident that the simplified model has some gaps in the representation. These are a direct consequence of describing every source ridge by a single GW packet and approximating the underlying topography by a small number of mountain ridges of different scales. The GW amplitudes, on the other hand, agree well with the ones simulated in the IFS, and the propagation towards the west (above the Pacific Ocean) is correctly predicted. Similar to the lower altitudes, GWs of very short scales are located mostly above their source regions.

Overall, the MWM predicts the general wave-field characteristic well above the tropopause, while a detailed investigation reveals the limitations of the temperature reconstruction approach. The MWM describes the source distribution and propagation generally

well but not in every detail that a complex physical model, like the IFS, could provide. Such a detailed reconstruction from the topography is, however, unprecedented. The ray tracer connects each MW source to a location, where the perturbation occurs in the atmosphere. This simplified consideration gives the possibility of considering individual contributions of single mountain ranges and local sources to the observations and perturbations by isolating or removing single mountain ridges. Since the agreement of the MWM with the IFS in terms of orientation, location, amplitudes, and horizontal propagation is mostly good, the MWM can be trusted to predict coarser-grained inferred parameters like the GW momentum flux and its transport in the following studies.

Comparison to lidar observations

A second comparison is performed between the temperature reconstruction from the MWM and ALIMA (Airborne Lidar for Middle Atmosphere Research) observations. ALIMA measured the temperature above the airplane from about 2 km above flight altitude up to 60 km. Therefore, the data provides a look into the later stages of the MW lifecycle, i.e., after propagating far into the stratosphere. For an in-depth study of the ALIMA measurements, refer to Krasauskas et al. (2023) for this specific flight and Geldenhuys et al. (2023) for a further case.

Figure 4.3 shows the residual temperature perturbations as measured by the lidar (panels a–c) and as predicted by the MWM (panels d–f) for 3 of the sections of the flight (the considered legs of the flight path are shown in Fig. 4.4). The ALIMA measurements show strong perturbations throughout the curtain with a few distinct GW patterns. Especially along leg 5 (Fig. 4.3a), a strong large-scale GW has been observed above the coast of the Southern Andes (which is at about 600 km in this panel) at around 35 km altitude.

Comparing the MWM predictions to the measurements, the curtains, in general, are much less structured. However, this sparsity is at least partially caused by the lack of GW sources other than orography. As with the model data in Sec. 4.2.2, the lidar observation picks up temperature perturbations of any origin. The MWM predicts the dominant features of all the legs at the right location and with the correct scales vertically and horizontally. Only
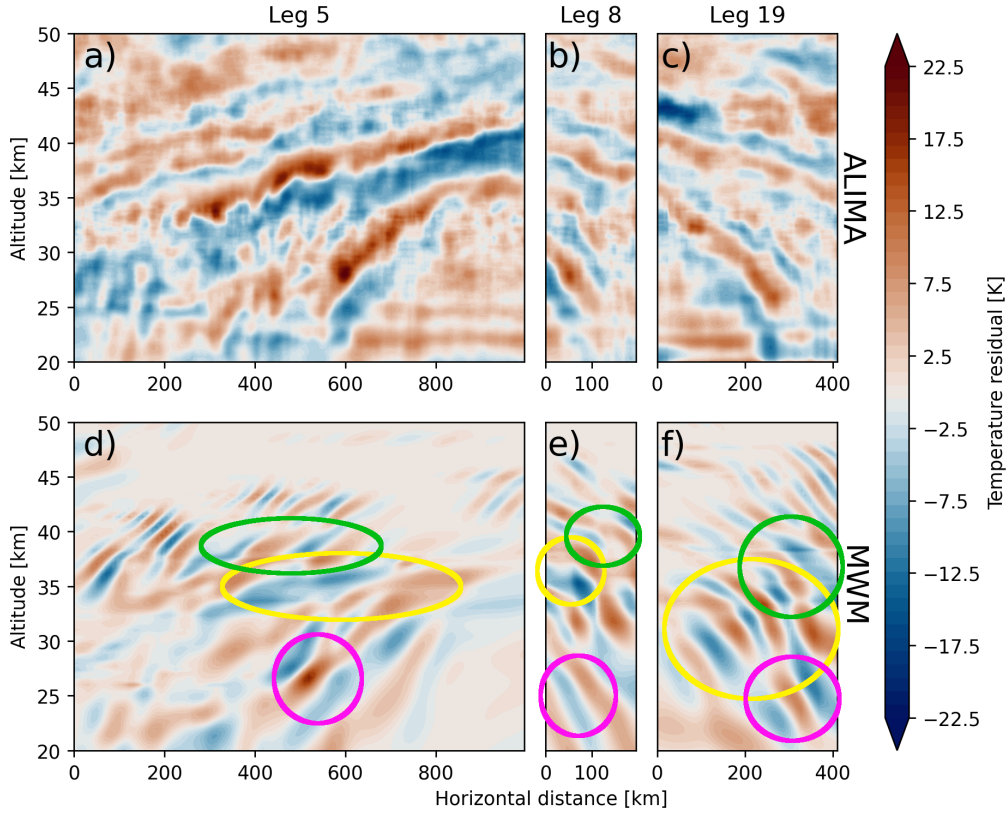
Figure 4.3: Temperature perturbations as measured by ALIMA during flight 12 of the South-TRAC campaign for selected flight legs (panels a–c) and the predictions for the same region from the MWM (panels d–f). The horizontal axis gives the distance from the start point of the flight leg. Information on the corresponding flight paths is given in Fig. 4.4. GW features of special interest for the source allocation are highlighted in the MWM predictions by green, yellow, and magenta ellipses, respectively.

the highest-amplitude GW spreading across the Pacific Ocean is not as pronounced in the predictions. Small-scale erratic patterns are seen in the observational data and the MWM prediction and can therefore be attributed to the interference of multiple mountain waves of different origins.

The MWM models the MWs excited by each mountain ridge individually; hence the source locations of the different regions of the perturbation field can be investigated in the next step. Exemplarily, three MWs are chosen as encircled in Fig. 4.3 in green, yellow, and magenta, respectively. Although these features originate in different parts of the Southern Andes and from separate mountain ranges, they propagate into the same region, where they are observed in all three considered flight legs.
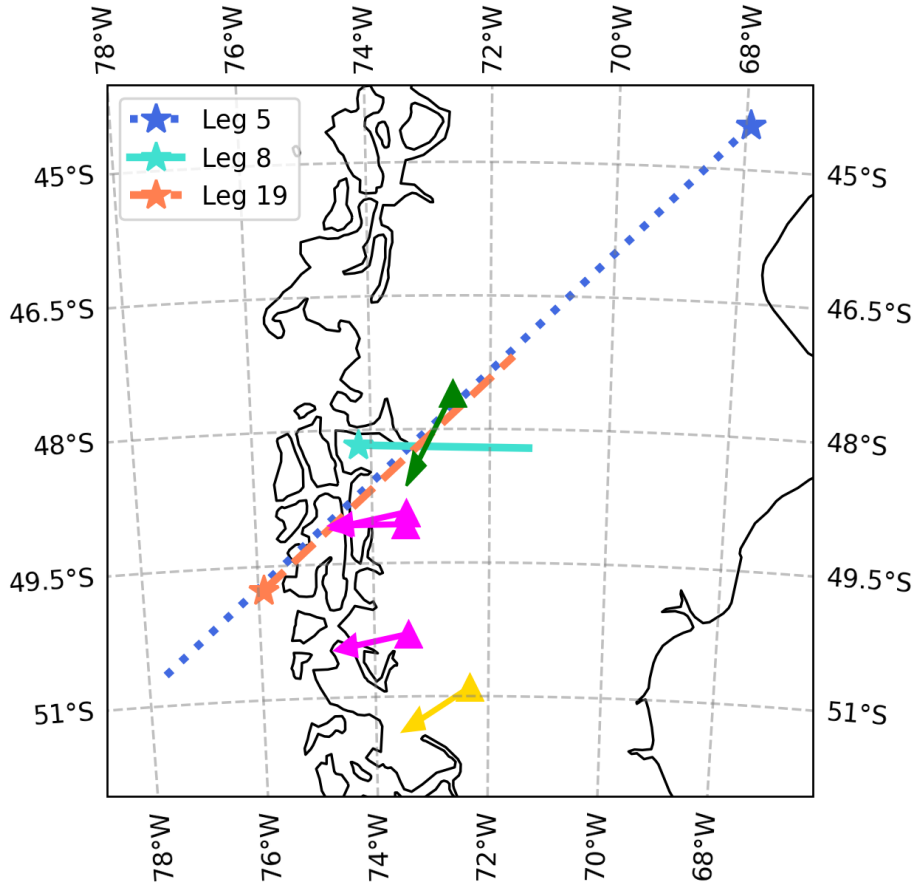
Figure 4.4: Flight paths for the three legs considered in this section. A star marks the start point of the flight track, i.e., the point corresponding to zero distance in Fig. 4.3. The estimated source locations and the initial orientation of the wave vector are shown by a triangle and an arrow, respectively. The color of the triangle matches the color of the highlighting of the corresponding MW perturbation in Fig. 4.3.

Within the MWM, different wave packets can be distinguished by their ray traces and origin. In particular, the MWs excited by specific mountain ridges can be reconstructed separately, identifying the origin and extent of individual wave patterns. Figure 4.4 shows the source identification for the highlighted features in the flight legs. The source mountain ridges are drawn in the same color as the ellipse encircling the corresponding MW feature. The attached arrow represents the orientation of the mountain ridge and, therefore, the initial orientation of the wave vector.

The yellow and magenta highlighted temperature perturbation originate from the main Andes mountain ridge but from different locations. Evidently, the GW excited by the yellow

mountain ridge needs to propagate further north and thus is only visible at higher altitudes in the shown temperature curtains. On the other hand, all three mountain ridges shown in magenta contribute to the low-altitude, high vertical wavenumber perturbation. In addition, the initial scales of both GWs are very different. The magenta mountain ridges are of short scales of about 150 km, while the yellow mountain ridge has a scale of about 600 km. Therefore the "gooseneck" structure seen in the most dominant waves in the ALIMA curtains results from the superposition of MWs of different scales and origins.

The MWM predicts the temperature residuals highlighted in green, which are of shorter horizontal and longer vertical scales, to originate from a secondary ridge directly beneath the flight legs. Due to the short horizontal scales, this GW is stronger localized above the source ridge than, for example, the yellow-highlighted MW (see also Sec. 4.2.2). The elevation of the corresponding mountain ridge is comparatively low.

The comparison of MWM predictions to observations shown in this section gives an example of how the MWM can be used to disentangle complex structures of GW perturbations as seen in the ALIMA observations to the individual wave packets and ultimately to the originating source mountain ridges. Thereby the MWM is augmenting the model data in a constructive way. Note, however, that the comparison to the MWM is not perfect (as can be seen in the prediction vs. measurements in Fig. 4.3) and is only possible in regions dominated by orographic GW activity. Therefore, the case study of the Southern Andes considered here is an ideal test case.

4.3   Estimation of GM momentum flux

Similar to the residual temperature reconstruction in Sec. 4.2, the ray tracing data can be used for reconstructing spatial GWMF distributions. These GWMF distributions can be compared to, e.g., global satellite observation data and used for further studies of the momentum transport by MWs. The reconstruction algorithm for GWMF is closely related to the reconstruction of temperature perturbations. Analogous assumptions are made, i.e., assuming that each GW packet has a limited spatial extent depending on the horizontal wavelength

and the source ridge length. In addition, the area covered by each wave packet within a grid cell needs to be accounted for.

This section presents the basics of the reconstruction algorithm for GWMF distributions. Afterward, the performance of the MWM in predicting horizontal GWMF pattern is validated by comparison to HIRDLS satellite data for January and July 2006. In addition, the observational data is analyzed in detail using the ray tracing data generated by the MWM and considering critical level filtering due to the wind profiles. The presented analysis follows closely Rhode et al. (2023).

4.3.1 Methodology

The reconstruction of GWMF distributions from ray tracing data follows mostly the same algorithm as the reconstruction of residual temperatures (see Sec. 4.2). The GWMF, however, is proportional to the temperature amplitude squared (Ern et al., 2004), and therefore, should decrease much faster with increasing distance to the center of the wave packet. Secondly, the GWMF is a consequence of the oscillating wave pattern of the GW and is independent of the phase. Thus, it depends only on the GW amplitude, and the oscillating term in the reconstruction can be dropped.

The maximum GWMF $F_{\max}$ is assumed to be at the center of the wave packet given by the the ray tracer. Assuming an enveloping Gaussian shape, the spatial distribution of a single GW packet can be expressed as

$$F = F_{\max} \frac{1}{\sqrt{1 + \left(\frac{2d_{\mathrm{perp}}}{l} \right)^{12}}} \exp \left(-2 \left(\frac{2d_{\mathrm{parallel}}}{\lambda_{\mathrm{hor}}} \right)^2 - 2 \left(\frac{2d_z}{\lambda_z} \right)^2 \right), \qquad (4.3)$$

where d_{parallel} and d_{perp} are the horizontal distance from the ray path parallel and perpendicular to the horizontal wave vector, and d_z is the vertical distance to the center of the wave packet.

In general, the grid boxes of the reconstruction are much larger than the average wave packet, which leads to possible under- and overestimation of the GWMF contribution to that

wave packet if the GWMF is sampled only at a single point within the grid cell. If this sampling point is located right at the center of the wave packet, the total GWMF of the grid cell is overestimated, and the opposite is true when the sampling point is far from the center of the wave packet. In principle, the total contribution of a wave packet within the grid cell has to be spatially integrated. This integration, however, is rather involved due to the almost random nature of the partial grid cell coverage, orientations, and scales of the GWs. The exact integral can be approximated by supersampling the original reconstruction grid, which is essentially a finite-elements integration of the GWMF.

Figure 4.5 shows the estimated error of the supersampling of the GWMF for GWs of different horizontal scales within a grid cell of 150 km horizontal extent corresponding to the grid size used throughout this thesis. The graphs show the average error introduced by supersampling with the given, color-coded number of points (per dimension) in comparison to the exact calculation of the integral in dependence on the horizontal scale of the wave packet. The average is calculated over all possible orientations and locations of the wave packet within the grid cell.

If the GWMF is sampled only at the central point of the grid cell, the introduced error, i.e., over- and underestimation of the total GWMF, is too large to give trustworthy results for GWs of horizontal scales of 100 km and below. However, if the reconstruction uses a supersampling of 3 or 5 points per dimension, the error for waves of about 80 km scale drops below 4% and 2%, respectively. In this thesis, the horizontal scales of the GWs are mostly above 100 km. Therefore, in the following considerations, a supersampling using 3 points is used, which gives sufficiently reliable estimations of the GWMF.

Most commonly, the density of GWMF is considered, instead of the total amount in a given grid cell, which ensures inter-comparability between differently gridded data sets. Therefore, the presented reconstruction, which gives the total GWMF in the grid cells, needs to be scaled by the horizontal grid cell area as follows:

$$F_{\text{tot}} = \frac{\sum_i F_i}{A_{\text{grid}}}, \tag{4.4}$$
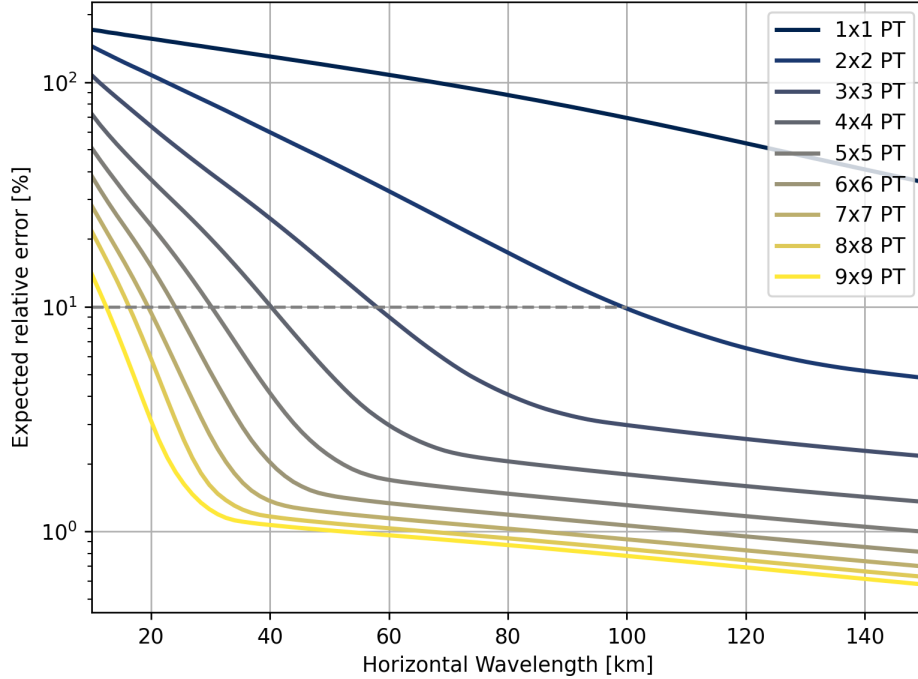
Figure 4.5: Error estimation of the GWMF sampling for wave packets randomly distributed and oriented within a grid cell of 150 km width compared to the exact integral. The color of the line represents the number of supersampled points, i.e., 1x1 PT corresponds to simply sampling the center of the grid cell. The error drops significantly by supersampling with 3x3 points for the here-considered scales of about 100 km and beyond.

where the individual contributions of the wave packets i are summed up and divided by the grid cell area $A_{\text{grid}} = d_x d_y$.

Finally, this reconstruction allows for generating horizontal GWMF distributions from ray tracing data at arbitrary altitudes and times. In the following sections, GWMF distributions predicted by the MWM are used to validate the MWM against satellite data and investigate MW features within these for January and July 2006.

4.3.2 Global GWMF distributions from HIRDLS

Another validation of the MWM can be made by comparing the predicted GWMF distributions to satellite data. Further, the MWM allows an in-depth analysis of MW-related features in the observations by supplementing the satellite data with explicit MW modeling.

Satellite data sets

The satellite data considered in this case study are measured by the HIgh Resolution Dynamics Limb Sounder (HIRDLS, Gille et al. (2003)) instrument. The horizontal resolution of these measurements is about 80–100 km along-track and about 1 km in the vertical. The present data set is specially prepared for the UTLS region, spanning altitudes from 14 km to 25 km. As discussed in Strube et al. (2020), below 20 km altitude, zonal wavenumbers of 10 and longer need to be taken into account in order to describe the large-scale atmospheric background. These wavenumbers, however, cannot be self-consistently estimated from a single-track low Earth orbit satellite (Salby and Callaghan, 1997). To isolate the contributions of small-scale GWs, lowpass filtered ERA5 reanalysis data with an altitude-dependent zonal wavenumber cutoff has been subtracted from the retrieved HIRDLS temperature measurements. The cutoff has been set to zonal wavenumber 20 (about 2000 km at the equator) below 10 km and zonal wavenumber 6 (about 6700 km at the equator) above 20 km. In between, the cutoff decreases linearly with altitude from 20 to 6. In addition, the HIRDLS data set has been high-pass filtered in terms of vertical wavenumbers using a 5th-order Butterworth filter with a cutoff in vertical wavelength of 12 km, similar to Ehard et al. (2015).

The GWMF is calculated from the resulting vertical profiles of temperature residuals as described in Ern et al. (2018) with slight modifications to suit the lower altitudes considered here. In order to analyze the lower stratosphere, i.e., about 20 km and below, and simultaneously avoid the influence of the tropopause, the vertical window of the applied maximum entropy method and harmonic analysis (MEM/HA) method (Preusse et al., 2002) was reduced from 10 km, which is typically used in the stratosphere (e.g. Ern et al., 2004), to 5 km. This reduced window size is preferable since the average vertical wavelengths in the lower stratosphere are much lower than in the mid stratosphere and mesosphere (e.g. Chane-Ming et al., 2000; Yan et al., 2010; Ern et al., 2018).

For this particular study, the GWMF is binned to rectangular overlapping bins of $15°$ in longitude and $5°$ in latitude sampled every $5°$ in longitude and $2.5°$ in latitude from the original profiles given along the satellite orbits. The vertical resolution is unchanged from the satellite data at 1 km. Note that due to the vertical window of 5 km used in the MEM/HA method,

the given data levels are representative for $\pm\,2.5\,\text{km}$ around the corresponding altitude.

January 2006

Figure 4.6 shows monthly mean total GWMF distributions for January 2006 as retrieved from HIRDLS (left column) and predicted by the MWM (right column) at altitudes of $16\,\text{km}$, $20\,\text{km}$, and $25\,\text{km}$. The most prominent pattern in the HIRDLS observations is located above the Himalaya and Altai Mountains (Mongolia), where two local maxima can be seen. The maximum above the Himalaya dominates at $16\,\text{km}$, but weakens stronger than the one above the Altai mountains with increasing altitude. Thereby only the pattern above Mongolia remains at $25\,\text{km}$ altitude. This double pattern above central Asia is consistent throughout the considered altitude levels. This feature is also structurally predicted by the MWM, although with lower amplitudes. Both regions show comparable local maxima at lower altitudes with the reduced GW activity above the Himalaya at higher altitudes analogously to the observations.

To understand this northward shifting GW activity, the properties and parameters of GWs in the different regions can be investigated within the MWM. Fig. 4.7 shows the histograms of horizontal and vertical wavelengths at $16\,\text{km}$ and $25\,\text{km}$ altitude for both regions as calculated from the MWM. The horizontal wavelengths are almost the same at both altitude levels in both regions. Conversely, the vertical wavelengths differ strongly between altitudes but also between both regions. The MWs above the Himalaya, i.e., the southern region, exhibit longer vertical wavelengths, which should be strongly suppressed by the observational filter, which has a cutoff at $\lambda_z = 12\,\text{km}$, at $16\,\text{km}$ altitude. Propagating upwards, the MWs refract strongly towards short vertical wavelength due to a negative vertical gradient of zonal wind (see Fig. 4.9). Therefore, there are at least two possible reasons for the diminished GW activity in the satellite observations at higher altitude levels: For one, the vertical resolution of HIRDLS is about $1\,\text{km}$ (Wright et al., 2009), which, in principle, allows for the detection of GWs with vertical wavelengths as low as 2-4 km. Multiple waves refract to wavelengths below this threshold and therefore are no longer seen by the instrument. Another reason might be high amplitude GWs, which are typical in this region of high elevation orography, that
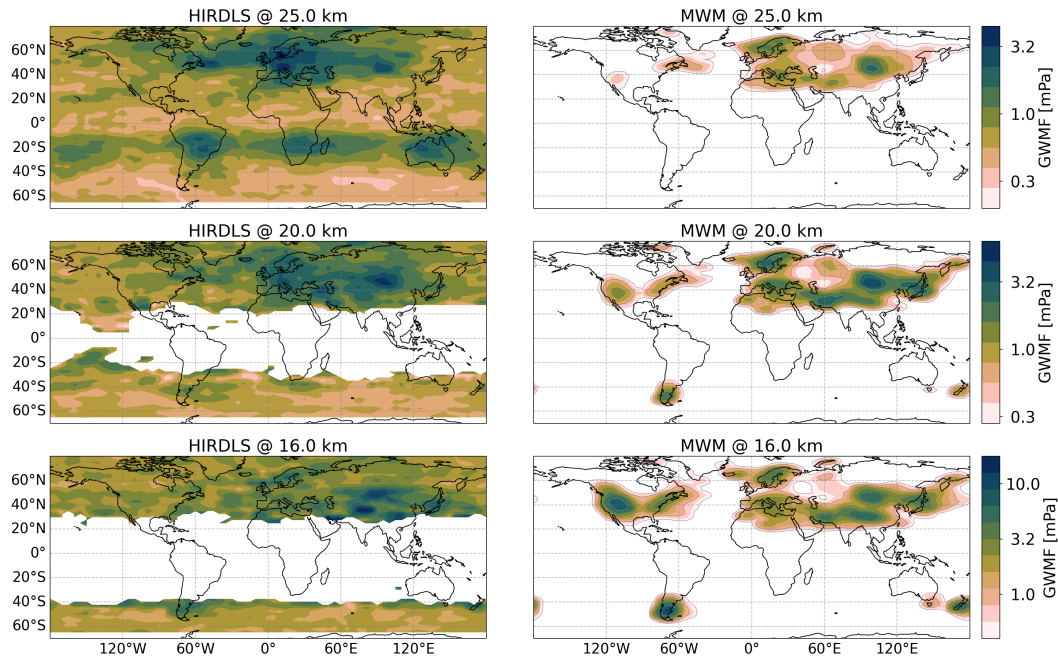
Figure 4.6: Global distribution of GWMF in the monthly mean for January 2006. The left column shows data from HIRDLS satellite observations (see Sec. 4.3.2), and the right column shows GWMF distributions predicted by the MWM. The different rows present data for 16 km, 20 km, and 25 km altitude from bottom to top, respectively. Note the differing logarithmic color scales.

could completely break instead of propagating further with an amplitude reduced below the saturation limit in a strong wind vertical shear (Kaifler et al., 2015). Such a complete break-down of GWs is currently not captured by the GROGRAT simulations. The MWM could be a suitable tool to test this hypothesis in other, more specific case studies by implementing different breaking schemes.

The MWM simulation shows very high GW activity above the Rocky Mountains. Al-though the amplitudes are overestimated in direct comparison to the satellite observations, a similar feature can be seen in both data sets. This GW signature diminishes with increasing altitude until it almost vanishes at 25 km. Within this region, there is also a minor southward shift of GWMF towards California visible, which is also hinted at by the satellite data. This feature sits, however, right at the edge of the observation and is, therefore, not fully charac-terizable. Similar arguments for the Himalaya region can explain the reduction of amplitudes here: a high negative vertical wind shear above the Rocky Mountains reduces the maximum

allowed amplitudes of GWs strongly. Compared to the Himalaya region, the MWs above the Rocky Mountains are launched with much higher amplitudes (about a factor of two, not shown), making them more likely to encounter saturation or complete breakdown along their path (there is plenty of evidence of high-amplitude MWs and their breaking in this region, e.g., Guarino et al. (2018)). The latter process might be a reason for the overestimation at 16 km altitude since the negative wind shear starts already at roughly 10 km, where waves could already break down. Therefore, the strong signature seen in the predictions could indicate a process that is not yet taken into account within the MWM.

Further noticeable patterns predicted by the MWM are the two local maxima in the Southern Hemisphere above New Zealand and the southern Andes, which are matched partially by the observations. The amplitude of these maxima strongly decreases at higher altitudes until they ultimately vanish at 25 km as expected, since MWs are critical-level filtered by the wind reversal at around 20 km altitude in the summer hemisphere. The MWM-predicted GWMF is higher than the satellite observations, which could be related to the GW-breaking process mentioned above. The MWM prediction shows far eastward propagation mainly above New Zealand, while the satellite data shows signs of far eastward propagation above both sources. However, the persistence of this pattern in the satellite observations at 25 km altitude is inconsistent with them being MWs. Instead, these are most likely GWs of other origin than orography.

The MWM predicts multiple GW sources in the North Atlantic region: Newfoundland, southern Greenland, Iceland, and Scandinavia. Especially above Iceland, far eastward propagation is seen, where the pattern of GWMF merges with the one above Scandinavia. In addition, the MWM predicts eastward propagation from Newfoundland towards southern Greenland at 25 km altitude. However, in general, the MWM-predicted GWMF is suppressed at this altitude. The HIRDLS observations show similar, although more complex patterns of GWMF in this region. The aforementioned MW sources are visible but merge into a band of high GWMF at 20 km and above. This band follows the path of the polar vortex and might therefore be related to local GW sources such as jet imbalances and fronts (e.g. Geldenhuys et al., 2021). The occurrence of sources other than orography in the observations
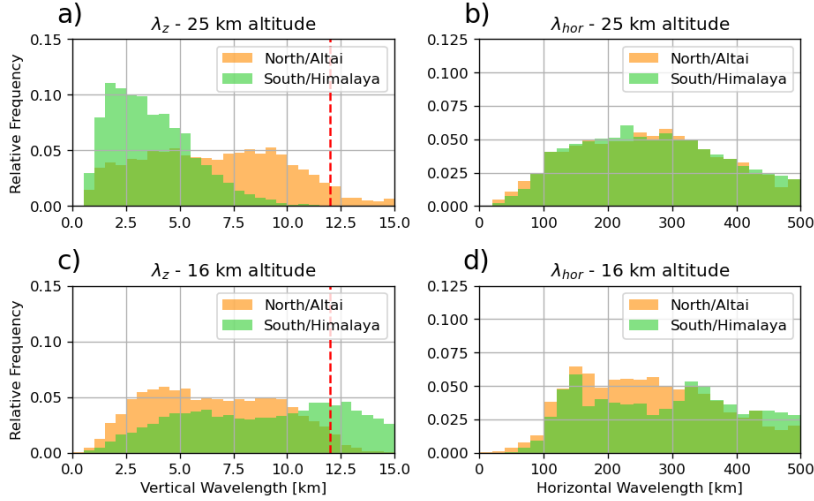
Figure 4.7: Distributions of vertical (left column) and horizontal (right column) wavelengths as calculated by the MWM at altitudes of 16 km (bottom row) and 25 km (top row). The northern region corresponds to the Altai Mountains at 42.5°-55.0°N 75-105°E, the southern region to the Himalaya at 30.0°-42.5°N 65°-95°E. The vertical red line on the left panels marks the cutoff for the vertical wavelength of $\lambda_z = 12$ km used in the highpass filtering of the HIRDLS data.

is strengthened by the (slight) increase of GWMF between 20 km and 25 km altitude.

To further investigate the reasons for the differences between the MWM and the satellite observations, blocking diagrams similar to the ones introduced in Taylor et al. (1993) and vertical profiles of the horizontal wind can be used. The considered regions of interest are shown in Fig. 4.8. In particular, differences in propagation conditions for non-orographic GWs above the Himalaya compared to Mongolia, above the Rocky Mountains, and above southern Africa, where a strong GWMF pattern arises in the HIRDLS data at 25 km altitude (see Fig. 4.6) are investigated. For the illustration of the general wind conditions, Fig. 4.8 shows the monthly mean zonal wind at 20 km altitude.

In the blocking diagrams shown in Fig. 4.9a–d, the criterion of waves encountering a critical level whenever the intrinsic frequency of a GW goes to zero, $\omega_{\mathrm{intr}} \to 0$, is used, where

$$\omega_{\mathrm{intr}} = \omega_{\mathrm{gb}} - \boldsymbol{k_{\mathrm{hor}}} \cdot \boldsymbol{U}, \tag{4.5}$$

$$\Leftrightarrow \quad \omega_{\mathrm{intr}} = \omega_{\mathrm{gb}} \left(1 - \frac{U_{\mathrm{par}}}{v_{\mathrm{ph}}} \right). \tag{4.6}$$
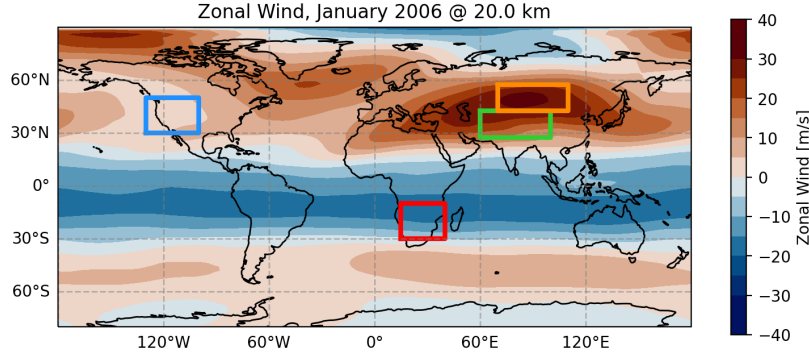
Figure 4.8: Regions of interest for critical layer filtering considered in this study shown on top of the monthly mean zonal wind at 20 km altitude: Himalaya (green), Mongolian Plateau (orange), Rocky Mountains (blue) and southern Africa (red). The same colors as in Fig. 4.7 have been used for the Mongolia and Himalaya regions.

Here, $\boldsymbol{k_{\mathrm{hor}}}$ and $\boldsymbol{U}$ are the horizontal wave- and wind vector, U_{par} is the wind speed projected onto the horizontal wave vector, and $v_{\mathrm{ph}} = \frac{\omega_{\mathrm{intr}}}{k_{\mathrm{hor}}}$ the horizontal phase speed. This consideration neglects the Coriolis parameter, which would restrict the intrinsic frequency even further ($|f| < \omega_{\mathrm{intr}}$) and hence leads to a stricter limit of phase speeds.

The curve of $\omega_{\mathrm{intr}} = 0$ is a circle in phase speed diagrams with the center at $\left(\frac{U}{2}, \frac{V}{2}\right)$ and radius $R = \frac{1}{2}\sqrt{U^2 + V^2}$ for zonal and meridional background wind speeds U and V and covers the restricted, i.e., blocked or filtered, part of the phase speed spectrum. These curves generated for the wind speeds from the surface up to 25 km altitude can be superposed on a phase speed diagram to estimate how widespread of all altitudes the critical levels for GWs with the source close to the ground are. The resulting blocking diagrams are shown in Fig. 4.9a–d, where the color shading gives the percentage of vertical profiles that exhibit critical levels for GWs of the corresponding (ground-based) phase speed. In other words, the color shading gives an estimate of the probability for GWs with a given phase speed to be filtered by a critical level below 25 km. Note, however, that near the launch locations of MWs and other GWs with approximately zero phase speed, these diagrams only hint at a critical level, where $\omega_{\mathrm{gb}} \approx 0$ and, thus, $v_{\mathrm{ph}} \approx 0$. Under these conditions, MWs encounter critical levels wherever the horizontal wind projected onto the horizontal wave vector becomes zero. As an additional metric, the monthly mean vertical profiles of horizontal wind for the four regions are shown in Fig. 4.9e and f, where reversing winds are easily seen.

Comparing the critical layer filtering patterns for the Himalaya and Mongolian plateau in monthly mean wind profiles in Fig. 4.9a and c, a wider range of phase speeds is restricted in the southern region, i.e., above the Himalaya. This stricter filtering potentially leads to a stronger suppression of non-orographic GWs, which might be part of why the GWMF in HIRDLS declines so fast with altitude in Fig. 4.6. The vertical profiles of monthly mean winds shown in Fig. 4.9e display no wind reversal in either of the regions and, thus, MWs should, in general, propagate similarly well in both regions. However, the zonal wind of the southern region exhibits a sharp vertical gradient. The wind speed peaks at around 12-13 km with a pronounced maximum of about $45\,\mathrm{m\,s^{-1}}$, which is roughly 5 km below the level of maximum wind speed of the northern region, the Mongolian Plateau. This high wind speed allows high amplitudes of the MWs, which afterward encounter a strong negative wind shear leading to refraction towards small vertical wavelengths and vigorous wave breaking due to exceeding the saturation limit. The strong wind shear and high GW amplitude could lead to severe turbulence upon wave breaking, and hence Kaifler et al. (2015) suggests that high-amplitude GWs might break completely upon saturation instead of propagating further with reduced amplitude. The lack of this effect in the GROGRAT simulations could be one reason for the overly enhanced GW activity above the Himalaya predicted by the MWM (Fig. 4.6). Above Mongolia, the propagation conditions are more favorable for MWs due to a more consistently strong wind that is slowing down only above 25 km altitude. Therefore the satellite observations and the model predictions both do not see such a severe reduction in GW activity as above the Himalaya region.

Since the here-considered blocking diagrams are not directly applicable to MWs close to their sources, alternative blocking diagrams for MWs with $\omega_{\mathrm{gb}} \approx 0$ are shown in App. A.4. Figure 7.1a and c show that due to the wind profile, the (horizontal) phase space in the Himalaya region is less restricted and, therefore, might exhibit more (diverse) MW activity in the stratosphere. The Mongolian Plateau, on the other hand, shows a much more restricted initial phase space. This finding underlines that the northward shift of the local GWMF maximum in the HIRDLS observations compared to the MWM could stem partly from non-orographic GWs measured above the northern part as well as MWs refracting to vertical

wavelengths that the observation data does not pick up.

The Rocky Mountains are the next region to investigate. The blocking diagram for this region is shown in Fig. 4.9b, and corresponding wind profiles are given in Fig. 4.9f (blue lines). The blocking diagram exhibits high values at and around the origin, indicating low wind speeds at various heights. The dumbbell-like shape, i.e., circular structures on either side of the origin, is a direct consequence of a wind reversal in the considered altitude range. The wind reversal of the horizontal winds is seen in the wind profiles at about 22 km altitude. The wind reversal prevents any MWs from propagating further upward. A wind reversal in the winter hemisphere is untypical and, in this case, is most certainly caused by the displaced location of the polar jet due to the SSW that happened during January 2006 (e.g. Xu et al., 2018). In the monthly mean winds in Fig. 4.8, the polar jet is not located above the Rocky Mountains but much further north (at about 75°N), which strongly affects the propagation criteria for MWs. The shape of the wind profile above the Rocky Mountains is similar to the one above the Himalaya region with a peak wind speed of about $25\,\mathrm{ms}^{-1}$ at $\sim$11 km altitude followed by a strong negative wind shear. In addition, the low-level wind speeds are around $6\,\mathrm{ms}^{-1}$, which is four times as strong as in the Himalaya region. Therefore, the MWs of this region have the potential to launch with much higher initial amplitudes, which makes them more likely to reach saturation and complete breaking due to high amplitudes as described by Kaifler et al. (2015). Again, since this is not modeled in the MWM, it may predict much stronger GWMF values than there actually are in this region.

Lastly, we want to briefly consider southern Africa to exclude MWs as a source for the pattern seen in HIRDLS at 25 km. The corresponding blocking and wind profiles are shown in Fig. 4.9d and f (red lines). The blocking diagram has a pronounced dumbbell shape caused by a wind reversal seen in the wind profile at about 4 km altitude. The wind reversal makes the propagation of MWs into the stratosphere impossible. Conversely, only small parts of the phase speed spectrum are blocked. These are ideal conditions for GWs of sources that generate a wide range of phase speeds like convection (e.g. Salby and Garcia, 1987; Alexander and Dunkerton, 1999; Preusse et al., 2001; Choi and Chun, 2011; Trinh et al., 2016). Therefore we can conclude that the observed patterns appear not due to orography but other sources

(most likely convection).

To summarize, the predictions of the MWM and the calculated wave parameters can explain the shift of focus of GW activity from the Himalaya to the Altai Mountains and therefore solve the question of why there is not as much GW activity as would be expected from the underlying orography itself. The MWM shows that parts of the GW spectrum refract to very short vertical wavelengths, which makes them hard to detect by the satellite. The refraction to smaller vertical wavelengths can be distinguished from GW breaking within GROGRAT. In the considered case, the modeled MWs do not reach the saturation amplitude, although the vertical wavelengths shorten significantly. The feature above the Himalaya is more pronounced without the instrument-specific observational filter substantiating the argument. In addition, the MWM is showing a strong GW signature above the Rocky Mountains, as would be expected from the orography. Since this is not present to such a degree in the satellite data, it might hint at a GW process that is not yet captured in the MWM, e.g., total breakdown of GWs reaching a saturation level (Kaifler et al., 2015). In total, the MWM has proven to be a valuable tool for investigating the orographic part of global GWMF observations for the case of January 2006.

July 2006

In this section, MWM-predicted GWMF distributions for July 2006 and the corresponding MW parameters, i.e., the wavenumbers and amplitudes, are considered to explain observed GWMF patterns found in HIRDLS satellite observations. Fig. 4.10 shows horizontal, global distributions of GWMF as retrieved from HIRDLS (left column) and predicted from the MWM after applying the observational filter (right column) at altitudes of 16, 20, and 25 km. The dominant feature in both data sets is the maximum above the southern Andes. At 16 km HIRDLS shows a distinct global maximum at around ∼52°S accompanied by a weaker separate local maximum directly north at around ∼42°S. At higher altitudes, the southern maximum vanishes while the northern one persists, which leads to an overall northward shift of the GWMF and, hence, of the global maximum.

The HIRDLS data set shows a far eastward spread around these maxima up to about
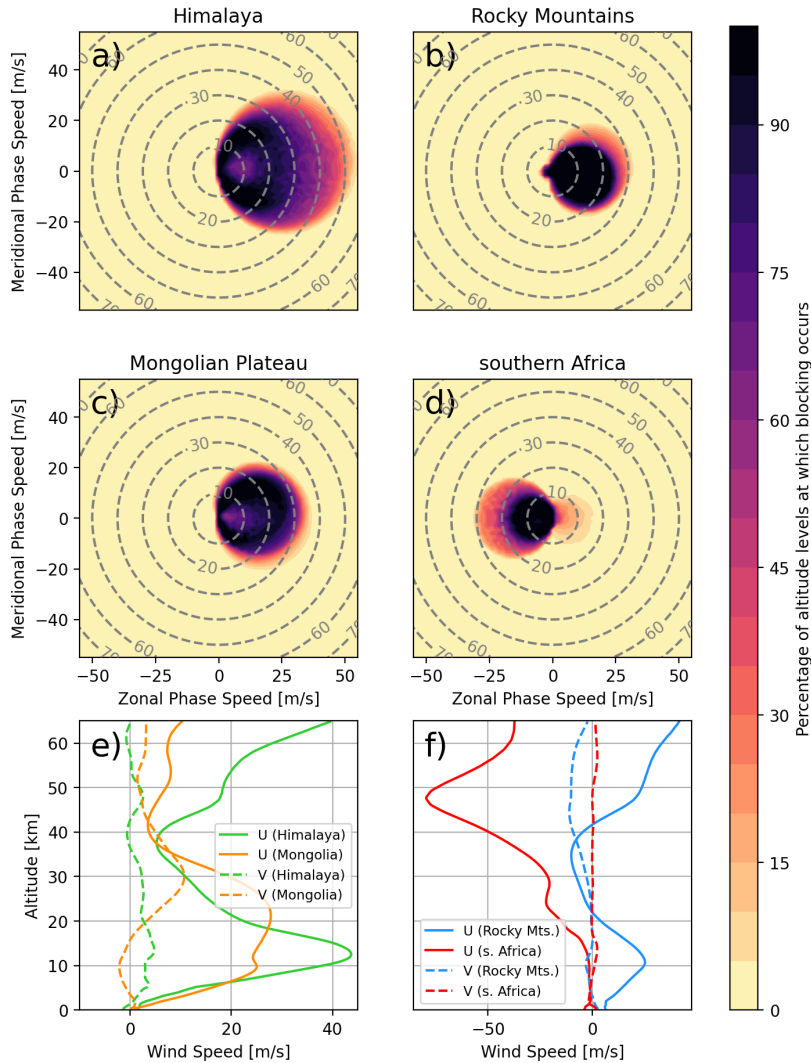
Figure 4.9: Blocking diagrams as introduced in Taylor et al. (1993) for the four regions shown in Fig. 4.8 and the time period of January 2006: Himalaya, Brazil, Mongolian plateau and southern Africa in panel a, b, c, and d, respectively. The color shading gives the fraction of altitude levels between the surface and 25 km altitude exhibiting a critical level for the corresponding position in the GW phase speed spectrum. Alternatively, these diagrams can be interpreted as the probability estimation of a GW of a given (ground-based) phase speed passing beyond 25 km altitude without being filtered by a critical level. The monthly and spatially averaged wind profiles at the individual levels have been used in the calculation of the critical levels in the corresponding region. Panels e and f show the monthly mean vertical profiles of zonal (solid) and meridional (dashed) wind speed for the Himalaya and Mongolian Plateau regions and Brazil and southern Africa region, respectively (colors correspond to the boxed regions in Fig. 4.8).

30°W over the Atlantic. The observed spread can be explained by eastward propagating MWs by comparison to the MWM prediction, which shows a similar pattern with a higher

amplitude maximum above the southern Andes. In a textbook case of oblique propagation from a single source region, the spread should increase with altitude. The increased spreading is seen in the MWM predictions, where MWs reach as far as 30°W at 25 km altitude. The satellite observations, however, show a decrease at 20 km altitude followed by an increase in the spread distance at 25 km altitude. Although the maximum of the MWM prediction is not as precisely localized as in the observations, it predicts the same northward shift at higher altitudes.

As seen in Sec. 4.3.2, the MWM allows an in-depth look at possible causes of the northward shift seen in the observations by investigating individual GW parameters in these regions. Fig. 4.11 shows the histograms of vertical and horizontal wavelengths of all modeled MWs between 37°-47°S and 47°-57°S, respectively, and longitudes between 40°-90°W at 16 km and 25 km altitude. The histograms indicate a drastic increase in vertical wavelengths in the southern region, while the ones in the northern region remain almost unchanged. The distributions of horizontal wavelengths stay mostly unchanged with increasing altitude for both regions. The MWs constituting the southern maximum refract towards longer vertical wavelengths than the cutoff wavelength of 12 km used in highpass filtering of the HIRDLS data set and thus become invisible at higher altitudes. This finding is confirmed by the unfiltered observation data, i.e., without applying the cutoff at $\lambda_z = 12$ km, which shows a broad maximum at all altitudes (not shown). In addition, the MWM shows more GW activity in the south without the observational filter, which could mean that HIRDLS picks up more of the horizontal spectrum than assumed in the observational filter described in Trinh et al. (2015) (see Fig. 5.1). This visibility filtering at higher latitudes is also one likely reason for the reduced GWMF predictions of the MWM around the Antarctic Peninsula.

Another major feature predicted by the MWM is the high GW activity around the Antarctic Peninsula and eastward trailing GWMF, especially at higher altitudes. This prediction agrees with the satellite observations concerning the extent of the horizontal propagation. The HIRDLS data, however, shows another peculiar pattern: GWMF is increasing again above 20 km altitude at the highest latitudes. Since the data set is limited to about 63°S, it is unclear where this enhanced GWMF originates. For one, the cause could be orographic

GWs propagating from further south, which, however, is not predicted by the MWM. Even without the observational filter, there is some northward propagation above the Antarctic Peninsula but far too little to compensate for the reduction in orographic GWMF with altitude due to saturation and wave breaking. Another explanation might be related to MWs due to katabatic flow (Watanabe et al., 2006) or non-orographic processes like imbalances of the polar jet, frontal systems, or even secondary wave generation. At least partially, this lack of GWMF might also be related to the filtering at high latitudes by the observational filter. Note that GWs excited by katabatic flow, although categorized as MWs, are not considered by the MWM since they are excited by drops in elevation, which are not detected by the presented ridge-finding algorithm. The extent of the eastward propagation seen at 25 km altitude in both data sets is in agreement with previous studies by, e.g., Sato et al. (2012); Perrett et al. (2021).

Further enhanced GW activity is predicted by the MWM above the Southern Alps and the Great Dividing Range/Tasmania, which has been shown to be a relevant MW source by Eckermann and Wu (2012). The MWs from Australia and Tasmania show a relatively localized pattern with increasing altitude, while the MWs originating from the Southern Alps show far south-eastward propagation, especially at higher altitudes. In the satellite observations, these features are hard to separate from the background and, therefore, can not be validated entirely. However, the satellite observation shows some visibly enhanced GWMF around the Southern Alps in New Zealand, which stretches to the southeast and merges with the background at around 170°W. Looking into unfiltered MWM data reveals far north-eastward propagation of MWs originating from eastern Antarctica, which could also partly contribute to enhanced GWMF in this region.

MW activity of similar strength to New Zealand is predicted above South Africa and propagating towards the southeast. Although this region is usually not regarded as a hot spot for MWs, the pattern of enhanced GWMF in this region is fairly consistent throughout the southern hemispheric winter, as will be shown in Sec. 5.1. In the satellite data, this feature is obscured by the belt of high GWMF in the Southern Ocean but could be interpreted as the bend in this belt towards the southeast of Africa.
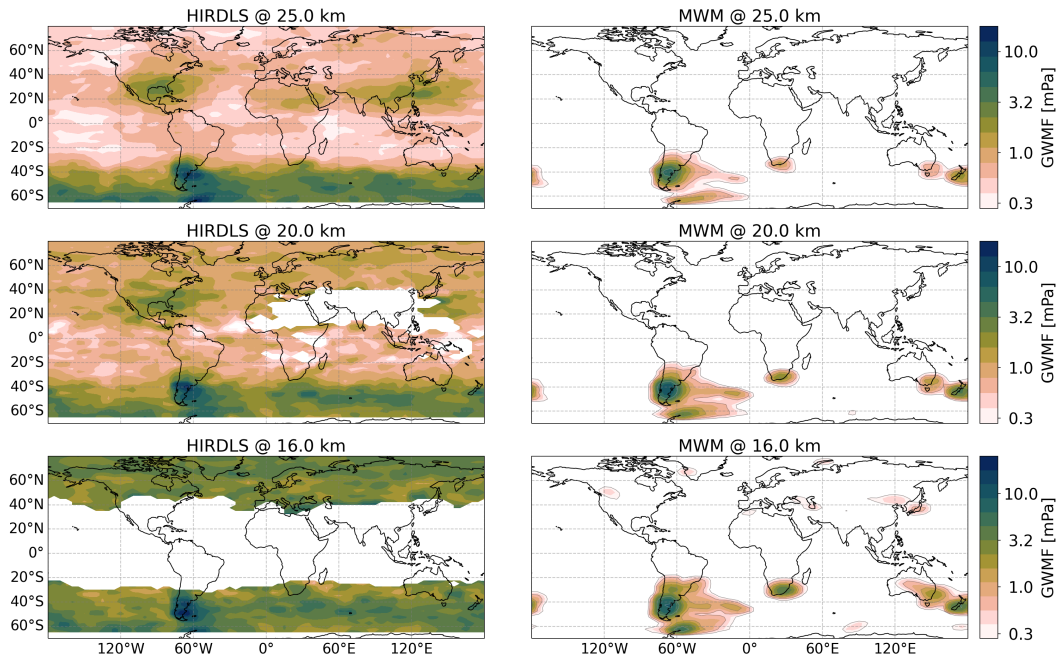
Figure 4.10: Same as Fig. 4.6 but for July 2006. Note the logarithmic color scales.
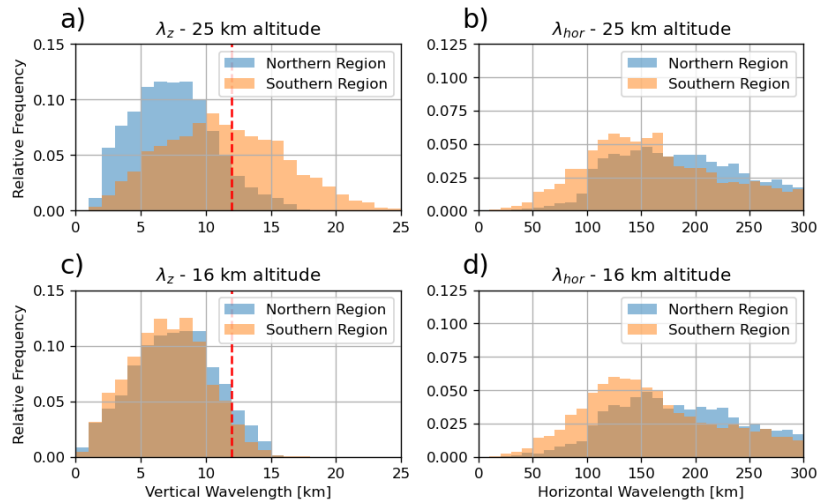
Figure 4.11: Distribution of vertical (left column) and horizontal (right column) wavelengths as predicted by the MWM at altitudes of 16 km (bottom row) and 25 km (top row). The northern region corresponds to 37°–47°S and the southern region to 47°–57°S, both between 40°–90°W. The vertical red line in panels a and c marks the cutoff wavelength of $\lambda_z = 12$ km for the present HIRDLS data.

Chapter summary

This chapter describes the capabilities of the mountain wave model (MWM) for MW temperature perturbations and GWMF distributions, and the performed validating comparisons to

model data and observations in multiple case studies. Under the assumption of single wave packets with finite extent, the MW-induced temperature perturbations can be reconstructed from the ray-tracing data generated by the MWM. The ray tracer provides all necessary information, i.e., location, phase, amplitude, and wave vector, to estimate the individual contribution of each wave packet to the overall perturbation field. Superposing the individual contributions of the MWs from each mountain ridge constructs the complete temperature residuals. The temperature reconstruction is validated against a simple Fourier transformation MW model. The comparison of MWM-predicted temperature residuals for flight 12 of the SouthTRAC campaign to high-resolution ECMWF IFS model data shows agreement in the dominant wave packets in terms of orientation, amplitude, and scales. More importantly, the field characteristics are represented well within the MWM prediction, i.e., the wavefronts show similar directions and horizontal distributions as the wave-resolving IFS simulations at all altitudes. Further agreement of the temperature reconstruction is found in the comparison to ALIMA measurements during the same flight. As a side note, a similar agreement was found for GLORIA measurements during the same campaign (see Krasauskas et al., 2023). Although the general matching of the temperature residuals between both data sets is worse than in the IFS case, the most dominant features are resembled by the MWM predictions. In addition, the MWM allows the estimation of the initial source of the individual wave patterns. In this case, the MW source is not limited to the main Andes mountain ridge near and far from the measurements but also lower elevation secondary mountain ridges in the leeward region to the east of the southern Andes.

GWMF distributions can be reconstructed from the ray-tracing data analogously to the residual temperatures. Using the presented reconstruction method, horizontal distributions of GWMF are reconstructed on a global scale for January and July 2006. Comparisons to HIRDLS satellite observations are shown. Note that an observational filter had to be applied to the MWM data to ensure comparability. Overall, the MWM reproduces the features seen in the satellite observations well. Furthermore, the calculated parameters of the individual MWs have been used for an in-depth investigation of patterns in the satellite observations above the Himalaya/Mongolia region for January 2006 and the Southern Andes region for

July 2006.

The MWM performs very well in predicting MW-induced temperature fields and MW propagation, and the GWMF distributions are reliable. Therefore, the MWM can be used for investigating horizontal momentum transport and propagation patterns of MWs in the following chapter. The results shown here are published in Rhode et al. (2023) and partially in Krasauskas et al. (2023) for the lidar observations.

Chapter 5

Oblique Mountain Wave Propagation

The motivation behind the development of the MWM is the investigation of horizontal MW propagation. For this, the raw predictions of the MWM are investigated without filtering and comparison to external data sets in the following. The general horizontal propagation behavior of MWs throughout the year will be derived as well as an efficient approximation of the momentum transport in climate models. To this end, this chapter presents two simplifying but efficient approaches for implementation in GCMs.

First, the MWM-predicted MW activity is shown throughout the year, which allows for an initial assessment of the general MW propagation behavior. In particular, consistent patterns in the global GWMF distributions stemming from orography can be seen, including small-scale islands in the Southern Ocean that are suspected to have a higher influence on the atmosphere as their size suggests. After this first assessment, a detailed description of approximating the horizontal momentum transport by transport matrices follows. In a first approximation, these transport matrices describe the MW propagation from the source region, i.e., the mountains, to the locations in the atmosphere where the waves dissipate. This approach to describe the horizontal propagation is developed within this thesis and published in Eichinger et al. (2023). In addition, they detail the implementation of the description via transport matrices in the chemistry-climate model (CCM) ECMWF/Hamburg (ECHAM5)/Modular Earth Submodel

System (MESSy) Atmospheric Chemistry (EMAC).

Finally, the question is, whether an approximate description of the momentum transport can be done with even fewer changes to the chemistry-climate model. For this, the possibility of describing the horizontal spread of orographic GWMF via diffusion is investigated in this chapter. Using the diffusion model, which is run in the dynamical core within GCMs, might be a very performant solution for spreading the GWMF horizontally from the source columns. Therefore, a first look into the feasibility of this approach for the description of horizontal momentum transport is given in this thesis.

5.1 GWMF propagation time series

In the following, the propagation behavior of MWs is assessed using the MWM presented in Ch. 3. Figure 5.1 shows the annual cycle of the predicted global distribution of GWMF in a monthly mean presentation for 2006 at 25 km altitude. Inter-comparison between the months allows for a first look into the seasonality of the general distribution and seasonal features in particular. Values here are higher than those in Fig. 4.6 and Fig. 4.10 since no (observational) filter is applied. The direct simulation results of the MWM are shown here; thus, the amplitudes might be higher in places than in the previous sections, and additional features might now be visible, which were filtered out previously by the observational filter.

At 25 km altitude, far-going oblique propagation is expected in all regions of high MW activity. The performed ray tracing experiments suggest that most of the propagation happens in a small layer above the tropopause at about 10–18 km. Although the MWs are still horizontally propagating above this level, the extent of it is typically smaller (Strube et al., 2021). In addition, the considered altitude of 25 km is above the summer wind reversal, and therefore the MW signatures in the respective summer hemisphere are strongly suppressed.

The northern hemisphere is covered by high MW activity from October to March. In particular, the Eurasia region shows very high GWMF. The enhanced MW activity is not limited to the Tibetan Plateau and the surroundings with high-elevation orography but is also present above the Alps and the Caucasian Mountains, which are a persistent source

Figure 5.1: Global monthly mean GWMF distributions predicted by the MWM at 25 km altitude for each month of 2006. The shown distributions are taken directly from the MWM, i.e., no observational filter is applied in contrast to Figs. 4.6 and 4.10.

of orographic GWMF throughout the winter months. In contrast, Scandinavia shows less continuous and more intermittent behavior as an MW source. During October to January, Scandinavia is a major source of GWMF, while the activity is strongly suppressed in February and March. This variability might be related to the occurrence of an SSW event in January and the subsequent modifications of planetary wave modes 1 and 2. As expected, wind filtering due to the wind reversal at around 20 km altitude reduces the visible GWMF during the summer months from about April to September. However, the GWMF above the Rocky Mountains persists until mid-April, while the Activity above Asia ceases already during late March.

One of the most dominant patterns seen regularly in the northern hemisphere is a belt of

GWMF above the Northern Atlantic connecting Newfoundland, Greenland, Iceland, Britain, and Scandinavia (see also Fig. 4.6 and Ern et al. (2018)). The MWM predicts this pattern to be most prominent in November to January. During early spring and late autumn, the trailing MWs originating at the east coast of North America do not propagate as far eastward and are thereby more localized. A similar pattern is seen for the MWs originating in Iceland, which strongly contribute to an eastward trail of GWMF. During the rest of the year, i.e., from May to October, the Northern Atlantic is void of GWMF of orographic origin but could be covered by GWs of other excitation mechanisms (e.g. Jia et al., 2014; Geldenhuys et al., 2021). Note that the connected band-like GWMF feature is highly suppressed by the observational filter in Fig. 4.6.

The Southern Andes/Drake Passage/Antarctic Peninsula (SADPAP) region shows the most prominent GWMF pattern of the southern hemisphere throughout the year. In particular, this pattern emerges during March and persists until about December and therefore is present almost throughout the year except for the southern hemisphere summer months. The breakdown during December is in agreement with the final warming date of the polar stratosphere and thus the reversal of the stratospheric winds in the southern hemisphere (e.g. Wilcox and Charlton-Perez, 2013). The MWs above the SADPAP region show much farther eastward spread due to horizontal propagation than seen in the filtered data presented in Fig. 4.10. In particular, the MWs propagate up to the prime meridian in July, which is consistent with the ray tracing study of Sato et al. (2012). In addition, the MWs propagate meridionally from the Antarctic Peninsula and the Southern Andes above the Drake Passage. However, this far momentum transport is not limited to a single month but is more of a persistent year-round feature: If MW activity is present in the SADPAP region, it will propagate to the east south/north. Of course, the stronger the wind speeds, the higher the amplitudes of the GWs, and therefore more GWMF is transported eastward. Thus, the absolute GWMF of this GWMF trail will vary while the shape stays comparable. In addition to the eastward propagation, the data show some spread of GWMF to the west of the Southern Andes, which is even more pronounced at higher altitudes (not shown). Due to refraction in a turning wind field with horizontal shear, MWs can change their orientation and propagate in the seemingly

upwind direction. This westward MW propagation was also observed during the SouthTRAC campaign (Rapp et al., 2021) and investigated in detail by Krasauskas et al. (2023).

Another GWMF feature not visible in the filtered MWM data (Fig. 4.10) is the GWMF originating in South Africa trailing towards the Kerguelen Islands (around 49°S, 69°E) and beyond from May to August. Although South Africa is usually not regarded as a source of high MW activity, it might contribute to the belt-like pattern stretching around the southern Ocean in satellite observations. In addition, the Kerguelen Islands excite high MW activity, which propagates further towards the south-east. This GWMF trail further indicates the contribution of small-scale islands of comparatively low elevation to the missing wave drag at 60°S (c.f. Alexander et al., 2010). Their exposition to strong surface-level winds makes them ideal sources of MWs and our MWM simulations indicate that they contribute up to 20% of the total GWMF in this latitude (see App. A.5). However, the MW propagation from, e.g., the Kerguelen Islands is of a lesser (horizontal) extent than in the SADPAP region, which is in agreement with Perrett et al. (2021), who compared the propagation of MWs excited by small islands and the Southern Andes using ray tracing. Enhanced GWMF above the Kerguelen Islands trailing towards the south-east is also seen in the satellite observations for (austral) autumn months, where the GWMF background is not as dominant, and thereby obscuring, as in Fig. 4.10. Due to the persistence of the GWMF patterns above the Kerguelen Islands and South Africa, they will have a non-negligible impact on the southern hemispheric atmospheric dynamics.

In general, the prediction of horizontal propagation by the MWM agrees with expectations from wind considerations and previous studies on oblique MW propagation. Especially the global hotspots of GW activity, i.e., the SADPAP region, New Zealand, and the northern Atlantic, are also the origins of far-propagating MWs. In addition, small-scale islands, e.g., the Kerguelen Islands, Falkland Islands, and South Georgia, exhibit high MW activity throughout the year. More unexpectedly is the comparatively strong influence of MWs originating in South Africa on the Southern Ocean. The propagation patterns seem consistent throughout the seasons, and there is not much variation in the general propagation behavior in the considered monthly means.

Similar patterns arise over the course of the winter season, which mainly vary depending on the amplitudes of the GWs. However, the direction of the momentum transport is mostly determined by the orientation of the orography. This low seasonal variance of the transport direction indicates a flow-independent GWMF transport pattern that describes the MW propagation to the first order. The construction of such a first-order transport pattern is investigated in the following sections.

5.2   Transport matrices and redistribution

The technical approximation of the momentum transport pattern due to MW propagation is comparatively straightforward. Within the parameterization scheme, the MWs originating in each grid column propagate vertically up to a given altitude level. At this level, the total GWMF of this grid column is horizontally redistributed to target grid cells following a statistic, or transport matrix, estimated from ray tracing simulations. In other words, the transport matrix prescribes how much of the GWMF originating in any given grid column is transported to any other grid cell due to horizontal MW propagation. After applying the redistribution, the MWs propagate vertically in their new respective model columns according to the parameterization scheme. The level at which the GWMF is redistributed, i.e., the redistribution height H_{redist}, splits the MW description into two regimes: below this level, the MWs are described as vertically propagating in their source column, and above, they are described in the approximated grid columns, to which they will propagate, and thereby transport their momentum, within their lifetime. The advantage of this approach is the amount of freedom in the parameters of where to apply the redistribution and how the prescription is constructed. For example, different transport matrices could be generated and used for different synoptic wind situations. In addition, the one-time redistribution requires communication between different grid columns just once, which makes it highly efficient compared to approaches resolving the horizontal propagation at every level explicitly.

5.2.1 Construction of the transport matrices

The ray tracing methodology of the MWM allows for examining the location of each MW at any given altitude between initialization at the mountain and termination in the atmosphere. Therefore, each contribution to the global GWMF distributions can be associated with a source location and is thus fully characterized by the amount and traveled distance since excitation. The construction of the transport matrices explicitly uses the information on the amplitude and position of the modeled MWs at any point. If the number of considered MWs and wind situations is high, the so-generated transport matrix gives a statistical approximation of momentum transport due to MW propagation.

Since the transport matrices describe the redistribution rule from each model source column to the target grid cells, they resemble a linear mapping between the source and target grid (which are identical since the grid resolution does not change above the level of redistribution). The individual entries of this mapping are proportional to the amount of GWMF launched in the given source grid cell and transported to the respective target grid cell. The horizontal resolution depends on the GCM and is an inherent property of the transport matrix and directly influences the statistical quality of the mapping. Coarser grid cells cover more MW sources and launched MWs and therefore have better statistics, while the precision of the transport allocation of the propagation approximation is reduced.

As a linear mapping from the horizontal source grid location to the target grid location, the transport matrix can be written as a 4D matrix, $\mu_{\mathrm{rd}}(\phi_{\mathrm{src}}, \lambda_{\mathrm{src}}, \phi_{\mathrm{tar}}, \lambda_{\mathrm{tar}})$, where ϕ and λ denote latitude and longitude, respectively, and the subscript *src* refers to the coordinates, where the MWs originate and the subscript *tar* refers to the coordinates, where the MWs propagate to. A schematic illustration of the transport matrix construction is shown in Fig. 5.2a. Note again that the redistribution is done only once at a single altitude level.

The individual entries of this mapping are calculated by iterating over all ray-traced MWs launched for the considered period. For each, the source location, i.e., ϕ_{src} and λ_{src}, is taken as the initialization location. The target location, i.e., ϕ_{tar} and λ_{tar}, is taken as the latitude and longitude of the MW at a specified altitude, the target height H_{target}. This parameter allows more control over the generated transport matrix by varying this height and investigating
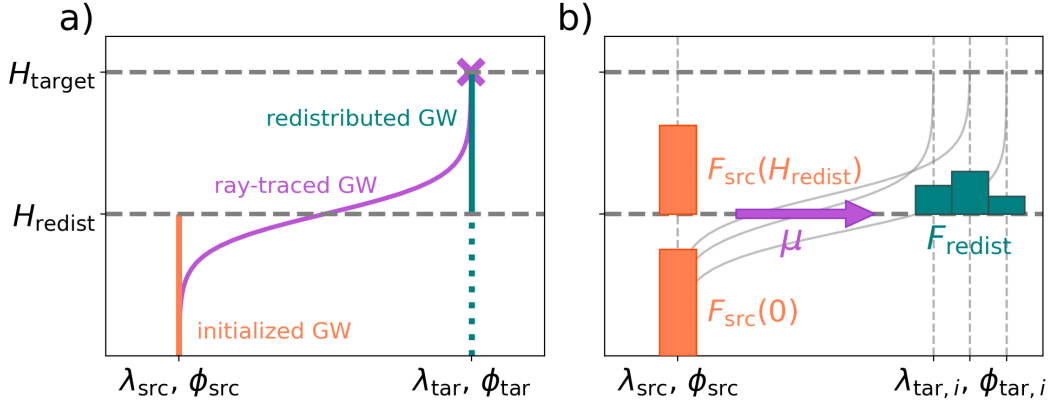
Figure 5.2: Schematic of the construction of transport matrices and the according redistribution of GWMF. Panel a shows the basic idea of the construction of the transport matrix. For each MWM-initialized MW (violet line), the source and target locations, $(\phi_{\mathrm{src}}, \lambda_{\mathrm{src}})$ and $(\phi_{\mathrm{tar}}, \lambda_{\mathrm{tar}})$, are estimated. The target location is estimated at a set target height, H_{tar}, and the corresponding amplitude at that altitude serves as the weight for the transport matrix. Once implemented in a parameterization scheme, the propagation is approximated by vertical propagation at the source location up to the redistribution height H_{redist} (orange line) and at the estimated target location of the original ray-traced MW beyond (teal line). Repeating this process for every launched MW gives the total transport matrix. Panel b shows a schematic of the full redistribution process as implemented by Eichinger et al. (2023). Following the upward propagation of the total column GWMF in any given grid column up to the redistribution height (orange bars), the total GWMF at that altitude, $F_{\mathrm{src}}(H_{\mathrm{redist}})$, is redistributed to multiple grid cells according to the transport matrix μ to get the redistributed GWMF distribution F_{redist} (teal bars).

the effect on redistribution performance. In case of a GW not propagating as high as H_{target}, the last position of the GW before termination is taken as the target location. Now the corresponding GWMF carried by the considered MW is added to the respective entry of the transport matrix, i.e., $\mu_{\mathrm{rd}}(\phi_{\mathrm{src}}, \lambda_{\mathrm{src}}, \phi_{\mathrm{tar}}, \lambda_{\mathrm{tar}})$. Once this is done for all ray-traced MWs, the matrix μ describes the transport of absolute GWMF values, i.e., the total GWMF ending up in a given grid cell due to MW propagation under the condition that it launched in the considered source grid cell. In order to construct a redistribution matrix that gives the fraction of the GWMF originating in one location that is transported to any other location, this matrix has to be normalized by enforcing

$$\sum_{\phi_{\mathrm{tar}}, \varphi_{\mathrm{tar}}} \mu_{\mathrm{rd}}(\phi_{\mathrm{src}}, \varphi_{\mathrm{src}}, \phi_{\mathrm{tar}}, \varphi_{\mathrm{tar}}) = 1 \ \ \forall \ (\phi_{\mathrm{src}}, \varphi_{\mathrm{src}}). \tag{5.1}$$

On a side note, this normalization ensures the conservation of the GWMF by keeping the sum of the redistributed GWMF over the target grid cells the same as the total GWMF in the source grid cell. The normalization in Eq. 5.1 is also enforced above regions where no MWs were launched by the MWM, e.g., above the ocean. In this way, the GWMF is untouched if the GCM predicts any in these regions and will propagate further upwards after redistribution.

The transport matrices considered in the following are constructed from the same MWM simulations described in Sec. 5.1 that are mostly based on the atmospheric conditions given by ERA5 reanalysis data. Although this is still a static derivation, it accounts for the general physical processes and varying conditions much better than the columnar parameterization schemes. An example of a transport matrix is shown in Fig. 5.3a, where the redistribution from the source grid cell at 48.8°S, 70.3°W (light blue square) is illustrated. In particular, this transport matrix is generated for the MWM simulation of July 2006 on a horizontal resolution of ~2.8°×2.8°, which is a typical horizontal resolution for long-term climate simulations in EMAC, and the target altitude is set to 40 km. The color shading shows the fraction of the GWMF originating in the source grid cell that ends up in the colored grid cell due to horizontal momentum transport. In this specific example, almost the complete GWMF is transported from the original model column towards the Drake Passage in the southeast. In addition, some of the GWMF is spread to the northeast and barely anything to the west, where the wind is typically coming from. In general, the redistributed GWMF is much less localized and widespread. The underlying topography within each grid cell exhibits multiple ridges of different orientations and widths, leading to high variability in the transport pattern of the individual launched MWs and, thus, various directions of momentum transport in this statistical consideration. Figure 5.3b shows the same transport matrix summed over all source grid cells, which gives a first indication of the general effect of the redistribution. Values above 100% (red) indicate a likely increase of GWMF due to redistribution, while values below 100% (blue) indicate the opposite. As expected, the redistribution is reducing the GWMF in the orographic variable regions and relocating it towards the oceans and regions of flat terrain. Especially in the Drake Passage, a high enhancement of GWMF is expected due to
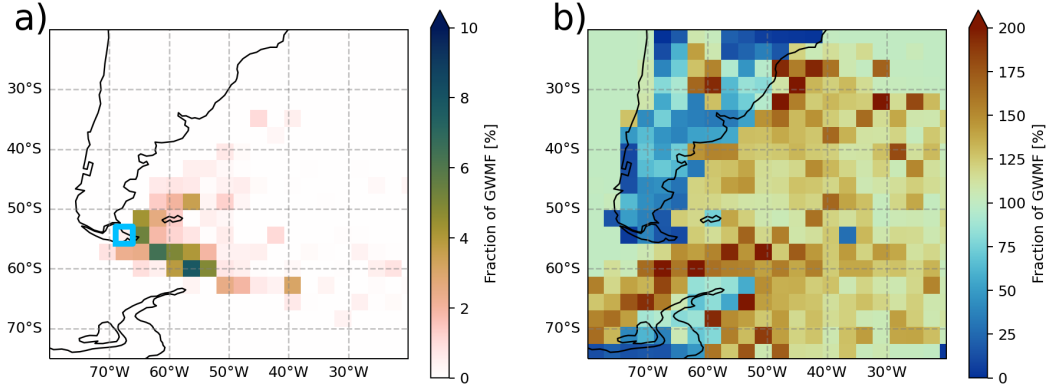
Figure 5.3: Exemplary transport matrix for July 2006 on a $\sim 2.8° \times 2.8°$ resolution and for a target height of $40\,\mathrm{km}$. The color shading in panel a shows the fraction of GWMF that is transported out of the source grid column at 48.8°S, 70.3°W (light blue square) to the corresponding grid cell according to this transport matrix. Panel b shows the transport matrix summed over all target grid cells; therefore, it gives a first estimate of the general redistribution of GWMF by the transport matrix. Values below 100% (blue colors) correspond to a reduction, and values above 100% (red colors) to an enhancement of GWMF due to the redistribution using this transport matrix.

the redistribution. Note, however, that this is only a first indication of the redistribution effect since only the GWMF fractions are summed and not the total GWMF itself, i.e., the strength of the source is not taken into account in this illustration.

5.2.2 Approximation quality of transport matrices

The transport matrices approximate the horizontal propagation of MWs; therefore, the horizontal momentum transport and, subsequently, the relocation of GW drag. The approximation quality, i.e., the accuracy of the approximated GWMF transport, is estimated by applying the redistribution to synthetic data of the MWM, where information on the exact GWMF transport is available as the reference. Further, this test can be used to estimate optimal values for the two parameters on which the transport matrix and the redistribution depend: the target height H_{target} and the redistribution height H_{redist}. Thus, the described method resembles a two-parameter approach. Both parameters can be estimated independently from each other since they are used in different stages of the redistribution process. The target height H_{target} is the altitude at which the location of the ray-traced MWs is taken as the destination of the momentum transport. Therefore, this parameter directly influences

the shape and values of the transport matrix. In contrast, the redistribution height H_{redist} is the altitude at which the redistribution according to the transport matrix is performed to the GWMF data set without horizontal propagation or the MW parameterization scheme in EMAC. Therefore, varying H_{redist} only affects the GWMF after redistribution. Therefore, in the following, both parameters are considered separately, starting with the target height.

Figure 5.2b illustrates the redistribution process schematically. The GWMF propagates strictly vertically in the grid column, where it originates, up to the redistribution height. It is then redistributed to the target grid cells according to the entries of the transport matrix μ. To estimate the approximation quality of the redistribution, an MWM simulation with horizontal propagation deactivated serves as the "status-quo" simulation, i.e., the current situation in MW parameterization in GCMs, and is called VERT in the following. The VERT simulation is then redistributed with different transport matrices and compared to the fully-propagating MWM simulation, which is the aim of the approximation, i.e., the reference for optimal propagation approximation, and further labeled as the REF simulation. In this way, the behavior of the MW parameterization and subsequent redistribution in EMAC is captured while still being able to compare to the explicitly modeled horizontal propagation of the MWM simulations.

Figure 5.4a, b, d, and e show the root-mean-square deviation (RMSD) for GWMF and GW drag distributions between the VERT run and the redistributed VERT data to the fully horizontally propagating REF simulations. The considered underlying distributions are the monthly mean of MWM simulations for July 2006, and the RMSD is calculated globally across all latitudes and longitudes. In this test, the redistribution of the VERT data set is applied at the lowest altitude level, which allows inspecting the redistribution through all altitudes and removes H_{redist} from the considerations for now. However, this causes reduced approximation quality at the lowest altitudes, where the VERT data set is a better approximation to REF than the redistributed ones because the MWs have not yet propagated as far from the source as the redistribution prescribes.

For the first test, the transport matrices are constructed from the same MWM data of July 2006, on which the redistribution is applied afterward. Figures 5.4a and b show

the resulting RMSD to the REF simulation for GWMF and GW drag, respectively. For the VERT simulation (black line), the RMSD to the reference in GWMF increases with altitude until it plateaus at about $8\,\mathrm{mPa}$ between $17\,\mathrm{km}$ and $30\,\mathrm{km}$ altitude. The increase in RMSD can be explained by GWs propagating increasingly further from their sources, thereby horizontally spreading the GWMF. The propagation leads to the VERT simulation increasingly deviating from the REF simulation at higher altitudes. In contrast, the total orographic GWMF decreases with altitude due to wave breaking and saturation, leading to a decrease in RMSD. In the altitude range of about 17–$30\,\mathrm{km}$, both processes cancel out such that the RMSD is almost constant. Beyond $30\,\mathrm{km}$ altitude, the RMSD decreases again due to wave breaking reducing the amplitudes of the propagating MWs stronger than further spreading could counteract.

The colored lines in Fig. 5.4a show the RMSD for the redistributed GWMF, with the color giving the target height H_{target} for which the transport matrix is constructed. As expected, the curves of RMSD show a minimum at the altitude corresponding to H_{target} since they are constructed to represent the GWMF transport at this altitude as well as possible. Moreover, a high reduction in RMSD of at least a factor of 2 can be seen for all shown transport matrices. A trade-off between correctly approximating the GWMF at lower altitudes (see $H_{\mathrm{target}} = 10\,\mathrm{km}$) and at high altitudes (see $H_{\mathrm{target}} = 40/50\,\mathrm{km}$) becomes evident as well. As a side note, the ideal redistribution height H_{redist} should be located above the crossing of the colored and the black line such that the redistribution reduces the RMSD at all levels above and no over-representation of the horizontal propagation is introduced.

Figure 5.4b shows the RMSD for the same transport matrices for GW drag on a logarithmic scale. As the atmospheric density decreases with altitude, the GW drag per GWMF increases accordingly. Therefore, the comparatively worse performance of high H_{target} at lower altitudes has a much lower impact on the dynamics than the inaccurate representation of low H_{target} at high altitudes. Overall, the approximated relocation of GW drag for $H_{\mathrm{target}} > 20\,\mathrm{km}$ is very similar up to $40\,\mathrm{km}$ altitude.

The altitude integrated reduction in RMSD, i.e., the RMSD of the redistributed data subtracted from the one for the VERT simulation divided by the summed RMSD for the

VERT simulation, is shown in Fig. 5.4c for GWMF and GW drag. Here only the RMSD above the crossing of the colored and the black line is considered such that the maximum possible improvement by redistribution is assessed. In the case of GWMF, the curve exhibits a distinct local maximum at $H_{\text{target}} \approx 30$,km before the redistribution overestimates the extent of the horizontal momentum transport at lower altitudes too strongly and subsequently, the performance deteriorates. The optimum performance for GW drag is achieved with $H_{\text{target}} \approx 40$,km, which is expectedly higher than for GWMF due to the increase of GW drag, and thereby RMSD, with altitude.

Ideally, the transport matrix is constructed from a longer period than a single month such that different atmospheric conditions are statistically resembled. Therefore, Fig. 5.4d–f show the same RMSD analysis for redistribution of the VERT simulation according to transport matrices constructed from MWM simulations of the whole year 2006 but with the redistribution still applied to July of 2006. In general, the performance is very similar to the previous case. Noteworthy, however, is that the improvement of the GW approximation in Fig. 5.4e is increased for $H_{\text{target}} \approx 40\,\text{km}$ above $10\,\text{km}$ altitude and decreased below. This increased approximation performance at high altitudes can be explained by the increase in statistics by considering 12 times as many MWs, while the decreased approximation performance at lower altitudes is caused by tropospheric fluctuations and seasonalities throughout the year that are captured by the annual mean transport matrices. The optimal values for H_{target} of about $30\,\text{km}$ and $40\,\text{km}$ for GWMF and GW drag, respectively, are unchanged. For GCMs, the major interaction of the MW parameterization with the simulations is the influence on the dynamics via the exerted GW drag and, thus, in the following transport matrices are constructed with $H_{\text{target}} = 40\,\text{km}$, which gives the best reduction in RMSD for GW drag.

After fixing the optimal value for H_{target} to $40\,\text{km}$, the next question is: what is the ideal parameter value for the redistribution height H_{redist} for this transport matrix? The optimal redistribution height is the altitude, where the RMSD profiles of the redistributed data and the status-quo VERT data cross, i.e., the crossing point of the colored and the black line in Fig. 5.4b and e. Therefore, the optimal redistribution height will vary depending on the atmospheric conditions and the season. For simplicity, however, a fixed redistribution
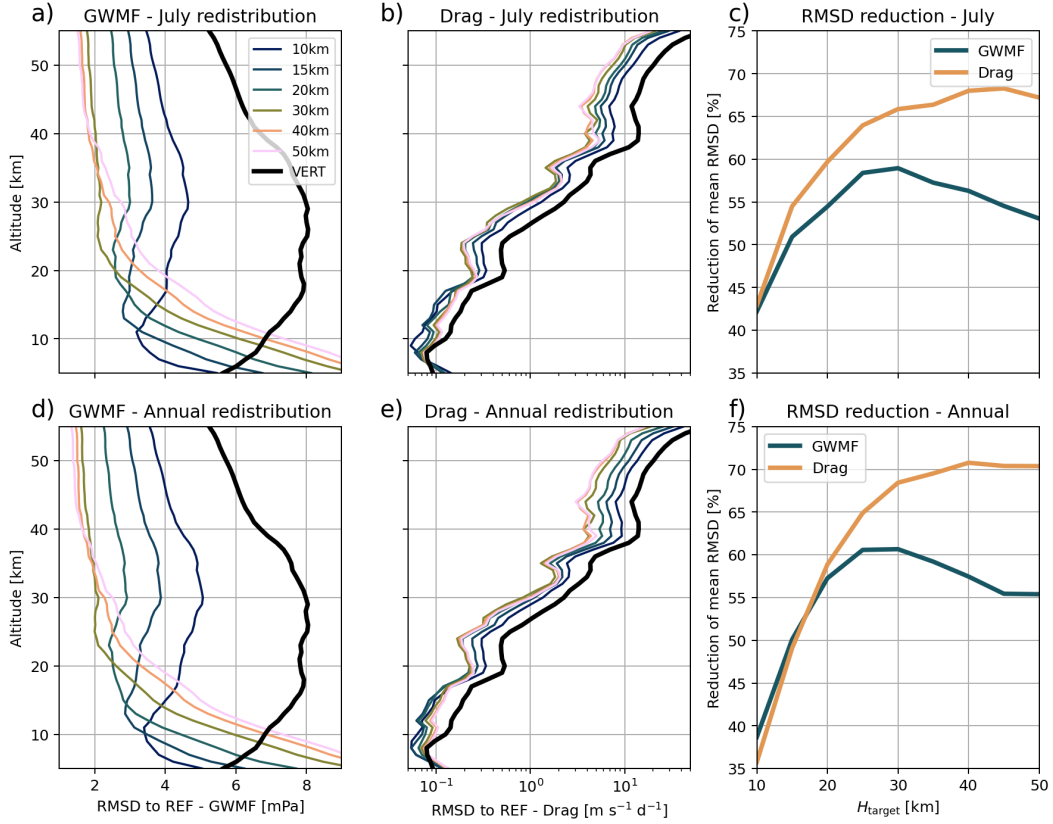
Figure 5.4: Comparison of MWM simulations without horizontal propagation (VERT, black lines) and approximated propagation via one-time redistribution according to transport matrices constructed with different H_{target} (colored lines). Shown are the root mean square differences (RMSD) with respect to the fully horizontal propagating MWM simulation (REF) for GWMF (panels a and d) and GW drag (panels b and e). Panels c and f show the total reduction in RMSD achieved by redistribution using the transport matrix of the given H_{target} through all altitude levels. Only the altitude levels, where the redistribution leads to an improvement, i.e., the altitudes above the crossing of the colored and the black curves, are considered here. The transport matrices are generated from ray tracing from July 2006 for panels a-c and the entire year 2006 for panels d-f. In both cases, the redistribution is applied to the GWMF or GW drag from an MWM simulation of July 2006. Note the logarithmic scale for GW drag.

height is used for the first implementation of this approach of approximating horizontal MW propagation. In particular, such a varying redistribution height needs to be calculated at runtime using the GCM forecast, which complicates this simplified approach unnecessarily and significantly reduces the computational performance.

An optimized mean redistribution height is determined by performing the redistribution on different altitude levels for multiple atmospheric conditions and periods and maximizing

the achieved reduction of RMSD to the fully propagating REF simulation compared to the VERT simulation (see Fig. 5.4c and f). Figure 5.5a shows the RMSD reduction for GW drag with respect to the VERT simulation for redistribution heights between $5\,\text{km}$ and $31\,\text{km}$ altitude and all months of 2006. As expected, the GW drag is comparatively insensitive to the redistribution height due to the exponential growth with altitude; therefore, the correct approximation at high altitudes outweighs the overestimated transport at lower levels for the most part. However, a smaller decrease in approximation quality is seen with redistribution altitudes above $10\,\text{km}$ altitude. Similarly, the performance decreases if the redistribution height is chosen below $10\,\text{km}$ altitude due to an overestimation of the horizontal momentum transport, thereby predicting GW drag at locations where it will propagate only at higher altitudes. In all cases, the improvement in total RMSD is above 40% throughout the year.

The annual average improvement of the RMSD for GWMF and GW drag by applying the redistribution in dependence of the redistribution height is shown in Fig. 5.5b. As already seen in Fig. 5.5a, the GW drag is not very sensitive to H_{redist} and is almost constantly around 60% up to $18\,\text{km}$ redistribution height with a following minor decrease beyond. In contrast, the GWMF is highly dependent on the redistribution height and noticeably shows the trade-off between correctly approximating the momentum transport at higher altitudes versus the overestimated momentum transport at low altitudes. A clear maximum of the RMSD improvement is given for $H_{\text{redist}} \approx 11\text{--}15\,\text{km}$. Physical considerations support this range for applying the MW redistribution within the GCM: this altitude is above the tropopause and below the (summer) wind reversal. Both highly affect GW propagation and breaking, and, in addition, MWs tend to propagate over-proportionally far in this altitude range, as simulated with the MWM (c.f. Strube et al., 2021).

5.2.3 Implementation in EMAC

Although the described approach for approximating the horizontal MW propagation by re-distributing the model-predicted GWMF at a single level is comparatively simple, it accounts for a large part of the deviations caused by the lack of horizontal propagation in the simulated tests. In particular, a single transport matrix constructed from multiple months or
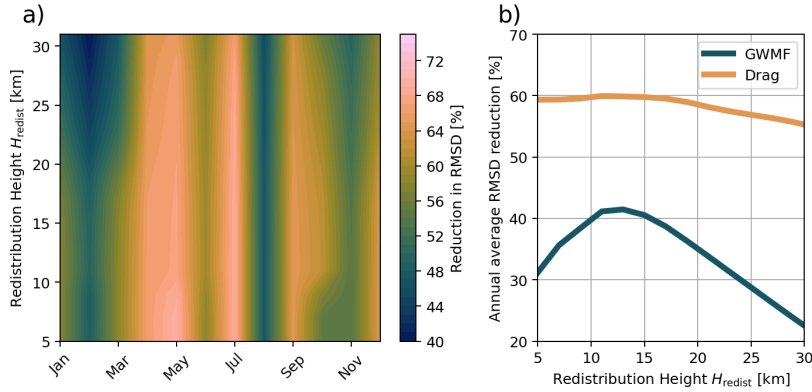
Figure 5.5: Reduction, or improvement, in the RMSD to the fully propagating REF simulations by redistributing at various redistribution heights compared to the VERT simulation without horizontal propagation. In color shading, panel a shows the RMSD improvement for the GW drag throughout the year by redistributing with a transport matrix generated from one year of ray-tracing data. Panel b shows the corresponding annual mean reduction in RMSD for GWMF and GW drag in dependence of the redistribution height H_{redist}.

years of data might describe the horizontal spread of orographic GWMF well enough to reduce the deviation of GW drag from a fully propagating representation by up to 60%. This high agreement further indicates that a large part of MW propagation, on average, follows a general pattern. Accounting for this pattern by redistribution is the first step towards a more realistic but, at the same time, fast parameterization of orographic GWs. Due to the one-time redistribution, the GCM simulation has to communicate the GWMF between model columns at just one level, which is comparatively cost-efficient.

The ideal parameters for the transport matrix and the redistribution are estimated to be $H_{\mathrm{target}} = 40\,\mathrm{km}$ and $H_{\mathrm{redist}} = 15\,\mathrm{km}$. These values are used in the technical implementation of this approach into the CCM EMAC by Eichinger et al. (2023). Most importantly, the redistribution closes the gap of GWMF at 60°S (see their Figs. 8 and 9). In addition, they provide a first look into the changes within the CCM due to the improved parameterization in terms of wind speeds, temperature, and nudging tendencies. Furthermore, they assess the performance cost of this improved parameterization and state that it is very reasonable for long-term climate simulations in EMAC.

5.3 Propagation approximation via diffusion

The implementation of the transport matrices is still a major change within the model. A possible way of approximating the horizontal spread of GWMF due to oblique MW propagation with fewer modifications to the model itself is a description via diffusion. One of the main challenges of this approach is that the GWMF does not necessarily follow general diffusion patterns but has a directional preference, e.g., toward the east in the SADPAP region. Therefore, setting up diffusion coefficients from modeled, propagating MWs from, e.g., the MWM, resulting in consistent and realistic GWMF distributions is challenging. A general diffusion between adjacent grid cells could, however, possibly describe the basic horizontal spread of GWMF around their sources, thereby reducing the sharp discontinuities in nudging tendencies within GCMs. This approach is of special interest since most climate models already implement a sophisticated diffusion module in the dynamical core, where calculations are fast. Thus, such an implementation could prove very efficient in terms of computational efficiency.

The basic idea for a first case study is to use standard isotropic diffusion in two dimensions, which is described by Fick's law and the differential equation:

$$\left(\frac{\partial F(x,y)}{\partial t}\right)_{\text{diff}} = \nabla \cdot (D(x,y)\nabla F(x,y)) \tag{5.2}$$

$$= D(x,y)\Delta F(x,y) \qquad\qquad +\partial_x D(x,y)\partial_x F(x,y) \tag{5.3}$$

$$+\partial_y D(x,y)\partial_y F(x,y), \tag{5.4}$$

where F is the field undergoing diffusion, e.g., particle concentration or GWMF in this case, and D is the diffusion coefficient. For now, the diffusion coefficient is isotropic and local, i.e., it varies in space, thereby allowing for the description of regionally varying propagation patterns. Anisotropic diffusion could approximate propagation patterns of directional character more precisely but requires four times as many parameters and a much more involved model. Therefore, for a first feasibility study, the diffusion is kept isotropic.

The horizontal transport of GWMF between altitude levels will be modeled by horizontal diffusion. Afterward, the breaking and saturation of the MWs are considered, which reduces the GWMF in the respective altitude. Therefore, this approach adds an additional step to the MW scheme, in which the GWMF diffuses following the pre-calculated diffusion coefficients before it propagates to the next altitude.

As mentioned before, the challenge is the estimation of the diffusion coefficients D. Here, D is estimated from GWMF distributions simulated with the MWM for July 2006 (see Sec. 4.3.2) as the underlying reference data set. Using Eq. 5.4 as the forward model, the diffusion coefficients D can be gained by optimization to the given GWMF distribution. In particular, the loss function

$$L = F(z_{i+1}) - \left(F(z_i) + \left(\frac{\partial F(z_i)}{\partial t}\right)_{\text{diff}}\right) + \Lambda||D(z_i)||_1 \tag{5.5}$$

gives the deviation of the diffusively predicted momentum flux transport from the actual momentum flux transport and is minimized using a standard least-squares optimization algorithm. The diffusion coefficients D are restricted to be positive, Λ is the Tikhonov regularization parameter, and $||\cdot||_1$ gives the L^1-norm. The optimization results in a sparse diffusion coefficient matrix for each altitude. The entries vary with location and approximate the local horizontal spread of GWMF via horizontal propagation according to Eq. 5.4.

Figure 5.6a and b show the horizontal cross-section of GWMF at $40\,\text{km}$ altitude as simulated by the MWM and approximated using the diffusion coefficients, respectively. For this comparison, the lowest altitude level of $5\,\text{km}$ gives the starting point with the GWMF of higher altitudes calculated using Eq. 5.4 and the diffusion coefficients D. Note that the diffusion only approximates the horizontal spread but neither GW breaking nor saturation. For comparability, a simple reduction in amplitudes is applied by normalizing the summed GWMF at each altitude level to the same value as in the MWM simulation. Therefore, the amplitude reduction is unphysical in this first consideration, and the GWMF can only be assessed qualitatively. Within the GCM, the amplitude reduction would be taken care of by

the parameterization scheme and should not be modeled additionally by the diffusion. Especially above the southern Andes, the GWMF is significantly spread from the land toward the ocean. This redistribution of GWMF, however, resembles more smearing out of the original distribution than proper MW propagation with the wind. Compared to the MWM simulation in panel a, the diffused GWMF shows too strong values above the Atlantic Ocean and too little GW activity above the Pacific Ocean. Note, however, that at this altitude level, the diffusion was applied 35 times in total; therefore, small errors could add up.

The zonal mean GWMF for the MWM simulation and the diffusive approximation are shown in Fig. 5.6c and d, respectively. The gap at 60°S is more pronounced in the diffusive approximation, but there is some spread into this region. Diffusion could therefore be a first-order approximation of at least the spread of the GWMF around the initial sources. This smearing could reduce the sharpness of nudging tendencies, which is currently observed in GCMs. Especially in the SADPAP region, too much GWMF is modeled above the mountains and too little in the direct surroundings of the topographic grid cells. Therefore, implementing this approach into a GCM could prove worthwhile as an alternative approach for improving MW parameterization, especially if it can be implemented in the dynamical core, where the calculation costs are low.

Chapter summary

This chapter shows the general propagation behavior of MWs throughout the year and how estimating the momentum transport pattern can be harnessed for improving MW parameterization schemes in GCMs. In particular, the momentum transport due to oblique MW propagation can be described with a transport matrix (see also Eichinger et al., 2023). These transport matrices are constructed from individual ray-tracing data from MWM simulations, which allows for the precise allocation of the source and target of the momentum transport by following the GW along its path through the atmosphere. Considering reasonably large data sets and periods, the general momentum transport pattern is estimated statistically.

This transport matrix is used to approximate the horizontal propagation of MWs within
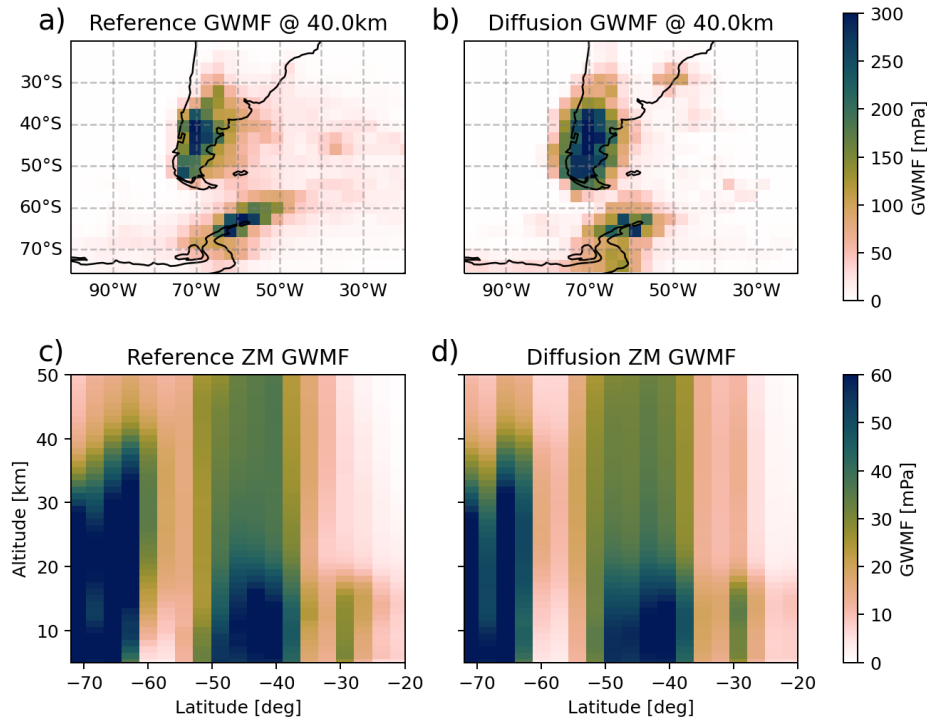
Figure 5.6: Horizontal spread of the GWMF due to horizontal propagation simulated by the MWM and as approximated by diffusion. Panels a and b show the horizontal cross-section of GWMF at 40 km altitude above the SADPAP region for the reference MWM simulation and the diffusively approximated GWMF transport, respectively. The corresponding zonal mean of GWMF over this region is shown in panels c and d.

MW parameterizations by redistributing the predicted columnar GWMF at a single altitude level to the statistically estimated target regions. In this way, the GWMF spreads across the horizontal and is closer to the physical location of the MWs. The performance of this approximation, i.e., how good a one-time redistribution approximates the full propagating MWM simulations, depends on assessing the GWMF or the resulting GW drag. The spread of GW drag, which strongly affects wind predictions in GCMs, is approximated by up to 60%. The good agreement using a fixed transport matrix indicates that a large part of horizontal MW propagation can be described by a more-or-less general pattern. The technical implementation of this approach in the GCM EMAC is shown in more detail in Eichinger et al. (2023) and is comparatively computationally cost-efficient. This modification is part of MESSy and can, in principle, be used by anyone working with EMAC.

Furthermore, this chapter showed a second approach for improving MW parameterization

schemes in climate models. Most models already integrate a sophisticated diffusion model within the dynamical core; therefore, an approximation of the horizontal momentum transport by diffusion might be possible. A showcase of this approach was given in this chapter. The necessary diffusion coefficients can be estimated from MWM simulations by assuming diffusive propagation between altitude levels. This approach might be faster than the redistribution using transport matrices due to the implementation in the dynamical core but not as precise in describing the horizontal propagation of MWs physically accurately. However, the GWMF could be spread around the source columns following a physics-based prescription, thereby reducing the sharpness of nudging tendencies in these regions.

Both approaches are promising for further investigation. Using the transport matrices for long-term climate projections and experimenting with different settings could shed light on the effect of horizontal MW propagation on the climate. In particular, the long-term projected dynamics should profit from the relocation of the drag. On the other hand, implementing the diffusion approximation in a model could be another simple method for alleviating model biases.

Chapter 6

Summary and outlook

Gravity waves (GWs) are one of the dominating forcing processes within the middle atmosphere by transporting momentum between different altitude levels. However, the lateral momentum transport due to oblique propagation of GWs is not captured in general circulation models. Orography, as one of the main GW sources, is described by a parameterization scheme within the model due to the too-coarse resolution. In general, these schemes only allow for vertical propagation of the MWs; therefore, the deceleration of the background wind is localized to the model column above the mountain source. Studies show, however, that the oblique propagation of MWs from the source region is an integral part of atmospheric dynamics. This lateral propagation might not only relocate the MW forcing horizontally but also prevent MW from breaking at lower altitudes if the MWs circumvent critical levels and propagate into regions with favorable propagation conditions allowing for further vertical propagation and higher amplitudes. Resolving small-scale MWs explicitly in climate projections, however, would require an increase in horizontal resolution by at least a factor of 30 in longitude and latitude compared to the common T42 resolution (about $2.8° \times 2.8°$), which alone would lead to an increase in computation cost of five orders of magnitude (note that the time and vertical resolution have to increase as well). This computational expense is simply infeasible for climate studies even on supercomputers in the foreseeable future. Therefore, this thesis studies alternative approaches of cost-effectively approximating the horizontal momentum transport due to oblique propagation. The general idea is that a generalized propagation

pattern can be estimated statistically and harnessed for improving the MW parameterization scheme in the general circulation models (GCMs).

The first step to estimate the MW propagation pattern is the realistic description of MW sources from orography. One possible way to achieve this is by approximating the underlying elevation data with a collection of two-dimensional mountain ridges, for which the MW excitation is described by theory. Hence, Chapter 3 and parts of Rhode et al. (2023) answer the question: **How to optimally approximate the elevation data by a small number of two-dimensional mountain ridges?** For estimating the mountain ridges, the elevation data is scale-separated using a Fourier transformation filter and further reduced to a skeleton of the ridge lines. The candidates for mountain ridges correspond to straight line segments in this skeleton; therefore, a line detection algorithm, the Hough transformation, can be used to provide the locations, orientations, and lengths of mountain ridge candidates. A fit of idealized mountain ridges of a sinusoidal cross-section at the detected locations gives the height and width of the given candidate, from which the initial displacement amplitude and horizontal wavelength are inferred using MW theory. Applying this algorithm to various scales results in a collection of idealized mountain ridges that, on the one hand, approximate the topography and, on the other hand, give a global distribution of MW sources. The mountain wave model (MWM) is constructed by combining the MW source ridges with the ray tracer GROGRAT for propagating the MWs through the atmosphere.

In order to validate the MWM, the predicted horizontal propagation has to be compared to high-resolution model data and direct observations of GWs. Both can provide GW-induced residual temperatures and GW momentum flux (GWMF), which may also be reconstructed from the MWM ray-tracing data by superposition of the individual MW contributions. Chapter 4 and Rhode et al. (2023) show algorithms for reconstructing 4D-distributions of both quantities from the MWM by assuming a single finite wave packet for each MW along its trajectory, thereby answering the questions: **Can the combined MWM estimate residual temperature perturbations reasonably in comparison to high-resolution model data and observations? Is the MWM able to predict global GWMF distributions?** The comparison of residual temperature prediction from the MWM to a simple, analytical

Fourier mountain model confirms that temperature reconstruction can be done from ray tracing. Furthermore, a comparison to the high-resolution integrated forecast system (IFS) of the European Centre for Medium-Range Weather Forecasts (ECMWF) shows that changes in the general MW field characteristics, i.e., the amplitudes, turning of phase fronts, and horizontal propagation, with altitude are captured well by the ray tracer and source model. In particular, the eastward propagation in the southern Andes region is predicted by the MWM. The prediction of GWMF agrees with HIRDLS satellite observations of orographic GWs in the Upper Troposphere/Lower Stratosphere (UTLS) for January and July of 2006. Furthermore, the satellite observations can be interpreted using the individual GW parameters and distributions of the MWM. This allows for an explanation of observed structures above the Himalayan Plateau and the southern Andes. Therefore, the MWM can be trusted to model the horizontal transport of GWMF from their sources, and propagation patterns are estimated in the following steps.

The subsequent study of MW propagation is based mostly on the MWM predictions. The propagation behavior throughout 2006 and the construction of general propagation patterns are considered in Chapter 5 and published in Eichinger et al. (2023). The MWM predictions show that, in the monthly mean, the general propagation behavior, i.e., the relocation of momentum, is mostly dependent on the fixed ridge parameters and not so much on the varying synoptic conditions, which mainly influence the amount of GWMF. The ray tracer allows the source allocation of each individual contribution to these global GWMF distributions. Subsequently, constructing a simple MW transport matrix is possible using the ray-tracing data, allowing for a one-time redistribution of horizontal momentum, which provides a more realistic representation of GW effects than current columnar parameterization schemes. The approximation quality of this one-time redistribution is estimated using the MWM with deactivated horizontal propagation and subsequently redistributing the resulting columnar GWMF at a single altitude level to the estimated target locations according to the transport matrix. This results in a two-parameter approach depending on the target height H_{target} and the redistribution height H_{redist}. The performance of this one-time redistribution is measured against the MWM predictions with active horizontal MW propagation, which defines the best-case, or

reference, scenario. This redistribution can reduce the root-mean-square deviation by up to 40% for GWMF and by up to 60% for the resulting GW drag in comparison to the columnar restricted simulation, i.e., to the status quo for MW parameterization schemes. The ideal altitude for this redistribution is estimated to be about $15\,\mathrm{km}$. Therefore, Chapter 5 answers the final to last questions: **How to construct a transport matrix that can approximate the horizontal transport of GWMF due to horizontal propagation?**

Afterward, an alternative approach of spreading the GWMF from the source regions between altitude levels is discussed, answering the last question: **Is it possible to describe the horizontal MW spread using anisotropic diffusion?** Here, the diffusion model is limited to be isotropic but local for a proof of concept. The calculation of reasonable diffusion coefficients is not as straightforward, and the approximation of the horizontal propagation is not as precise and realistic as with the transport matrix approach. However, the diffusion could reduce the sharpness of nudging tendencies around orographic regions in GCMs by simply spreading the GWMF around the sources on a physical basis. Therefore, implementing this approach into a GCM would be a worthwhile follow-up study, especially since the diffusion is calculated within the performant, low-cost dynamical core (e.g. Becker and Burkhardt, 2007).

Thus, the aforementioned two-parameter approach is better suited to model the horizontal propagation of MWs. Eichinger et al. (2023) show promising investigations on the effects of the updated MW parametrization using this redistribution on model projections in EMAC. In their first look, the gap of GW drag at around 60°S is closed by the implemented redistribution of GWMF according to a general propagation pattern. The warm pole bias of EMAC is slightly alleviated, and the distribution of the final warming dates, i.e., the vortex breakdown, is altered by the updated MW parameterization. Further studies on the resulting model dynamics and nudging tendencies would, therefore, be of high interest.

In conclusion, the MWM developed as part of this thesis is a valuable tool for predicting MW activity, propagation, and induced quantities like residual temperatures and GWMF. The model application to specific case studies can benefit the understanding and interpretation of observations and high-resolution models. The propagation patterns estimated using the

MWM provide the basis for a simple, and in particular computation-cost efficient, improvement of MW parametrization schemes within climate models. The technical implementation of this two-parameter approach into the MESSy framework and a first study on the implications on the model dynamics is given by Eichinger et al. (2023). Such a straightforward yet effective approximation of the horizontal MW propagation is unprecedented in climate modeling.

Appendices

A.1 List of mathematical notation

This thesis follows standard conventions for mathematical symbols: scalars are given in lowercase italics, vector quantities in lowercase bold italics, and functions and atmospheric constants are given in uppercase italics. The subscripts q_x, q_y, and q_z refer to the respective directional component. The subscripts q_0 and q_1 refer to the background and perturbation part of the quantity in linear theory, respectively. Amplitudes are given by the subscript q_A.

Particular notation:

$\boldsymbol{x} = (x, y, z)$	position vector in Cartesian coordinates
ρ	density
p	pressure
H	atmospheric density height scale
N	Brunt–Väisälä frequency
g	gravity acceleration, $\approx 9.81 \, \mathrm{ms}^{-2}$
T	temperature
Θ	potential temperature
Γ	adiabatic lapse rate, $\approx -9.8 \, \mathrm{Kkm}^{-1}$
f	Coriolis parameter
Fr	Froude Number
Ri	Richardson Number
$\boldsymbol{U} = (U, V, W)$	wind velocity vector
$\boldsymbol{k} = (k, l, m)$	wave vector
λ_z	vertical wavelength
λ_{hor}	horizontal wavelength
ω	frequency
ζ	displacement
$_{gb}$	ground-based, i.e., with respect to the ground
$\boldsymbol{c_g} = (c_{gx}, c_{gy}, c_{gz})$	group velocity vector
c_{ph}	phase velocity
F, F_x, F_y	gravity wave momentum flux, zonal and meridional gravity wave momentum flux

D_x, D_y	zonal and meridional gravity wave drag
E	energy
A	wave action density
$_0$	background component
$_1$	wave perturbation
$_A$	(wave) amplitude
μ	orography standard deviation
σ	orography slope
γ	orographic anisotropy
τ_1, τ_2	GW drag components in MW parameterizations
$H(x, y)$	terrain elevation
l_{min}	minimal line length for the Hough transformation
l_{gap}	maximum line gap for the Hough transformation
ϕ	longitude
θ	latitude
α	ridge orientation
h	ridge height
a	ridge width
l	ridge length

A.2   List of abbreviations

ALIMA	Airborne Lidar for the Middle Atmosphere
DLR	Deutches Zentrum für Luft und Raumfahrt, engl. German Aerospace Center
ECMWF	European Centre for Medium-Range Weather Forecasts
EMAC	ECHAM MESSy Atmospheric Chemistry
ERA5	ECMWF Reanalysis 5th Generation
GCM	general circulation model
GROGRAT	Gravity-wave Regional Or Global Ray Tracer
GW	gravity wave
GWMF	gravity wave momentum flux
HIRDLS	High Resolution Dynamics Limb Sounder
IFS	Integrated Forecast System
MEM/HA	maximum entropy method & harmonic analysis
MW	mountain wave
MWM	mountain wave model
UTLS	Upper Troposphere/Lower Stratosphere
WKB	Wentzel-Kramers-Brillouin

A.3 Amplitude correction terms in GROGRAT

The amplitude correction by approximating $\nabla \cdot \boldsymbol{j}$ locally is derived in Eq. 3.5. The individual contributions of the gradients of the group velocity components are given in full length in this appendix. The representation is shortened by limiting the breakdown of individual terms to the ones that GROGRAT already calculates, i.e., the gradients in the background parameters N and $\alpha = \frac{1}{2H}$ and the intrinsic frequency $\hat{\omega}$, which correspond to the refraction terms ($\frac{dk_i}{dt} = -\frac{\partial \hat{\omega}}{\partial x_i}$).

The partial derivatives of the horizontal components of the group velocity therefore read:

$$\partial_x c_{g,x} = U_x + \frac{k}{\hat{\omega}\Delta}\left(N_x^2 - 2\hat{\omega}\hat{\omega}_x\right) - \frac{k(N^2 - \hat{\omega}^2)}{\hat{\omega}^2\Delta^2}\left(\hat{\omega}\alpha_x^2 + \Delta\hat{\omega}_x\right), \tag{A.3.1}$$

$$\partial_y c_{g,y} = V_y + \frac{k}{\hat{\omega}\Delta}\left(N_y^2 - 2\hat{\omega}\hat{\omega}_y\right) - \frac{k(N^2 - \hat{\omega}^2)}{\hat{\omega}^2\Delta^2}\left(\hat{\omega}\alpha_y^2 + \Delta\hat{\omega}_y\right), \tag{A.3.2}$$

$$\partial_x c_{g,z} = -\frac{2m\hat{\omega}\hat{\omega}_x}{\hat{\omega}\Delta} + \frac{m(\hat{\omega}^2 - f^2)}{\hat{\omega}^2\Delta^2}\left(\Delta\hat{\omega}_x + \hat{\omega}\alpha_x^2\right), \tag{A.3.3}$$

$$\partial_y c_{g,z} = -\frac{m}{\hat{\omega}\Delta}\left(2\hat{\omega}\hat{\omega}_y - f_y^2\right) + \frac{m(\hat{\omega}^2 - f^2)}{\hat{\omega}^2\Delta^2}\left(\Delta\hat{\omega}_y + \hat{\omega}\alpha_y^2\right). \tag{A.3.4}$$

These terms have been implemented in the differential equation calculating the vertical flux of wave action in GROGRAT. An option allows choosing between the standard amplitude estimation and the one corrected for horizontal wave packet deformations along the path.

A.4 Mountain Wave blocking diagrams

Since the blocking diagrams described in Taylor et al. (1993) are not directly applicable to orographic GWs close to their source where $\omega_{\mathrm{gb}} \approx 0$, we show a different type of blocking diagram in this section. The considerations are based on the relation of wave vector to intrinsic frequency and the lower limit for the frequency of GWs:

$$\omega_{\text{intr}} = -kU - lV, \tag{A.4.1}$$

$$\omega_{\text{intr}} \overset{!}{\geq} |f|. \tag{A.4.2}$$

Here f is the Coriolis parameter, k and l are the zonal and meridional wavenumbers, and U and V are the zonal and meridional background wind speeds. Combining both equations allows an estimation where the intrinsic frequency drops below the Coriolis frequency for a given wind speed and direction, which directly corresponds to a critical level for MWs and therefore restricts vertical propagation.

Figure 7.1 shows the restricted (horizontal) phase space for the same regions and wind profiles as Fig. 4.9a – d. Panels a and c show the Himalaya and Mongolian Plateau region, respectively, where basically the opposite of the more general blocking diagrams can be seen. While Fig. 4.9 shows that the Himalaya region has the more restricted phase speed space for non-orographic GWs, for GWs of orographic origin, the Himalaya region shows a more favorable phase space. Only half the phase space is strongly restricted here, while about two-thirds are restricted above the Mongolian Plateau. This strengthens our finding that the northward shift seen in the HIRDLS observations is due to stronger non-orographic GWs in the northern region and MWs refracting to large vertical wavelengths in the southern region.

The Rocky Mountain region in Fig. 7.1b is highly restricted for mountain waves, as is expected due to the wind reversal, and therefore almost no MWs will reach up to $25\,\text{km}$ altitude. Although there is a hint at a wind reversal in the vertical wind profile of the southern Africa region, this is not confirmed by Fig. 7.1d, where a large part of the GW spectrum is blocked, but by far not the full phase space as in Fig. 7.1b. The weak surface level winds (c.f Fig. 4.9f) are, however, very unfavorable conditions to launch and propagate MWs to the stratosphere in the first place.
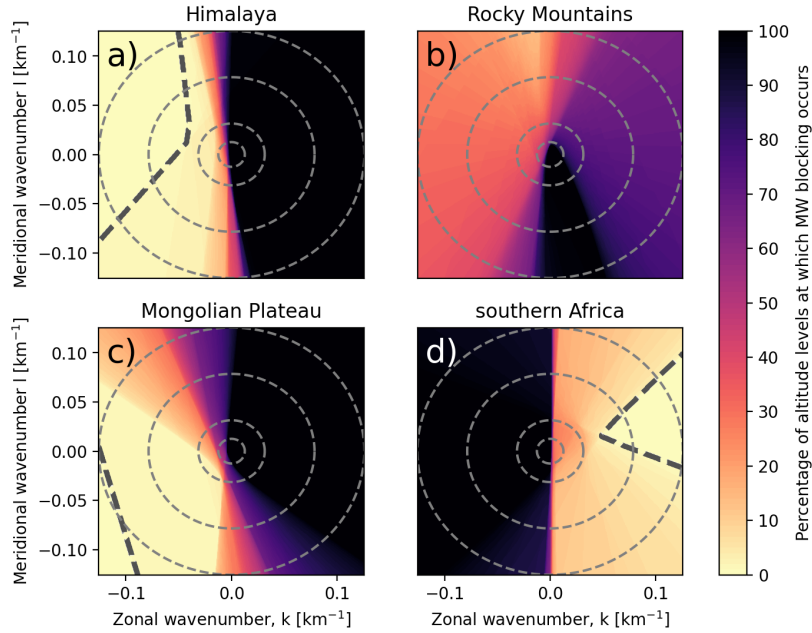
Figure 7.1: Mountain wave blocking diagrams similar to the ones given in Fig. 4.9 but more applicable for MWs with $\omega_{\text{gb}} \approx 0$. In this case, the critical level filtering is based on the wind profile and Eq. A.4.2. The percentage of altitudes from the surface to 25 km at which an MW of given horizontal wavenumbers is blocked is given in color shading. The dashed line separates the region of (horizontal) phase space that does encounter no critical level at any level (radially outwards w.r.t. the dashed line). Circular gird lines show horizontal wavelengths of 500 km, 200 km, 80 km, and 50 km (from the center outwards). Note that this diagram does not consider refraction, which could lead to MWs maneuvering around critical levels in phase space on their propagation path.

A.5 GWMF contribution of small-scale islands

For an estimation of the contribution of small-scale islands to the total GWMF, an MWM simulation without these islands as MW sources is performed. For this, the corresponding mountain ridges are simply removed from the underlying ridge database. The resulting global GWMF distribution throughout the year, analogously to Fig. 5.1, is shown in Fig. 7.2. The general distribution is the same, as expected. During the southern hemispheric winter, however, larger parts of the GWMF distributions are missing, especially the one above the Kerguelen Islands. Although the effect of the small-scale islands is very variable, the reduction in total GWMF due to the removal of these islands adds up to about 20% of the total zonal mean GWMF at around 60°S in the winter months.
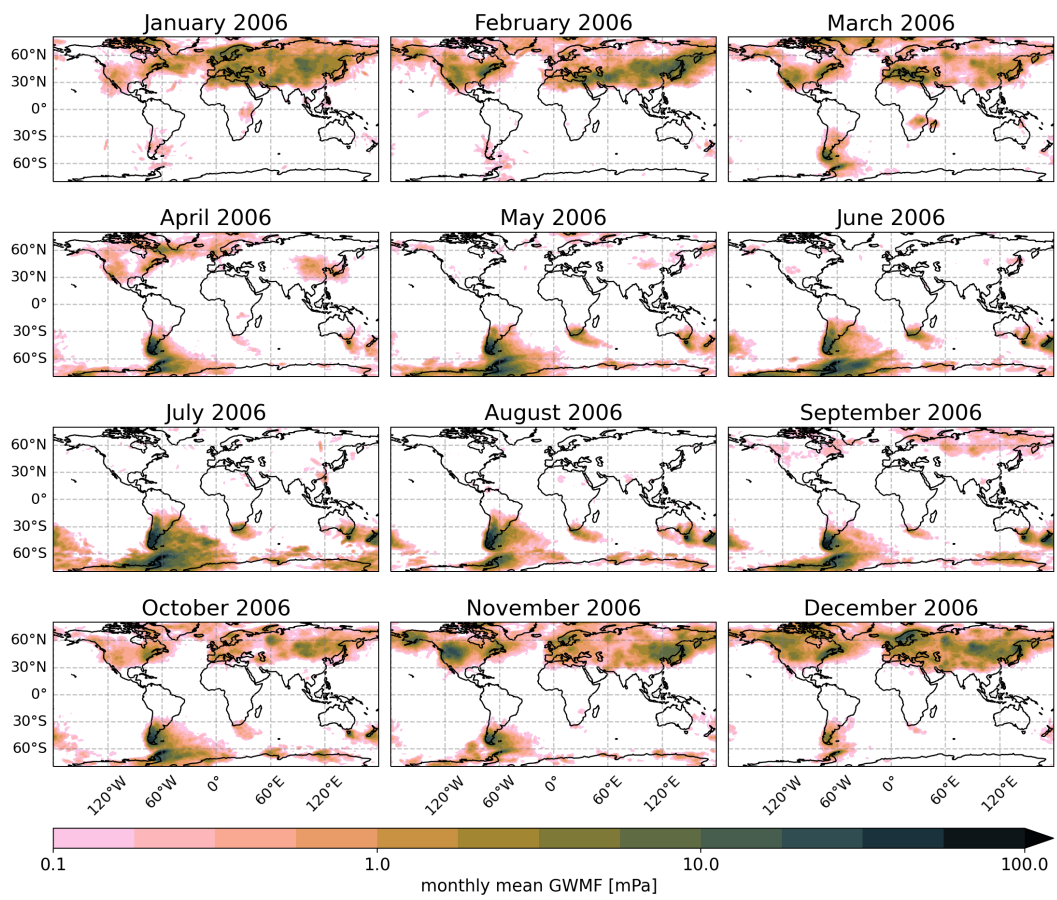
Figure 7.2: Horizontal distributions of GWMF throughout the year similar to Fig. 5.1 but without small-scale islands as MW sources.

Danksagung

Zuallererst möchte ich mich bei meinem Doktorvater Prof. Dr. Martin Riese für die Chance bedanken an diesem Projekt arbeiten zu können und ein kleines Puzzleteil zur Verbesserung von Klimamodellen beitragen zu können. Besonderer Dank geht auch an meinen Betreuer Dr. Peter Preusse, der mir zu jeder Zeit für Diskussionen und konstruktiver Kritik zur Verfügung stand. Weiterhin bedanke ich mich herzlich bei Dr. Manfred Ern für die viele Zeit und Expertise, die du meinen Artikeln gewidmet und hinzugefügt hast. Ebenso bedanke ich mich bei Dr. Jörn Ungermann für viele (teils sehr technische) Diskussionen und Anregungen zu meinen Ansätzen. Ohne jeden Einzelnen von euch wäre die Arbeit in dieser Form nicht zustande gekommen.

Desweiteren bedanke ich mich bei dem HITEC Graduiertenprogramm, das mich durch eine Vielzahl von Veranstaltungen zu einem besseren Doktoranden machteund motivierte und mich mit anderen Doktoranden vernetzt hat. Zudem ermöglichte mir HITEC einen Besuch bei meinen externen Mentor Dr. Julio Bacmeister Boulder. Many thanks for the opportunity to visit you, Julio, and all the input and optimism you provided!

Danke auch an alle meine Kollegen im IEK-7, insbesondere meine Mit-Doktoranden Markus Geldenhuys, Lukas Krasauskas und Konstantin Ntokas, für den mal-mehr-mal-weniger wissenschaftlichen Austausch und die angenehme Arbeitsatmosphäre im Institut.

Und zu guter letzt bedanke ich mich bei meiner Familie und im besonderen bei Eva dafür, dass ihr immer für mich da seid und mich jederzeit mit unterstützt!

Bibliography

J. R. Albers and T. Birner. Vortex preconditioning due to planetary and gravity waves prior to sudden stratospheric warmings. *J. Atmos. Sci.*, 71(11):4028–4054, 2014. doi: 10.1175/JAS-D-14-0026.1.

M. J. Alexander and T. J. Dunkerton. A spectral parameterization of mean-flow forcing due to breaking gravity waves. *J. Atmos. Sci.*, 56:4167–4182, 1999.

M. J. Alexander and K. H. Rosenlof. Gravity-wave forcing in the stratosphere: Observational constraints from the upper atmosphere research satellite and implications for parameterization in global models. *J. Geophys. Res.*, 108(D19):4597, 2003. doi: 10.1029/2003JD003373.

M. J. Alexander, M. Geller, C. McLandress, S. Polavarapu, P. Preusse, F. Sassi, K. Sato, S. Eckermann, M. Ern, A. Hertzog, Y. Kawatani, M. Pulido, T. A. Shaw, M. Sigmond, R. Vincent, and S. Watanabe. Recent developments in gravity-wave effects in climate models and the global distribution of gravity-wave momentum flux from observations and models. *Quart. J. Roy. Meteorol. Soc.*, 136:1103–1124, 2010. ISSN 0035-9009. doi: 10. 1002/qj.637.

C. Amante and B. Eakins. ETOPO1 1 arc-minute global relief model: Procedures, data sources and analysis, 2009. last access: 20 February 2020.

D. G. Andrews, J. R. Holton, and C. B. Leovy. *Middle Atmosphere Dynamics*, volume 40 of *International Geophysics Series*. Academic Press, 1987. ISBN 0-12-058576-6.

J. A. Anstey and T. G. Shepherd. High-latitude influence of the quasi-biennial oscillation. *Quarterly Journal of the Royal Meteorological Society*, 140(678):1–21, 2014. doi: https://

doi.org/10.1002/qj.2132. URL `https://rmets.onlinelibrary.wiley.com/doi/abs/10.1002/qj.2132`.

J. Bacmeister, P. Newman, B. Gary, and K. Chan. An algorithm for forecasting mountain wave-related turbulence in the stratosphere. *Wea. Forecast.*, 9(2):241–253, JUN 1994. ISSN 0882-8156. doi: 10.1175/1520-0434(1994)009⟨0241:AAFFMW⟩2.0.CO;2.

J. T. Bacmeister. Mountain-wave drag in the stratosphere and mesosphere inferred from observed winds and a simple mountain-wave parameterization scheme. *J. Atmos. Sci.*, 50: 377–399, 1993.

P. Baines and T. Palmer. Rationale for a new physically-based parametrization of subgrid-scale orographic effects. *ECMWF Technical Memoranda*, (169):11, 07 1990. doi: 10.21957/h4h36b3u. URL `https://www.ecmwf.int/node/7875`.

M. P. Baldwin, B. Ayarzagüena, T. Birner, N. Butchart, A. H. Butler, A. J. Charlton-Perez, D. I. V. Domeisen, C. I. Garfinkel, H. Garny, E. P. Gerber, M. I. Hegglin, U. Langematz, and N. M. Pedatella. Sudden stratospheric warmings. *Reviews of Geophysics*, 59 (1):e2020RG000708, 2021. doi: https://doi.org/10.1029/2020RG000708. URL `https://agupubs.onlinelibrary.wiley.com/doi/abs/10.1029/2020RG000708`. e2020RG000708 10.1029/2020RG000708.

R. G. Barry. *Mountain Weather and Climate*. Cambridge University Press, Cambridge, UK, third edition, 2008. ISBN 978-0511754753. doi: 10.1017/CBO9780511754753.

G. Baumgarten and D. C. Fritts. Quantifying kelvin-helmholtz instability dynamics observed in noctilucent clouds: 1. methods and observations. *Journal of Geophysical Research: Atmospheres*, 119(15):9324–9337, 2014. doi: https://doi.org/10.1002/2014JD021832. URL `https://agupubs.onlinelibrary.wiley.com/doi/abs/10.1002/2014JD021832`.

E. Becker and U. Burkhardt. Nonlinear horizontal diffusion for gcms. *Monthly Weather Review*, 135(4):1439 – 1454, 2007. doi: https://doi.org/10.1175/MWR3348.1. URL `https://journals.ametsoc.org/view/journals/mwre/135/4/mwr3348.1.xml`.

F. P. Bretherton. The propagation of groups of internal gravity waves in a shear flow. *Quarterly Journal of the Royal Meteorological Society*, 92(394):466–480, 1966. doi: https://doi.org/10.1002/qj.49709239403. URL `https://rmets.onlinelibrary.wiley.com/doi/abs/10.1002/qj.49709239403`.

F. P. Bretherton. On the mean motion induced by internal gravity waves. *J. Fluid Mech.*, 36 (4):785–803, 1969. doi: 10.1017/S0022112069001984.

N. Butchart. The brewer-dobson circulation. *Rev. Geophys.*, 52(2):157–184, 2014. ISSN 1944-9208. doi: 10.1002/2013RG000448. URL `http://dx.doi.org/10.1002/2013RG000448`.

G. Bölöni, Y.-H. Kim, S. Borchert, and U. Achatz. Toward transient subgrid-scale gravity wave representation in atmospheric models. part i: Propagation model including nondissipative wave–mean-flow interactions. *Journal of the Atmospheric Sciences*, 78 (4):1317 – 1338, 2021. doi: https://doi.org/10.1175/JAS-D-20-0065.1. URL `https://journals.ametsoc.org/view/journals/atsc/78/4/JAS-D-20-0065.1.xml`.

C. C. C. S. (C3S). ERA5: Fifth generation of ECMWF atmospheric reanalyses of the global climate., 2017. URL `https://cds.climate.copernicus.eu/cdsapp#!/home`.

F. Chane-Ming, F. Molinaro, J. Leveau, P. Keckhut, A. Hauchecorne, and S. Godin. Vertical short-scale structures in the upper tropospheric and lower stratospheric temperature and ozone at la réunion island (20.8°s 55.3°e). *Journal of Geophysical Research: Atmospheres*, 105(D22):26857–26870, 2000. doi: https://doi.org/10.1029/2000JD900199. URL `https://agupubs.onlinelibrary.wiley.com/doi/abs/10.1029/2000JD900199`.

H.-J. Choi and H.-Y. Chun. Momentum flux spectrum of convective gravity waves. Part I: An update of a parameterization using mesoscale simulations. *J. Atmos. Sci.*, 68(4):739–759, APR 2011. ISSN 0022-4928. doi: 10.1175/2010JAS3552.1.

M. Corcos, A. Hertzog, R. Plougonven, and A. Podglajen. Observation of gravity waves at the tropical tropopause using superpressure balloons. *Journal of Geophysical Research: Atmospheres*, 126(15):e2021JD035165, 2021. doi: https://doi.org/10.1029/

2021JD035165. URL `https://agupubs.onlinelibrary.wiley.com/doi/abs/10.1029/2021JD035165`. e2021JD035165 2021JD035165.

C. Y. Cullens and B. Thurairajah. Gravity wave variations and contributions to stratospheric sudden warming using long-term ERA5 model output. *J. Atm. Sol.-Terr. Phys.*, 219, AUG 2021. ISSN 1364-6826. doi: 10.1016/j.jastp.2021.105632.

C. Y. Cullens, S. L. England, and T. J. Immel. Global responses of gravity waves to planetary waves during stratospheric sudden warming observed by saber. *Journal of Geophysical Research: Atmospheres*, 120(23):12,018–12,026, 2015. doi: https://doi.org/10.1002/2015JD023966. URL `https://agupubs.onlinelibrary.wiley.com/doi/abs/10.1002/2015JD023966`.

R. O. Duda and P. E. Hart. Use of the hough transformation to detect lines and curves in pictures. *Communications of the ACM*, 15(1):11–15, 1972.

S. D. Eckermann and C. J. Marks. GROGRAT: a new model of the global propagation and dissipation of atmospheric gravity waves. *Adv. Space Res.*, 20:1253–1256, 1997.

S. D. Eckermann and P. Preusse. Global measurements of stratospheric mountain waves from space. *Science*, 286(5444):1534–1537, 1999. doi: 10.1126/science.286.5444.1534.

S. D. Eckermann and D. L. Wu. Satellite detection of orographic gravity-wave activity in the winter subtropical stratosphere over Australia and Africa. *Geophys. Res. Lett.*, 39(21), 2012. doi: https://doi.org/10.1029/2012GL053791. URL `https://agupubs.onlinelibrary.wiley.com/doi/abs/10.1029/2012GL053791`.

B. Ehard, B. Kaifler, N. Kaifler, and M. Rapp. Evaluation of methods for gravity wave extraction from middle-atmospheric lidar temperature measurements. *Atmos. Meas. Tech.*, 8(11):4645–4655, 2015. doi: 10.5194/amt-8-4645-2015.

R. Eichinger, S. Rhode, H. Garny, P. Preusse, P. Pisoft, A. Kuchař, P. Jöckel, A. Kerkweg, and B. Kern. Emulating lateral gravity wave propagation in a global chemistry–climate model (EMAC v2.55.2) through horizontal flux redistribution. *Geosci. Model Dev.*, 16(19):

5561–5583, 2023. doi: 10.5194/gmd-16-5561-2023. URL `https://gmd.copernicus.org/articles/16/5561/2023/`.

M. Ern, P. Preusse, M. J. Alexander, and C. D. Warner. Absolute values of gravity wave momentum flux derived from satellite data. *J. Geophys. Res. Atmos.*, 109(D20), 2004. ISSN 2156-2202. doi: 10.1029/2004JD004752.

M. Ern, F. Ploeger, P. Preusse, J. C. Gille, L. J. Gray, S. Kalisch, M. G. Mlynczak, J. M. Russell III, and M. Riese. Interaction of gravity waves with the QBO: A satellite perspective. *J. Geophys. Res. Atmos.*, 119:2329–2355, 2014. doi: 10.1002/2013JD020731.

M. Ern, Q. T. Trinh, P. Preusse, J. C. Gille, M. G. Mlynczak, J. M. Russell III, and M. Riese. GRACILE: A comprehensive climatology of atmospheric gravity wave parameters based on satellite limb soundings. *Earth Syst. Sci. Dat.*, 10:857–892, 2018. doi: 10.5194/essd-10-857-2018. URL `https://www.earth-syst-sci-data.net/10/857/2018/`.

M. Ern, Q. T. Trinh, M. Kaufmann, I. Krisch, P. Preusse, J. Ungermann, Y. Zhu, J. C. Gille, M. G. Mlynczak, J. M. Russell, III, M. J. Schwartz, and M. Riese. Satellite observations of middle atmosphere gravity wave absolute momentum flux and of its vertical gradient during recent stratospheric warmings. *Atmos. Chem. Phys.*, 16(15):9983–10019, AUG 9 2016. ISSN 1680-7316. doi: 10.5194/acp-16-9983-2016.

D. Fritts and M. Alexander. Gravity wave dynamics and effects in the middle atmosphere. *Rev. Geophys.*, 41(1), APR 16 2003. ISSN 8755-1209. doi: 10.1029/2001RG000106.

D. C. Fritts and P. K. Rastogi. Convective and dynamical instabilities due to gravity wave motions in the lower and middle atmosphere: theory and observations. *Radio Sci.*, 20: 1247–1277, 1985.

D. C. Fritts, G. Baumgarten, K. Wan, J. Werne, and T. Lund. Quantifying kelvin-helmholtz instability dynamics observed in noctilucent clouds: 2. modeling and interpretation of observations. *Journal of Geophysical Research: Atmospheres*, 119(15):9359–9375, 2014. doi: https://doi.org/10.1002/2014JD021833. URL `https://agupubs.onlinelibrary.wiley.com/doi/abs/10.1002/2014JD021833`.

W. A. Gallus and J. B. Klemp. Behavior of flow over step orography. *Monthly Weather Review*, 128(4):1153 – 1164, 2000. doi: https://doi.org/10.1175/1520-0493(2000)128⟨1153: BOFOSO⟩2.0.CO;2. URL `https://journals.ametsoc.org/view/journals/mwre/128/4/1520-0493_2000_128_1153_bofoso_2.0.co_2.xml`.

R. R. Garcia, A. K. Smith, D. E. Kinnison, A. de la Camara, and D. J. Murphy. Modification of the gravity wave parameterization in the whole atmosphere community climate model: Motivation and results. *J. Atmos. Sci.*, 74(1):275–291, 2017. doi: 10.1175/JAS-D-16-0104.1.

C. I. Garfinkel, E. P. Gerber, O. Shamir, J. Rao, M. Jucker, I. White, and N. Paldor. A qbo cookbook: Sensitivity of the quasi-biennial oscillation to resolution, resolved waves, and parameterized gravity waves. *Journal of Advances in Modeling Earth Systems*, 14 (3):e2021MS002568, 2022. doi: https://doi.org/10.1029/2021MS002568. URL `https://agupubs.onlinelibrary.wiley.com/doi/abs/10.1029/2021MS002568`. e2021MS002568 2021MS002568.

M. Geldenhuys, P. Preusse, I. Krisch, C. Zülicke, J. Ungermann, M. Ern, F. Friedl-Vallon, and M. Riese. Orographically induced spontaneous imbalance within the jet causing a large-scale gravity wave event. *Atmos. Chem. Phys.*, 2021. doi: 10.5194/acp-21-10393-2021.

M. Geldenhuys, B. Kaifler, P. Preusse, J. Ungermann, P. Alexander, L. Krasauskas, S. Rhode, W. Woiwode, M. Ern, M. Rapp, and M. Riese. Observations of gravity wave refraction and its causes and consequences. *J. Geophys. Res. Atmos.*, 128(3):e2022JD036830, FEB 16 2023. ISSN 2169-897X. doi: 10.1029/2022JD036830.

M. A. Geller, M. J. Alexander, P. T. Love, J. Bacmeister, M. Ern, A. Hertzog, E. Manzini, P. Preusse, K. Sato, A. A. Scaife, and T. Zhou. A comparison between gravity wave momentum fluxes in observations and climate models. *J. Clim.*, 26(17):6383–6405, SEP 2013. ISSN 0894-8755. doi: 10.1175/JCLI-D-12-00545.1.

A. E. Gill. *Atmosphere-ocean dynamics*, volume 30 of *International Geophysics Series*. Academic Press, 1982.

J. C. Gille, J. J. Barnett, J. G. Whitney, M. A. Dials, D. Woodard, W. P. Rudolf, A. Lambert, and W. Mankin. The High-Resolution Dynamics Limb Sounder (HIRDLS) experiment on AURA. *Proc. SPIE*, 5152:161–171, 2003. doi: 10.1117/12.507657.

S. Gisinger, I. Polichtchouk, A. Dörnbrack, R. Reichert, B. Kaifler, N. Kaifler, M. Rapp, and I. Sandu. Gravity-wave-driven seasonal variability of temperature differences between ECMWF IFS and Rayleigh lidar measurements in the lee of the Southern Andes. *J. Geophys. Res. Atmos.*, 127(13):e2021JD036270, 2022. doi: https://doi.org/10.1029/2021JD036270. e2021JD036270 2021JD036270.

GLOBE Task Team. The global land one-kilometer base elevation (globe) digital elevation model, version 1.0. 1999. URL `http://www.ngdc.noaa.gov/mgg/topo/globe.html`. Accessed 20.07.2023.

C. González, M. Bachmann, J.-L. Bueso-Bello, P. Rizzoli, and M. Zink. A fully automatic algorithm for editing the tandem-x global dem. *Remote Sensing*, 12(23), 2020. ISSN 2072-4292. doi: 10.3390/rs12233961. URL `https://www.mdpi.com/2072-4292/12/23/3961`.

E. E. Gossard and W. H. Hooke. Waves in the atmosphere, atmospheric infrasound and gravity waves - their generation and propagation. *Elsevier Scientific Publishing Company*, 1975.

M.-V. Guarino, M. A. C. Teixeira, T. L. Keller, and R. D. Sharman. Mountain-wave turbulence in the presence of directional wind shear over the rocky mountains. *Journal of the Atmospheric Sciences*, 75(4):1285–1305, 2018. doi: 10.1175/JAS-D-17-0128.1. URL `https://journals.ametsoc.org/view/journals/atsc/75/4/jas-d-17-0128.1.xml`.

A. Gupta, T. Birner, A. Dörnbrack, and I. Polichtchouk. Importance of gravity wave forcing for springtime southern polar vortex breakdown as revealed by era5. *Geophysical Research Letters*, 48(10):e2021GL092762, 2021. doi: https://doi.org/10.1029/2021GL092762. URL `https://agupubs.onlinelibrary.wiley.com/doi/abs/10.1029/2021GL092762`. e2021GL092762 2021GL092762.

I. Hajnsek, A. Moreira, M. Zink, S. Buckreuss, T. Kraus, M. Bachmann, and T. Busche. Tandem-x: 10 years of operation. In *IGARSS 2020 - 2020 IEEE International Geoscience and Remote Sensing Symposium*, pages 3403–3405, 2020. doi: 10.1109/IGARSS39084.2020. 9323263.

D. A. Hastings and P. K. Dunbar. Global land one-kilometer base elevation (globe). *NOAH National Geophysical Data Center*, Publication KGRD-34:138pp, 1999. URL `https://www.ngdc.noaa.gov/mgg/topo/report/globedocumentationmanual.pdf`.

C. J. Heale and J. B. Snively. Gravity wave propagation through a vertically and horizontally inhomogeneous background wind. *Journal of Geophysical Research: Atmospheres*, 120(12): 5931–5950, 2015. doi: https://doi.org/10.1002/2015JD023505. URL `https://agupubs.onlinelibrary.wiley.com/doi/abs/10.1002/2015JD023505`.

H. Hersbach, B. Bell, P. Berrisford, G. Biavati, A. Horányi, J. Muñoz Sabater, J. Nicolas, C. Peubey, R. Radu, I. Rozum, D. Schepers, A. Simmons, C. Soci, D. Dee, and J.-N. Thépaut. ERA5 hourly data on pressure levels from 1979 to present. copernicus climate change service (C3S) climate data store (CDS), 2018. accessed February 17, 2022.

H. Hersbach, B. Bell, P. Berrisford, S. Hirahara, A. Horanyi, J. Munoz-Sabater, J. Nicolas, C. Peubey, R. Radu, D. Schepers, A. Simmons, C. Soci, S. Abdalla, X. Abellan, G. Balsamo, P. Bechtold, G. Biavati, J. Bidlot, M. Bonavita, G. De Chiara, P. Dahlgren, D. Dee, M. Diamantakis, R. Dragani, J. Flemming, R. Forbes, M. Fuentes, A. Geer, L. Haimberger, S. Healy, R. J. Hogan, E. Holm, M. Janiskova, S. Keeley, P. Laloyaux, P. Lopez, C. Lupu, G. Radnoti, P. de Rosnay, I. Rozum, F. Vamborg, S. Villaume, and J.-N. Thepaut. The ERA5 global reanalysis. *Quart. J. Roy. Meteorol. Soc.*, 146(730):1999–2049, JUL 2020. ISSN 0035-9009. doi: {10.1002/qj.3803}.

N. P. Hindley, C. J. Wright, L. Hoffmann, T. Moffat-Griffin, and N. J. Mitchell. An 18-year climatology of directional stratospheric gravity wave momentum flux from 3-D satellite observations. *Geophys. Res. Lett.*, 47(22):e2020GL089557, NOV 28 2020. ISSN 0094-8276. doi: 10.1029/2020GL089557.

J. Holton and H. Tan. The influence of the eqautorial quasi-biennial oscillation on the global circulation at 50 mb. *J. Atmos. Sci.*, 37(10):2200–2208, 1980. ISSN 0022-4928. doi: {10.1175/1520-0469(1980)037⟨2200:TIOTEQ⟩2.0.CO;2}.

J. Y. Jia, P. Preusse, M. Ern, H. Y. Chun, J. C. Gille, S. D. Eckermann, and M. Riese. Sea surface temperature as a proxy for convective gravity wave excitation: a study based on global gravity wave observations in the middle atmosphere. *Ann. Geophys.*, 32(11): 1373–1394, 2014. ISSN 0992-7689. doi: 10.5194/angeo-32-1373-2014.

J. Jiang, S. Eckermann, D. Wu, and J. Ma. A search for mountain waves in MLS stratospheric limb radiances from the winter Northern Hemisphere: Data analysis and global mountain wave modeling. *J. Geophys. Res. Atmos.*, 109(D3), FEB 11 2004. ISSN 2169-897X. doi: 10.1029/2003JD003974.

J. H. Jiang and D. L. Wu. UARS MLS observations of gravity waves associated with the Arctic winter stratospheric vortex. *Geophys. Res. Lett.*, 28(3):527–530, 2001.

J. H. Jiang, S. D. Eckermann, D. L. Wu, and D. Y. Wang. Inter-annual variation of gravity waves in the Arctic and Antarctic winter middle atmosphere. *Adv. Space Res.*, 38(11): 2418–2423, 2006. ISSN 0273-1177. doi: 10.1016/j.asr.2005.09.036.

Q. Jiang and R. B. Smith. Gravity wave breaking in two-layer hydrostatic flow. *Journal of the Atmospheric Sciences*, 60(9):1159 – 1172, 2003. doi: https://doi.org/10. 1175/1520-0469(2003)060⟨1159:GWBITH⟩2.0.CO;2. URL `https://journals.ametsoc. org/view/journals/atsc/60/9/1520-0469_2003_060_1159_gwbith_2.0.co_2.xml`.

B. Kaifler, N. Kaifler, B. Ehard, A. Doernbrack, M. Rapp, and D. C. Fritts. Influences of source conditions on mountain wave penetration into the stratosphere and mesosphere. *Geophys. Res. Lett.*, 42(21):9488–9494, NOV 16 2015. ISSN 0094-8276. doi: 10.1002/ 2015GL066465.

N. Kaifler, B. Kaifler, B. Ehard, S. Gisinger, A. Dornbrack, M. Rapp, R. Kivi, A. Kozlovsky, M. Lester, and B. Liley. Observational indications of downward-propagating gravity waves

in middle atmosphere lidar data. *J. Atm. Sol.-Terr. Phys.*, 162(SI):16–27, SEP 2017. ISSN 1364-6826. doi: 10.1016/j.jastp.2017.03.003.

S. Kalisch, P. Preusse, M. Ern, S. D. Eckermann, and M. Riese. Differences in gravity wave drag between realistic oblique and assumed vertical propagation. *J. Geophys. Res. Atmos.*, 119:10,081–10,099, 2014. ISSN 2169-8996. doi: 10.1002/2014JD021779.

C.-W. Kang, R.-H. Park, and K.-H. Lee. Extraction of straight line segments using rotation transformation: generalized hough transformation. *Pattern Recognition*, 24(7):633–641, 1991. ISSN 0031-3203. doi: https://doi.org/10.1016/0031-3203(91)90030-9. URL `https://www.sciencedirect.com/science/article/pii/0031320391900309`.

M.-J. Kang, H.-Y. Chun, and B.-G. Song. Contributions of convective and orographic gravity waves to the brewer–dobson circulation estimated from ncep cfsr. *Journal of the Atmospheric Sciences*, 77(3):981–1000, 2020. doi: https://doi.org/10.1175/JAS-D-19-0177.1. URL `https://journals.ametsoc.org/view/journals/atsc/77/3/jas-d-19-0177.1.xml`.

M.-J. Kang, S.-W. Son, and H.-Y. Chun. Distinct upward propagation of the westerly qbo in winter 2015/16 and its relationship with brewer-dobson circulation. *Geophysical Research Letters*, 49(16):e2022GL100101, 2022. doi: https://doi.org/10.1029/2022GL100101. URL `https://agupubs.onlinelibrary.wiley.com/doi/abs/10.1029/2022GL100101`. e2022GL100101 2022GL100101.

J. Kidston, A. A. Scaife, S. C. Hardiman, D. M. Mitchell, N. Butchart, M. P. Baldwin, and L. J. Gray. Stratospheric influence on tropospheric jet streams, storm tracks and surface weather. *Nature Geosci.*, 8:433–440, 2015. doi: 10.1038/ngeo2424.

Y.-H. Kim and H.-Y. Chun. Contributions of equatorial wave modes and parameterized gravity waves to the tropical qbo in hadgem2. *Journal of Geophysical Research: Atmospheres*, 120(3):1065–1090, 2015. doi: https://doi.org/10.1002/2014JD022174. URL `https://agupubs.onlinelibrary.wiley.com/doi/abs/10.1002/2014JD022174`.

128

Y.-J. Kim. Representation of subgrid-scale orographic effects in a general circulation model. part i: Impact on the dynamics of simulated january climate. *Journal of Climate*, 9(11):2698–2717, 1996. doi: 10.1175/1520-0442(1996)009⟨2698:ROSSOE⟩2.0.CO; 2. URL `https://journals.ametsoc.org/view/journals/clim/9/11/1520-0442_1996_ 009_2698_rossoe_2_0_co_2.xml`.

Y.-J. Kim and A. Arakawa. Improvement of orographic gravity wave parameterization using a mesoscale gravity wave model. *J. Atmos. Sci.*, 52:11875–1902, 1995. doi: 10.1175/ 1520-0469(1995)052⟨1875:IOOGWP⟩2.0.CO;2.

Y.-j. Kim and J. D. Doyle. Extension of an orographic-drag parametrization scheme to incorporate orographic anisotropy and flow blocking. *Quarterly Journal of the Royal Meteorological Society*, 131(609):1893–1921, 2005. doi: https://doi.org/10.1256/qj.04.160. URL `https://rmets.onlinelibrary.wiley.com/doi/abs/10.1256/qj.04.160`.

M. Kogure, J. Yue, and H. Liu. Gravity wave weakening during the 2019 antarctic stratospheric sudden warming. *Geophysical Research Letters*, 48(8):e2021GL092537, 2021. doi: https://doi.org/10.1029/2021GL092537. URL `https://agupubs.onlinelibrary.wiley. com/doi/abs/10.1029/2021GL092537`.

L. Krasauskas, B. Kaifler, S. Rhode, J. Ungermann, W. Woiwode, and P. Preusse. Oblique propagation and refraction of gravity waves over the Andes observed by GLORIA and ALIMA during the SouthTRAC campaign. *J. Geophys. Res. Atmos.*, page e2022JD037798, 2023. doi: 10.1029/2022JD037798.

C. G. Kruse, M. J. Alexander, L. Hoffmann, A. van Niekerk, I. Polichtchouk, J. Bacmeister, L. Holt, R. Plougonven, P. Sacha, C. Wright, K. Sato, R. Shibuya, S. Gisinger, M. Ern, C. Meyer, , and O. Stein. Observed and modeled mountain waves from the surface to the mesosphere near the Drake Passage. *J. Atmos. Sci.*, pages 909–932, 2022. doi: 10.1175/ JAS-D-21-0252.1.

H. Li, J. Zhang, B. Sheng, Y. Fan, X. Ji, and Q. Li. The gravity wave activity during two recent qbo disruptions revealed by u.s. high-resolution radiosonde data. *Remote Sensing*,

15(2), 2023. ISSN 2072-4292. doi: 10.3390/rs15020472. URL `https://www.mdpi.com/2072-4292/15/2/472`.

M. J. Lighthill. Waves in fluids. *Communications on Pure and Applied Mathematics*, 20(2):267–293, 1967. doi: https://doi.org/10.1002/cpa.3160200204. URL `https://onlinelibrary.wiley.com/doi/abs/10.1002/cpa.3160200204`.

M. J. Lighthill. Waves in fluids. *Cambridge University Press*, page 504pp, 1978.

E.-P. Lim, H. H. Hendon, G. Boschat, D. Hudson, D. W. J. Thompson, A. J. Dowdy, and J. M. Arblaster. Australian hot and dry extremes induced by weakenings of the stratospheric polar vortex. *Nature Geoscience*, 12(11):896–901, 2019. doi: 10.1038/s41561-019-0456-x. URL `https://doi.org/10.1038/s41561-019-0456-x`.

E.-P. Lim, H. H. Hendon, A. H. Butler, D. W. J. Thompson, Z. D. Lawrence, A. A. Scaife, T. G. Shepherd, I. Polichtchouk, H. Nakamura, C. Kobayashi, R. Comer, L. Coy, A. Dowdy, R. D. Garreaud, P. A. Newman, and G. Wang. The 2019 southern hemisphere stratospheric polar vortex weakening and its impacts. *Bulletin of the American Meteorological Society*, 102(6):E1150 – E1171, 2021. doi: https://doi.org/10.1175/BAMS-D-20-0112.1. URL `https://journals.ametsoc.org/view/journals/bams/102/6/BAMS-D-20-0112.1.xml`.

R. S. Lindzen. Turbulence and stress due to gravity wave and tidal breakdown. *J. Geophys. Res.*, 86:9707–9714, 1981.

R. S. Lindzen. Supersaturation of vertically propagating internal gravity waves. *Journal of Atmospheric Sciences*, 45(4):705 – 711, 1988. doi: https://doi.org/10.1175/1520-0469(1988)045⟨0705:SOVPIG⟩2.0.CO;2. URL `https://journals.ametsoc.org/view/journals/atsc/45/4/1520-0469_1988_045_0705_sovpig_2_0_co_2.xml`.

R. S. Lindzen and J. R. Holton. A theory of the quasi-biennial oscillation. *J. Atmos. Sci.*, 25(6):1095–1107, 1968. doi: 10.1175/1520-0469(1968)025⟨1095:ATOTQB⟩2.0.CO;2.

F. Lott and M. J. Miller. A new subgrid scale orographic drag parameterization: Its formulation and testing. *Quart. J. Roy. Meteorol. Soc.*, 123:101–127, 1997.

F. Lott, B. Deremble, and C. Soufflet. Mountain waves produced by a stratified boundary layer flow. part i: Hydrostatic case. *Journal of the Atmospheric Sciences*, 77(5):1683 – 1697, 2020. doi: https://doi.org/10.1175/JAS-D-19-0257.1. URL `https://journals.ametsoc.org/view/journals/atsc/77/5/jas-d-19-0257.1.xml`.

F. Lott, B. Deremble, and C. Soufflet. Mountain waves produced by a stratified shear flow with a boundary layer. part ii: Form drag, wave drag, and transition from downstream sheltering to upstream blocking. *Journal of the Atmospheric Sciences*, 78(4):1101 – 1112, 2021. doi: https://doi.org/10.1175/JAS-D-20-0144.1. URL `https://journals.ametsoc.org/view/journals/atsc/78/4/JAS-D-20-0144.1.xml`.

C. J. Marks and S. D. Eckermann. A three-dimensional nonhydrostatic ray-tracing model for gravity waves: Formulation and preliminary results for the middle atmosphere. *J. Atmos. Sci.*, 52(11):1959–1984, 1995. doi: 10.1175/1520-0469(1995)052⟨1959:ATDNRT⟩2.0.CO;2.

T. Matsuno. A quasi one-dimensional model of the middle atmosphere circulation interacting with internal gravity waves. *Journal of the Meteorological Society of Japan. Ser. II*, 60(1): 215–226, 1982. doi: 10.2151/jmsj1965.60.1_215.

M. E. McIntyre. Breaking waves and global scale chemical transport in the Earth's atmosphere, with spinoffs for the sun's interior. *Prog. of Theor. Phys. / Suppl.*, 130:137–166, 1998.

M. J. Miller, T. N. Palmer, and R. Swinbank. Parametrization and influence of subgridscale orography in general circulation and numerical weather prediction models. *Meteorology and Atmospheric Physics*, (40):84–109, 03 1989. doi: 10.1007/BF01027469. URL `https://doi.org/10.1007/BF01027469`.

J. Muraschko, M. D. Fruman, U. Achatz, S. Hickel, and Y. Toledo. On the application of Wentzel-Kramer-Brillouin theory for the simulation of the weakly nonlinear dynamics of gravity waves (vol 141, pg 3446, 2015). *Quart. J. Roy. Meteorol. Soc.*, 141(693, B):3446, OCT 2015. ISSN 0035-9009. doi: 10.1002/qj.2719.

C. J. Nappo. *An Introduction to Atmospheric Gravity Waves*. Academic Press, second edition, 2012. ISBN 978-0-12-385223-6.

NASA Goddard Earth Sciences Data and Information Services Center. NASA GES DISC: The HIRDLS Level 2 product [data set]. URL `https://acdisc.gesdisc.eosdis.nasa.gov/data/Aura_HIRDLS_Level2/`. last accessed on 19 October 2022.

NOAA National Centers for Environmental Information. Etopo 2022 15 arc-second global relief model. 2022. doi: https://doi.org/10.25921/fd45-gt74. URL `https://www.ncei.noaa.gov/products/etopo-global-relief-model`. Accessed 20.07.2023.

J. A. Perrett, C. J. Wright, N. P. Hindley, L. Hoffmann, N. J. Mitchell, P. Preusse, C. Strube, and S. D. Eckermann. Determining gravity wave sources and propagation in the southern hemisphere by ray-tracing AIRS measurements. *Geophys. Res. Lett.*, 48(2):e2020GL088621, JAN 28 2021. ISSN 0094-8276. doi: 10.1029/2020GL088621.

D. S. Phillips. Analytical surface pressure and drag for linear hydrostatic flow over three-dimensional elliptical mountains. *Journal of Atmospheric Sciences*, 41(6):1073–1084, 1984. doi: 10.1175/1520-0469(1984)041⟨1073:ASPADF⟩2.0.CO;2. URL `https://journals.ametsoc.org/view/journals/atsc/41/6/1520-0469_1984_041_1073_aspadf_2_0_co_2.xml`.

R. Pierrehumbert. *An essay on the parameterization of orographic gravity wave drag*. PhD thesis, 1986 1986.

M. Placke, P. Hoffmann, R. Latteck, and M. Rapp. Gravity wave momentum fluxes from mf and meteor radar measurements in the polar MLT region. *J. Geophys. Res. Space*, 120(1): 736–750, JAN 2015. ISSN 2169-9380. doi: 10.1002/2014JA020460.

P. Preusse, S. D. Eckermann, and D. Offermann. Comparison of global distributions of zonal-mean gravity wave variance inferred from different satellite instruments. *Geophys. Res. Lett.*, 27(23):3877–3880, 2000. doi: 10.1029/2000GL011916.

P. Preusse, G. Eidmann, S. D. Eckermann, B. Schaeler, R. Spang, and D. Offermann. Indications of convectively generated gravity waves in CRISTA temperatures. *Adv. Space Res.*, 27(10):1653–1658, 2001.

P. Preusse, A. Dörnbrack, S. D. Eckermann, M. Riese, B. Schaeler, J. T. Bacmeister, D. Broutman, and K. U. Grossmann. Space-based measurements of stratospheric mountain waves by CRISTA, 1. sensitivity, analysis method, and a case study. *J. Geophys. Res.*, 107(D23) (8178), 2002. doi: 10.1029/2001JD000699.

P. Preusse, S. D. Eckermann, M. Ern, J. Oberheide, R. H. Picard, R. G. Roble, M. Riese, J. M. Russell III, and M. G. Mlynczak. Global ray tracing simulations of the SABER gravity wave climatology. *J. Geophys. Res. Atmos.*, 114, 2009. doi: 10.1029/2008JD011214.

P. Preusse, M. Ern, P. Bechtold, S. D. Eckermann, S. Kalisch, Q. T. Trinh, and M. Riese. Characteristics of gravity waves resolved by ECMWF. *Atmos. Chem. Phys.*, 14(19):10483–10508, 2014. doi: 10.5194/acp-14-10483-2014.

M. Rapp, B. Kaifler, A. Dörnbrack, S. Gisinger, T. Mixa, R. Reichert, N. Kaifler, S. Knobloch, R. Eckert, N. Wildmann, A. Giez, L. Krasauskas, P. Preusse, M. Geldenhuys, M. Riese, W. Woiwode, F. Friedl-Vallon, B.-M. Sinnhuber, A. de la Torre, P. Alexander, J. L. Hormaechea, D. Janches, M. Garhammer, J. L. Chau, J. F. Conte, P. Hoor, and A. Engel. SOUTHTRAC-GW: An airborne field campaign to explore gravity wave dynamics at the world's strongest hotspot. *Bull. Amer. Meteor. Soc.*, 102(4):E871 – E893, 2021. doi: 10.1175/BAMS-D-20-0034.1.

R. Reichert, B. Kaifler, N. Kaifler, A. Dörnbrack, M. Rapp, and J. L. Hormaechea. High-cadence lidar observations of middle atmospheric temperature and gravity waves at the southern Andes hot spot. *J. Geophys. Res. Atmos.*, 126(22):e2021JD034683, 2021. doi: https://doi.org/10.1029/2021JD034683. e2021JD034683 2021JD034683.

S. Rhode, P. Preusse, M. Ern, J. Ungermann, L. Krasauskas, J. Bacmeister, and M. Riese. A mountain ridge model for quantifying oblique mountain wave propagation and distribution.

Atmos. Chem. Phys., 23(14):7901–7934, 2023. doi: 10.5194/acp-23-7901-2023. URL `https://acp.copernicus.org/articles/23/7901/2023/`.

M. L. Salby and P. Callaghan. Sampling error in climate properties derived from satellite measurements: Consequences of undersampled diurnal variability. *Journal of Climate*, 10(1):18–36, 1997. doi: 10.1175/1520-0442(1997)010⟨0018:SEICPD⟩2.0.CO; 2. URL `https://journals.ametsoc.org/view/journals/clim/10/1/1520-0442_1997_010_0018_seicpd_2.0.co_2.xml`.

M. L. Salby and R. R. Garcia. Transient response to localized episodic heating in the tropics. Part I: Excitation and short-time near-field behavior. *J. Atmos. Sci.*, 44(2):458–498, 1987.

I. Sandu, P. Bechtold, A. Beljaars, A. Bozzo, F. Pithan, T. G. Shepherd, and A. Zadra. Impacts of parameterized orographic drag on the northern hemisphere winter circulation. *J. Adv. Model. Earth Syst.*, 8(1):196–211, MAR 2016. ISSN 1942-2466. doi: 10.1002/2015MS000564.

I. Sandu, A. van Niekerk, T. Shepherd, S. Vosper, A. Zadra, J. Bacmeister, A. Beljaars, A. Brown, A. Dörnbrack, N. McFarlane, F. Pithan, and G. Svensson. Impacts of orography on large-scale atmospheric circulation. *npj Climate and Atmospheric Science*, 2:10, 05 2019. doi: 10.1038/s41612-019-0065-9. URL `https://doi.org/10.1038/s41612-019-0065-9`.

K. Sato and S. Hirano. The climatology of the brewer–dobson circulation and the contribution of gravity waves. *Atmospheric Chemistry and Physics*, 19(7):4517–4539, 2019. doi: 10.5194/acp-19-4517-2019. URL `https://acp.copernicus.org/articles/19/4517/2019/`.

K. Sato, S. Tateno, S. Watanabe, and Kawatani. Gravity wave characteristics in the Southern Hemisphere revealed by a high-resolution middle-atmosphere general circulation model. *J. Atmos. Sci.*, 69:1378–1396, 2012. doi: 10.1175/JAS-D-11-0101.1.

M. Sigmond and J. F. Scinocca. The influence of the basic state on the northern hemisphere circulation response to climate change. *J. Clim.*, 23(6):1434–1446, 2010. doi: 10.1175/2009JCLI3167.1.

W. C. Skamarock. Evaluating mesoscale NWP models using kinetic energy spectra. *Mon. Weath. Rev.*, 132:3019–3032, 2004.

I.-S. Song, C. Lee, H.-Y. Chun, J.-H. Kim, G. Jee, B.-G. Song, and J. T. Bacmeister. Propagation of gravity waves and its effects on pseudomomentum flux in a sudden stratospheric warming event. *Atmos. Chem. Phys.*, 20(12):7617–7644, JUL 1 2020. ISSN 1680-7316. doi: 10.5194/acp-20-7617-2020.

C. C. Stephan, T. P. Lane, and C. Jakob. Gravity wave influences on mesoscale divergence: An observational case study. *Geophys. Res. Lett.*, 47(1), JAN 16 2020. ISSN 0094-8276. doi: 10.1029/2019GL086539.

G. Stober, S. Sommer, M. Rapp, and R. Latteck. Investigation of gravity waves using horizontally resolved radial velocity measurements. *Atmos. Meas. Tech.*, 6(10):2893–2905, 2013. doi: 10.5194/amt-6-2893-2013. URL `http://www.atmos-meas-tech.net/6/2893/2013/`.

C. Strube, M. Ern, P. Preusse, and M. Riese. Removing spurious inertial instability signals from gravity wave temperature perturbations using spectral filtering methods. *Atmos. Meas. Tech.*, 13(9):4927–4945, 2020. doi: 10.5194/amt-13-4927-2020. URL `https://amt.copernicus.org/articles/13/4927/2020/`.

C. Strube, P. Preusse, M. Ern, and M. Riese. Propagation paths and source distributions of resolved gravity waves in ECMWF-IFS analysis fields around the southern polar night jet. *Atmos. Chem. Phys.*, 21(24):18641–18668, 2021. doi: 10.5194/acp-21-18641-2021. URL `https://acp.copernicus.org/articles/21/18641/2021/`.

S. Suzuki, K. Shiokawa, Y. Otsuka, T. Ogawa, M. Kubota, M. Tsutsumi, T. Nakamura, and D. C. Fritts. Gravity wave momentum flux in the upper mesosphere derived from oh airglow imaging measurements. *Earth Planets Space*, 59:421–428, 2007.

M. J. Taylor, E. H. Ryan, T. F. Tuan, and R. Edwards. Evidence of preferential directions for gravity wave propagation due to wind filtering in the middle atmosphere. *J. Geophys. Res.*, 98:6047–6057, 1993. doi: 10.1029/92JA02604.

Q. T. Trinh, S. Kalisch, P. Preusse, H.-Y. Chun, S. D. Eckermann, M. Ern, and M. Riese. A comprehensive observational filter for satellite infrared limb sounding of gravity waves. *Atmos. Meas. Tech.*, 8:1491–1517, 2015. doi: 10.5194/amt-8-1491-2015.

Q. T. Trinh, S. Kalisch, P. Preusse, M. Ern, H.-Y. Chun, S. D. Eckermann, M.-J Kang, and M. Riese. Tuning of a convective gravity wave source scheme based on hirdls observations. *Atmos. Chem. Phys.*, 16:7335–7356, 2016. doi: 10.5194/acp-16-7335-2016.

S. L. Vadas and E. Becker. Numerical modeling of the excitation, propagation, and dissipation of primary and secondary gravity waves during wintertime at McMurdo Station in the Antarctic. *J. Geophys. Res. Atmos.*, 123(17):9326–9369, SEP 16 2018. ISSN 2169-897X. doi: 10.1029/2017JD027974.

S. L. Vadas and E. Becker. Numerical modeling of the generation of tertiary gravity waves in the mesosphere and thermosphere during strong mountain wave events over the Southern Andes. *J. Geophys. Res. Space*, 124(9):7687–7718, SEP 2019. ISSN 2169-9380. doi: {10.1029/2019JA026694}.

S. L. Vadas, D. C. Fritts, and M. J. Alexander. Mechanism for the generation of secondary waves in wave breaking regions. *J. Atmos. Sci.*, 60(1):194–214, 2003. doi: 10.1175/1520-0469(2003)060⟨0194:MFTGOS⟩2.0.CO;2. URL `https://doi.org/10.1175/1520-0469(2003)060<0194:MFTGOS>2.0.CO;2`.

S. L. Vadas, J. Zhao, X. Chu, and E. Becker. The excitation of secondary gravity waves from body forces: Theory and observation. *J. Geophys. Res. Atmos.*, 0(ja), 2018. doi: 10.1029/2017JD027970. URL `https://agupubs.onlinelibrary.wiley.com/doi/abs/10.1029/2017JD027970`.

A. van Niekerk and S. Vosper. Towards a more "scale-aware" orographic gravity wave drag parametrization: Description and initial testing. *Quarterly Journal of the Royal Meteorological Society*, 147(739):3243–3262, 2021. doi: https://doi.org/10.1002/qj.4126. URL `https://rmets.onlinelibrary.wiley.com/doi/abs/10.1002/qj.4126`.

F. Vargas, G. Yang, P. Batista, and D. Gobbi. Growth rate of gravity wave amplitudes observed in sodium lidar density profiles and nightglow image data. *Atmosphere*, 10(12), 2019. ISSN 2073-4433. doi: 10.3390/atmos10120750. URL `https://www.mdpi.com/2073-4433/10/12/750`.

P. N. Vargin and B. M. Kiryushov. Major sudden stratospheric warming in the arctic in february 2018 and its impacts on the troposphere, mesosphere, and ozone layer. *Russian Meteorology and Hydrology*, 44(2):112–123, 2019. doi: 10.3103/S1068373919020043. URL `https://doi.org/10.3103/S1068373919020043`.

R. A. Vincent, A. hertzog hertzog hertzog hertzog, G. Boccara, and F. Vail. Quasi-Lagrangian superpressure balloon mesurements of gravity-wave momentum fluxes in the polar stratosphere of both hemispheres. *Geophys. Res. Lett.*, 34, 2007. doi: 10.1029/2007GL031072.

G. S. Voelker, T. R. Akylas, and U. Achatz. An application of wkbj theory for triad interactions of internal gravity waves in varying background flows. *Quarterly Journal of the Royal Meteorological Society*, 147(735):1112–1134, 2021. doi: https://doi.org/10.1002/qj.3962. URL `https://rmets.onlinelibrary.wiley.com/doi/abs/10.1002/qj.3962`.

S. Watanabe, K. Sato, and M. Takahashi. A general circulation model study of the orographic gravity waves over antarctica excited by katabatic winds. *J. Geophys. Res.*, 111, 2006. doi: 10.1029/2005JD006851.

A. Wegener. Studien über luftwogen. *Beitr. Physik Freien Atmos.*, 4:23–25, 1906.

J. Wei, F. Zhang, J. H. Richter, M. J. Alexander, and Y. Q. Sun. Global distributions of tropospheric and stratospheric gravity wave momentum fluxes resolved by the 9-km ecmwf experiments. *Journal of the Atmospheric Sciences*, 79(10):2621 – 2644, 2022. doi: https://doi.org/10.1175/JAS-D-21-0173.1. URL `https://journals.ametsoc.org/view/journals/atsc/79/10/JAS-D-21-0173.1.xml`.

L. J. Wilcox and A. J. Charlton-Perez. Final warming of the southern hemisphere polar vortex in high- and low-top cmip5 models. *Journal of Geophysical Research: Atmospheres*,

118(6):2535–2546, 2013. doi: https://doi.org/10.1002/jgrd.50254. URL `https://agupubs.onlinelibrary.wiley.com/doi/abs/10.1002/jgrd.50254`.

C. J. Wright, S. M. Osprey, J. J. Barnett, L. J. Gray, and J. C. Gille. High Resolution Dynamics Limb Sounder measurements of gravity wave activity in the 2006 Arctic stratosphere. *J. Geophys. Res.*, 2009. doi: 10.1029/2009JD011858.

J. Xie, M. Zhang, Z. Xie, H. Liu, Z. Chai, J. He, and H. Zhang. An orographic-drag parametrization scheme including orographic anisotropy for all flow directions. *J. Adv. Model. Earth Syst.*, 12, 2020. doi: 10.1029/2019MS001921.

J. Xie, M. Zhang, Q. Zeng, Z. Xie, H. Liu, Z. Chai, J. He, and H. Zhang. Implementation of an orographic drag scheme considering orographic anisotropy in all flow directions in the earth system model cas-esm 2.0. *Journal of Advances in Modeling Earth Systems*, 13 (12):e2021MS002585, 2021. doi: https://doi.org/10.1029/2021MS002585. URL `https://agupubs.onlinelibrary.wiley.com/doi/abs/10.1029/2021MS002585`. e2021MS002585 2021MS002585.

X. Xu, D. Yu, and J. Luo. The spatial and temporal variability of global stratospheric gravity waves and their activity during sudden stratospheric warming revealed by cosmic measurements. *ADVANCES IN ATMOSPHERIC SCIENCES*, 35(12):1533–1546, DEC 2018. ISSN 0256-1530. doi: 10.1007/s00376-018-5053-1.

H. Xue, X. Zhou, Y. Luo, and J. Yin. Impact of parameterizing the turbulent orographic form drag on convection-permitting simulations of winds and precipitation over south china during the 2019 pre-summer rainy season. *Atmospheric Research*, 263: 105814, 2021. ISSN 0169-8095. doi: https://doi.org/10.1016/j.atmosres.2021.105814. URL `https://www.sciencedirect.com/science/article/pii/S0169809521003707`.

X. Yan, N. Arnold, and J. Remedios. Global observations of gravity waves from High Resolution Dynamics Limb Sounder temperature measurements: A yearlong record of temperature amplitude and vertical wavelength. *J. Geophys. Res. Atmos.*, 115:D10113, MAY 29 2010. ISSN 2169-897X. doi: 10.1029/2008JD011511.